Development of Joule Heating Coating Layers for Membrane Distillation Process

by

Arian Enayat

A thesis submitted in partial fulfillment of the requirements for the degree of

Master of Science

Department of Mechanical Engineering

University of Alberta

© Arian Enayat, 2020

Abstract

Membrane desalination processes have attracted much attention in the last few decades with regards to water purification. While some methods such as reverse osmosis (RO) are demonstrated at the commercial scale, some such as membrane distillation (MD) have not been deployed, mainly due to issues associated with energy efficiency requirements. Some attempts have been recently made to improve energy consumption of the MD setup by developing heat-generating membranes. Although the methods explored in the literature have yielded promising results, the materials and techniques incorporated in those studies were not financially viable.

In this M.Sc. study, the application of Joule heating coating layers deposited via flame spraying to develop heat-generating MD membranes was investigated. In the first stage of this work, stainless steel meshes were chosen to serve as the base material. Prior to nichrome deposition, alumina was coated on the steel substrate to function as a dielectric intermediary medium. To fabricate hydrophobic MD membranes, polyvinylidene fluoride (PVDF) was cast on the steel substrate's backside. Scanning electron microscopy (SEM) characterization was conducted to determine the deposited particles' morphology and the thickness of each layer.

Even though, at the best practice, the resistive heating tests showed a 16°C temperature difference across some samples, most could not generate the desired heat due to short-circuiting. To resolve this problem, the mesh substrates were replaced with carbon steel sheets, and instead of fabricating the polymeric layer, commercial hydrophobic polytetrafluoroethylene (PTFE) membranes were used. The Joule heating performance of

the developed samples was examined in air, deionized (DI) water, and saline water. For the experiments conducted in water, a commercial H-bridge was integrated into the electrical circuit to minimize electron leakage. It was shown that the higher H-bridge frequencies provided more efficient resistive heating performance. The Joule heating coating layers generated enough heat to increase the water temperature and provide the necessary driving force to distill water.

The MD experiments showed that 80 W of power increased the Joule heating sample's temperature and its surroundings to 80°C, resulting in water desalination at 2.24 kg/hr.m^2 rate. Although the recorded flux was lower than that of conventional MD tests, the amount of energy consumed in this novel method makes this new generation of MD membranes promising. Even after hours of operation, the samples' electrical conductivity did not deteriorate, suggesting that any oxides found in the system originated from the steel substrate rather than the nichrome/alumina layer. Also, the chemical composition analysis of the permeate water showed that its quality remained intact. These results indicate that Joule heating coating layers fabricated inexpensively by flame spraying can improve the MD process's energy consumption, making it a more viable option to be used commercially.

Lastly, a mathematical model was developed to predict and evaluate the performance of the Joule heating coating layers as part of the MD setup. Even though the developed model was quite simple, in most cases, the predicted values were in close agreement with the results obtained from the experimental study. The modeling results suggested that the temperature polarization was 2- to 3 times lower than which has been recorded by other investigators for conventional MD process. Reflection on both the experimental and

theoretical elements indicated that the Joule heating element could increase the temperature of its surroundings as desired. But the feed tank not being thermally insulated wasted most of the heat generated by the Joule heating element, resulting in its low efficiency. It could be said that with the right optimization made in the design of the MD setup and cell, the Joule heating element could become much more efficient.

Preface

Some of the sections included in this thesis will be published in peer-reviewed journals or conference papers as follows:

- Chapter 3 of this thesis has been prepared for submission to the *Journal of Thermal Spray Technology.,* Title: "**Development of Joule Heating Coating Layers for Membrane Distillation Process.**"
- Chapter 4 and parts of Chapter 3 of this thesis have been prepared for submission to *Desalination.,* Title: "**Mathematical Modeling of The Joule Heating Coating Layer Integration Into the MD process.**"

This research work was conducted under the supervision of Dr. Andre McDonald and Dr. Mohatada Sadrzadeh. The collaboration with Ms. Sadaf Noamani resulted in the development of Chapter 4 of this work. Parts of the mathematical model developed by Ms. Sadaf Noamani as part of her M.Sc. program were modified to produce the results presented in Chapter 4.

Acknowledgment

Firstly, I would like to express my gratitude to my supervisors Dr. André McDonald and Dr. Mohtada Sadrzadeh, for their trust, patience, and support. Their guidance helped me overcome the many challenges that this interdisciplinary project posed. It indeed was an honor to work with and learn from them.

Secondly, I am grateful to Dr. Hossein Rouhani and Dr. Peichun Tsai for agreeing to serve on the thesis defense exam committee.

Thirdly, I had the opportunity of working alongside many talented engineers as part of my research project. I learned many things from them on both professional and personal levels. Ms. Sadaf Noamani kindly trained me in the "advanced water research lab" (AWRL), and she also helped me develop the membrane distillation aspect of this project.

Also, I am grateful for having access to the services of very knowledgeable and dedicated technicians who worked at the mechanical engineering department. Mr. Les Dean developed the LabVIEW program, which helped us to control the frequency of the H-bridge. Also, he developed the electrical circuit, which was used in this project. Most importantly, he graciously let us use his data acquisition system for three months. The progress of this project in the defined time frame would not be possible without his kindness.

Last but not least, I would like to thank my parents, Masoud and Shahin, and brother, Shayan, for their never-ending love, morale, and financial support. I had the privilege of having them by my side while walking down my academic path.

Table of Contents

Contents

List of Tables

List of Figures

Nomenclature

A	Area	m^2
B_{M}	Membrane mass transfer coefficient	$\mathrm{kg}/(\mathrm{m}^2\mathrm{sPa})$
C	Conductivity	µS/cm
c	Concentration	Mole/Litre
$\mathrm{c_p}$	Specific heat capacity	J/(kgK)
CPC	Concentration polarization coefficient	-
D	Water diffusion coefficient	m^2/s
D_{h}	Hydraulic diameter of the flow channel	m
d_{pore}	Diameter of the membrane pores	µm
$\in -\mathrm{NTU}$	Effectiveness-Number of Transfer Units	-
h	Heat transfer coefficient	$\mathrm{W}/(\mathrm{m}^2\mathrm{K})$
ΔH	Enthalpy or Latent Heat of vaporization of water	kJ/kg
J_{w}	Mass flux	$\mathrm{kg}/(\mathrm{m}^2\mathrm{s})$
k	Thermal conductivities	W/mK
K	Overall mass transfer coefficient of salt ions	m/s
K_{B}	The Boltzmann constant	1.380649×10^{-23} J/K
K_{M}	Effective thermal conductivity of the membrane	W/mK
$\mathrm{K_n}$	Knudsen number	-
MW_{w}	Molecular weight of water	Kg/mol
$\dot{m}$	Flow rate	Kg/s
Δm	Mass	Kg
Nu	Nusselt number	-
P	Pressure	Pa
Pr	Prandtl number	-
Q	Heat transfer	W/m^2
Q_{H}	The energy that consumed for heating the feed solution	W
Q_{M}	Heat transfer through the membrane	W/m^2
Q_{cm}	Heat conduction through the membrane material	W/m^2
r	Radios of membrane pore size	µm
R	The universal gas constant	8.314 J/(molK)
Re	Reynolds	-
S	Salt concentration	gr/L
T	Temperature	K
t	time	hour
TPC	Temperature polarization coefficient	-
U	Overall heat transfer coefficient	$\mathrm{W}/(\mathrm{m}^2\mathrm{K})$
x	Mole fraction	-

Greek symbols

η	Thermal efficiency	%
γ	Activity coefficient	-
δ	Membrane thickness	µm
ε	Membrane porosity	%
λ	Mean free path of the transported molecules through membrane pores	m
ρ	Density	kg/m^3
σ	The collision diameter of water molecules	2.641×10^{-10} m
τ	Tortuosity	-

Subscripts

air, pore	Air inside pores
bf	Bulk feed
bp	Bulk Permeate
c	Cold
cm	Conduction in membrane
f	feed
gas	Air within the pores
h	Hot
in	inlet
m	membrane
mf	membrane surface on the feed side
mp	membrane surface on the permeate side
out	outlet
p	permeate
$pore$	pores
v	Vapors/Vaporization
w	Water
wf	Water in feed
wvf	Water vapor feed
wvp	Water vapor permeate

Chapter 1

1. Introduction

1.1 Membrane Distillation

Overuse of natural resources due to the expansion of human activities coupled with pollution and global warming has taken a toll on water reservoirs [1 – 6]. Water scarcity and difficulty in having access to uncontaminated sources of water have become two major issues challenging the future of communities [3, 4, 7]. The concern regarding these issues has motivated the development of more efficient ways of water treatment and water reuse [3–7].

Membrane-based processes have gained much popularity in the last few decades [6, 8]. In these systems, the membrane plays the role of a selective filter retaining some components of the solution or letting them pass through ergo a more desired composition is obtained, whether as the retentate or the permeate [9, 10]. Nowadays, some of these processes, such as reverse osmosis (RO), governed by pressure difference, have been used extensively in practice [6, 11 – 13]. Despite being a widely-used mechanism, RO lacks the ability to desalinate highly saline waters, which has created a drive to develop a method overcoming this shortcoming [11 – 14]. Membrane distillation (MD), a thermally driven process in which the membrane acts as a barrier keeping the saline and pure water separated from each other, has been promoted as a desalination method capable of perfect salt rejection in addition to having the potential to be more reasonable financially as the applied pressure is negligible [15, 16]. Furthermore, the MD membrane does not need to have pores as small as the RO membranes while being made of cheaper materials [15]. Another

important point is that the MD process's required energy could be supplied by clean energy sources and heat wastes [15, 17]. Finally, the absence of pressure during the MD process eliminates the need to implement "heavy gauge piping" and reduces the susceptibility of the membrane to fouling [18].

Unlike many membrane processes, MD is a thermally driven process in which the temperature difference across the membrane acts as a driving force [4, 5, 13, 18 – 24]. In this method, the temperature difference leads to a vapour pressure difference between the feed and permeate sides [4, 5, 20, 21, 23 – 27]. As a result, the hot water on the feed side evaporates when it is in contact with the membrane, and the vapours move to the other side of the membrane to condensate [4, 5, 13, 20, 21, 23, 25 – 27]. In order for this mechanism to work as expected, only water vapour should be allowed to move through the membrane, leaving the contaminants on the feed side [4, 5, 20 – 23, 25, 26, 28]. The membranes not getting wet imposes an extra mass transfer resistance induced by the air entrapped inside the pores [15]. The MD process can be performed in various configurations, with each having certain superiorities.

The MD process can be done in direct contact membrane distillation (DCMD), air gap membrane distillation (AGMD), vacuum membrane distillation (VMD), and sweeping gas membrane distillation (SGMD) forms [15, 29 – 31]. Starting with the simplest one, in the DMCD process, the membrane itself is the only physical barrier separating the feed and permeate waters [15 – 17, 32]. The main disadvantages of the DCMD setup are the high susceptibility of the membrane pores to being wet and the significant heat waste caused by the heat conduction through the membrane structure [15, 17]. However, these issues have not affected the broad implementation of this method owing to its simplicity while yielding

relatively high flux [17, 20, 32]. In the AGMD configuration, in addition to the membrane, a thin layer of stagnant air on the permeate side helps separate the contaminated and pure water from each other [15, 16, 31, 32]. Although the air layer acts as an insulating layer, lowering the heat loss through the membrane, it diminishes the mass transfer rate [15, 31, 32]. In the SGMD modules, the added air on the permeate side is dynamic, unlike AGMD, which carries the water vapours reaching the permeate side to a condenser placed outside of the cell for phase conversion [15, 31, 32]. Even though air movement facilitates mass transfer, incorporating a powerful condenser is a disadvantage [15, 32]. Finally, in VMD, similar to the SGMD, the water vapour is moved from inside of the MD cell to an external condenser to complete the distillation process [31]. Still, the only difference is that instead of air, the vacuum acts as the vapour carrier [15, 31, 32]. VMD has the highest water purification rate among all the MD modules while maintaining its heat loss at a low level [15, 32]. The requirement of incorporating a vacuum pump and membranes with smaller pores are among the downsides of this MD configuration [31, 32]. Moving on to the factors affecting the MD performance, the first one is the membrane thickness.

Although thick membranes provide higher energy efficiency owing to less heat conduction through the membrane, the higher thickness leads to a lower permeation through the membranes [19, 27, 32]. Such a trade-off relation suggests the need for optimizing the membrane thickness for MD application [19, 32]. It has been suggested that, as long as the thickness of the membrane lies between 10 to 60 μm, the membrane thickness would have an optimum behavior regarding the mass transfer rate and heat loss [32].

In addition to the thickness of the membrane, two natural phenomena called temperature and concentration polarization also have an adverse effect on the performance

of the MD process [6, 13, 19, 33 – 36]. The temperature polarization is induced by evaporation and condensation of water on the surface of the membrane itself, which reduces the temperature on the feed side and increases it on the permeate side [13, 37, 38]. The endothermic and exothermic physical reactions differ the temperature of the membrane surface from the bulk, which leads to a slight reduction in the temperature difference across the membrane [37, 38]. The concentration polarization occurs when the membrane prevents the contaminants from reaching the permeate side [6, 36]. The accumulation of the contaminants on the feed side of the membrane diminishes the vapour pressure of the feed side [35, 36]. Another adverse effect of this phenomenon is the accelerated scaling of the MD membrane by minerals such as divalent ions [6, 18, 39]. Membrane scaling decreases the flux significantly and reduces the lifetime of the membranes, which consequently increases the MD desalination process [18, 39, 40]. In addition to the "operational conditions," the membrane and feed water properties each play their respective roles regarding promoting or preventing the fouling/scaling phenomenon [40]. Fouling/scaling could be delayed by increasing the water flow in the channels and proper material selection for the membrane, making it less susceptible to fouling/scaling [6,18]. It must be noted that the high flow of water increases the chances of membrane pores flooding. Therefore, the safest approach is focusing on membrane characteristics.

To delay membrane wetting and fouling, researchers have suggested using hydrophobic materials for the MD process [8]. The required pressure for the feed water entering the membrane pores is known as "Liquid entry pressure" (LEP), which is defined Eq.(1.1) as [21, 41 – 43]

$$LEP = \frac{-2B\gamma_l \cos(\theta)}{r}. \quad (1.1)$$

In this equation, B, γ_l, θ, and r correspond to the geometric factor of the membrane, the liquid surface tension, the contact angle of the liquid, and the maximum pore size of the membrane, respectively [21, 41 – 43]. As it is evident from Equation 1.1, the smaller the membrane pores and the more hydrophobic the membrane surface, the more difficult the flooding of the membrane pores by the feed water [21, 41]. In common practice, the pore size should be less than 1 μm for the desired performance of the MD membranes [8, 44]. Although smaller pores yield higher resistance to wetting, they pose more mass transfer resistance reducing the water flux [42]. The pore size determines the water vapour's interaction mechanism with air and pore walls, which governs the mass transfer through the membrane [42].

Moving on to the last physical property of the membrane, the porosity of the membrane also plays an integral part regarding its mass transfer efficiency. Kang *et al.* [8] and Albrecht *et al.* [44] have suggested 50-80 % and 70-80% porosity as the appropriate range for MD membranes, respectively.

1.2 Heat-Generating Membranes

Conventionally, to operate the MD setup, the feed water tank is usually heated to reach the desired temperature. Then the water is fed into the MD cell while its temperature is maintained at the working temperature. Also, on the permeate side, a cooling device is connected to the permeate water tank to keep it cool enough to retain the temperature difference across the membrane as the intended one. These processes consume a substantial amount of energy, which lowers the energy efficiency of the MD mechanism. Therefore,

the development of heat-generating membranes would be a big step toward commercializing the MD process [13, 36, 38, 45 – 48]. The implementation of self-heating membranes was reported to improve the energy efficiency of the process when compared to the bulk heating method of the conventional MD assemblies [13, 36, 38]. In addition, self-heating membranes were found to diminish the negative impact of the temperature polarization phenomenon on water flux [13, 36, 38].

The idea of implementing photothermal materials as a part of the membrane structure to generate self-heating properties has been widely investigated in the literature. Some materials have relatively small bandgaps, making them prone to get electronically excited while being irradiated [46]. To name a few, semiconductors, polymers, carbon, gold, and silver could be mentioned as materials with this capability [13, 36, 38, 46, 47]. According to Politano *et al.* [13], ultraviolet (UV) irradiation of the polyvinylidene fluoride (PVDF) membrane consisted of 25% wt silver nanoparticles yielded a 23.3°C rise in the feed water temperature. Ye *et al.* [47] stated that one-minute UV light irradiation of their PVDF/Ag composite membrane raised the temperature of the feed solution to 93°C, followed by 2.5 kg/m^2hr flux coupled with 53 % energy efficiency. Although Tan *et al.* [48] have adopted PVDF/ titanium carbide ($Ti_3C_2T_x$) membranes for self-heating purposes, they have indicated lower flux of their composite membranes than the pristine PVDF membranes (10 % lower) due to the smaller pores of the coated membranes. Huang *et al.* [36] have designed a photothermal self-heating MD system that could use solar energy to overcome the process's energy demands. Their graphene/PTFE membrane yielded a 78 % improvement in mass flux when compared to the pristine commercial PTFE membrane due to the photothermal activity of the graphene-based component [36].

It is worth mentioning that financial obstacles raised by the materials and coating method costs have hindered the acceptance of the photothermal materials from being considered viable commercial options for the self-heating membranes [13, 46]. Also, the efficiency of the indirect use of electricity in the form of UV light could be questioned. Last but not least, for systems capable of working with solar energy, the cost of solar systems and the incapability of this design to work under universal conditions could keep this design far from reality. Therefore, an alternative approach to develop self-heating membranes that could use the electrical energy directly regardless of the season and time of the day could be the required leap for the MD process to become a more commercially accepted process.

Instead of photothermal materials, the incorporation of resistive heating materials could be the answer to this issue. In order to have the highest level of energy efficiency, there should be no intermediate layers between the Joule heating layer and the feed water [45]. Of course, when dealing with DI water, this direct contact might not be a big concern, but when it comes to waters containing impurities, electron leakage and electrochemical degradation of the materials would be among the concerns [45]. Dudchenko *et al.* [45] overcame these problems by coupling a direct current (DC) power supply with an in-house built H-bridge, enabling them to change the electrical current direction, which prevented any over-accumulation of electrons on the surface of the resistive heating layer. In 125 hours of consistent operation of their design with 20 V and 100 kHz, no issues were observed [45]. Still, the absence of an industrially cheap process to fabricate such a membrane seems to be a problem [45]. The successful examples of resistive heating

coating deposition via thermal spray coating methods widely implemented in the industry could be found in the literature and is presented in the following section.

1.3 Thermal Spray Coating Deposition

Thermal spray coating has been established as an economical way to fabricate protective and smart coatings for various applications [49]. This coating method has been used extensively because of its low cost and reliability [50]. In the thermal spray coating process, the feedstock, which is in the form of powder or wire, is heated by a heat source [51 – 56]. As a result, the feedstock is fully or partially melted; at this point, the particles are propelled toward the substrate for impact and penetration to form a coating [51 – 56]. Depending on the device's working temperature and the particles' velocity, the thermal spray coating is divided into many categories [54]. The deposition of the particles on the substrate's surface happens mostly due to mechanical interlocking [55].

The coating process, which was used in this work, was flame spraying. In the flame spray deposition process, the implemented heat source is the combustion of oxy-acetylene to provide up to 3000°C temperature to melt the feedstock [55, 57]. The particles' velocity in this method gets as high as 100 m/s, which is provided by the flow of an inert gas carrying the feedstock particles [55]. Figure 1.1 shows the thermal spray process schematically.

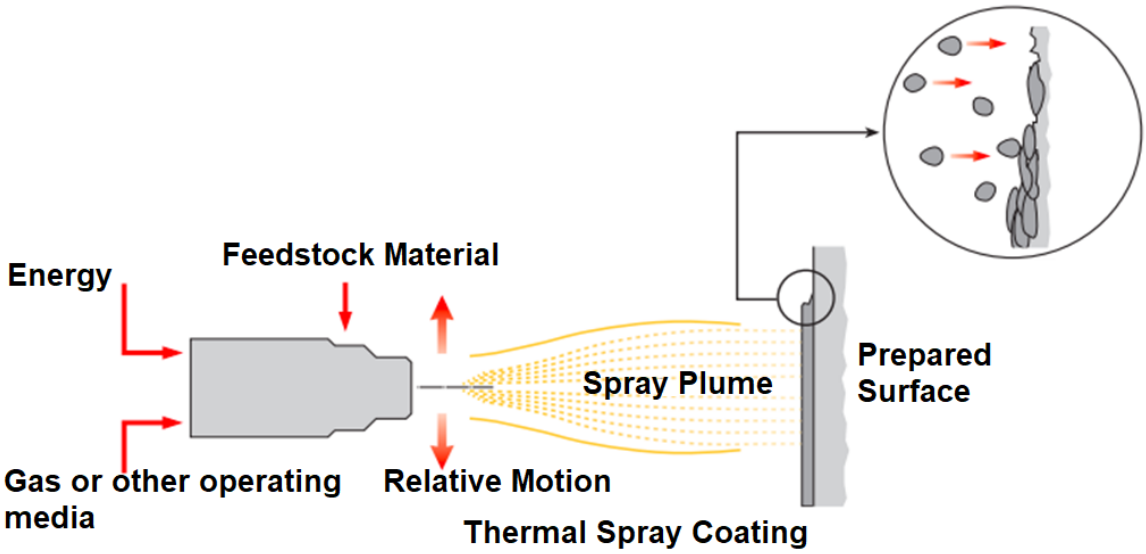

Figure 1.1 Schematic of the thermal spray process [58]

Since the coating deposition is done on the surface, the substrate surface properties and conditions are of great importance [51, 59]. It is recommended that the substrates get thoroughly clean prior to any other preparation steps [51, 59]. Thereafter, the substrates' surface should be grit blasted to enhance the surface roughness, which plays a pivotal role in the adhesion of the deposited coatings [54, 60]. Another pre-coating measure is preheating the substrate by letting the flame torch to go over the substrate for at least one pass [51, 61]. Not only the preheating eliminates moisture from the surface of the substrate, but also it anneals the substrate, allaying the residual stress [51, 61]. Also, the absence of preheating might lead to potential thermal shocks, which might come into existence due to a significant temperature difference between the coating particles and the substrate itself [62].

There are many parameters involved in the coating process, and each one plays its respective role in the final coating characteristics. For example, acetylene's ratio to oxygen,

the pressure of added air, standoff distance (SOD), torch velocity, number of passes, carrier gas (usually argon) pressure, and powder flow rate are influential parameters on the coating process. Adjusting all these parameters to an optimum degree could yield a high-quality coating with useful functionality.

During the high-temperature thermal spray coating methods, there is the chance of over-heating the substrate, leading to poor coating adhesion to the substrate due to excessive oxidation and substrate damage [52, 62]. To minimize the substrate oxidation, spray parameters such SOD and the cooling gas pressure can be modified, or a cooling system could be used [52, 63].

To fabricate a resistive heating coating on top of a conductive substrate without short-circuiting, there is a need to deposit an electrically insulating layer [49, 61, 63, 64]. The resistive heating coating should be deposited on top of that [49, 61, 63, 64].

1.3.1 Alumina Coating

To develop resistive heating layers on top of electrically conductive substrates, it is necessary to fabricate an electrically insulating material between the substrate and the Joule heating layer as an intermediary [57, 61, 63, 64]. Many ceramic materials have the insulating characteristic to be chosen for this role, but the thermal expansion coefficient mismatch of the substrate and this layer narrows down the range of possible options [61]. In the case of significant mismatch, the thermal expansion and shrinkage of both materials during and post coating process leads to coating delamination and damage [49, 61, 65]. Therefore, alumina has been promoted as a material meeting these requirements by many scholars [50].

It is worth mentioning that only the alpha phase of alumina yields highly stable electrical insulations, which is in contrast with other phases of this material [49, 50, 53, 64, 66, 67]. Thus, in addition to implementing alpha phase powders for the coating procedure, it is necessary to ensure that this material has not gone through any phase conversions while being deposited [53, 54, 64]. Rezvani Rad [50] has shown that close control of the spraying parameters could prevent the alumina particles from going through the unwanted phase change while being sprayed.

Some parameters such as thickness, humidity, porosity, mechanical stress can be detrimental to the electrical insulating properties of alumina [49, 50, 67, 68]. Toma *et al.* [66] tests have shown that as the alumina layer thickness increased, the dielectric breakdown voltage (DBV) followed. They have also demonstrated a resistance drop in DC electrical resistance of the alumina layers in order of 10^5 when the alumina coated samples were exposed to humid conditions [66].

It has been widely accepted that the porous structure has more vulnerability than the bulk ones to experience dielectric breakdown [66]. The pores provide an easy path for the electrons to leak through the structure and result in dielectric breakdown [69]. On the other hand, the structural defects pose resistance to the swift movement of electrons, which improves the electrical resistivity of the material [61, 65]

Most thermal sprayed alumina films have shown porous structure, reducing its thermal conductivity [54, 63]. This porosity is mostly a consequence of expeditious solidification of the coated particles [63]. Michels *et al.* [63] have implied that bulk alumina has ten times the electrical conductivity possessed by the ones deposited by plasma spray coating.

Niittymaki *et al.* [54] have shown the dependence of DC breakdown strength on both the coating method and environmental parameters. It is evident in their results that the alumina films fabricated by flame spray coating had much lower breakdown voltage when compared to APS and HVOF coatings [54]. Additionally, it has been indicated that the alumina layers are more susceptible to voltage breakdown when moisture is added to the working environment, but this vulnerability is allayed at low temperatures (20 to 120°C) [54]. The electrical resistivity of this material also dwindles when exposed to humidity [54]. In the alumina layers, which consisted of gamma-alumina, more dielectric sensitivity with the change in humidity was observed, which was linked to the alumina's hygroscopic structure [54].

Michels *et al.* [70] have reported that 100 μm thick alumina layers deposited by HVOF, APS, and VPS methods provided 50-250 kΩ electrical resistance. Rezvani Rad *et al.* [61] reported success in maintaining the alpha-alumina phase as the dominating phase in the alumina layers' chemical composition by modifying the spray parameters. They Also have suggested preheating the substrate prior to initiation of the alumina coating deposition to minimize the creation of thermally-induced stresses [61]. Although, it has been mentioned that rapid solidification and cooling of the alumina splats during the flame spray coating process is accompanied by crack formation, compromising the full potential of the dielectric characteristic [50].

1.3.2 Resistive Heating Coating Layer

Certain materials have the capability of generating a significant amount of heat when there is electron passage through their structure due to their high electrical resistance,

which are known as "Joule heating" or "resistive heating" materials [49, 71]. The development of heat-generating coatings has attracted much attention, especially for de-icing purposes [50, 61, 71, 72]. The superiority of Joule heating layers, which have been coated to the physically attached ones, is their lower thermal resistance [49]. Nickel-Chromium alloys have been extensively reviewed as ideal materials for heat-generating purposes as a result of electricity passage [49, 50, 61, 70].

Michels *et al.* [70] deposited the nichrome layer on top of an intermediary alumina one in their work. According to their observations, running a high electrical current through the resistive heating layers ended up damaging the nichrome layer causing a stoppage in the electrical current moving between the electrodes [70]. It was observed that even though the electrically conductive layer was fractured, the alumina layer was flawless, suggesting that probably the thermally induced stresses caused by the layers' thermal expansion coefficient mismatch have contributed to this issue [70].

Lopera-Valle and McDonald [71] successfully developed resistive heating layers consisting of Ni20Cr and NiCrAlY on fiber-reinforced polymer composite (FRPC) substrate via flame spray coating, which showed anti-icing characteristics when low electrical power was applied, and the testing temperature was -25°C by drawing only 10.1 W power. In their case, since the FRPC substrate could have been damaged during the coating deposition process, a layer of garnet sand was adhered to the FRPC surface, providing both the required thermal protection and the roughness for the sound coating deposition [71].

Rezvani Rad *et al.* [61] have shown that nichrome layers deposited by flame spray coating had higher electrical resistivity than the layers fabricated by HVOF and APS

methods due to the flame spray coated layers having a more porous structure. Though Rezvani Rad and McDonald [73] applied 500 W power to the prepared Joule heating layers, successfully benefiting from the nichrome layer's de-icing property in a short period, he has suggested against taking the same approach. They made the case that higher applied powers create a higher temperature gradient across the resistive heating layer itself, shortening the coating's life span [73]. It was also inferred that the thermally induced stresses generated during the heating and cooling cycles could lead to crack propagation, reducing the coating adhesion to the substrate [73].

1.4 Polymer Coating

For the MD membranes to function successfully, at least one hydrophobic layer should be integrated into its structure [8, 13, 74]. Since most inorganic materials are hydrophilic and possess relatively high thermal conductivity, they are not ideal for the fabrication of MD membranes [74]. Common polymers that have been used for the fabrication of MD membranes are polytetrafluoroethylene (PTFE), polypropylene (PP), and polyvinylidene fluoride (PVDF) [24, 74, 75].

Thermally-induced phase separation (TIPS), vapour-induced separation (VIPS), and non-solvent induced phase separation (NIPS) are three primary methods for fabricating membranes [76]. In the NIPS process, the immersion of cast polymer dope solution inside a bath containing a non-solvent solution triggers the polymer-solvent to diffuse in the non-solvent bath, leaving the polymer material behind [10, 76 – 78]. In the VIPS method, the non-solvent is introduced in the form of vapour, which, upon contact with the dope

solution, initiates the exchange stage [10]. In the TIPS method, temperature decrease contributes to the polymer solidification [25].

Among these methods, NIPS is the most versatile and facile method to prepare microporous MD membranes [75, 77]. Among the suitable polymeric materials for the MD mechanism, PVDF is one of those few options that is hydrophobic enough for MD application and could be fabricated by the straightforward and cost-efficient NIPS method [24, 75, 77]. In addition, PVDF possesses high chemical and thermomechanical stability that make it suitable for the MD process [24, 76 – 79].

1.5 Modeling

Even though few researchers have developed the heat-generating membranes, still, no work has been done regarding the mathematical modeling of heat generation on the surface of the membrane and its effects. The MD process itself has been modeled and investigated from a mathematical perspective. Although computational fluid dynamics (CFD) modeling could yield more detailed predictions, it requires comprehensive computations [80]. On the other hand, the Nusselt number-based approach provides fewer details; hence it is easier to be performed [80]. Noamani [81] developed a "self-sustained" mathematical model by combining the effectiveness-number of transfer units ($\in -$NTU) and finite difference methods. In this work, the predicted flux values were only 10% off the ones which were recorded during their experiment [81]. In the current study, inspired by the model developed by Noamani [81], in collaborative work with her, some parts of that mathematical approach were modified to help us simulate the mass and heat transfer of the system in which the Joule heating element has been integrated.

1.6 Thesis Objectives

The objectives of this thesis are as follows:

- Development of mesh-based heat-generating MD membranes
- Development of coating-based heating elements on steel plate substrates
- Analysis of the coating properties such as porosity, homogeneity, adhesion, and thickness
- Development of a proper MD cell to test the samples
- Investigation of the performance of the resistive heating elements in triggering the water purification in the MD process
- Development of a simple mathematical model to predict the performance of the Joule heating samples integrated into the MD process

1.7 Thesis Outline

Chapter 1 of this thesis an overview of the MD process for desalination, its advantages, and its downsides. The feasibility of the heat-generating materials being used as surface heating elements for the MD process and the efforts made in this regard are introduced. The efforts made to fabricate Joule heating coating layers and polymeric layers using the NIPS method and mathematical modeling of the MD process are also presented in this chapter.

In Chapter 2, the fabrication details of mesh-based heat-generating MD membranes are described, and the results related to microscopy characterization and heat generation in stagnant air are presented.

In Chapter 3, the fabrication details of Joule heating layers on steel plate substrates are described. The resistive heating performance of these coating layers in different environments is investigated in this chapter. Lastly, the effect of implementing such elements on the MD performance is explored.

In Chapter 4, the mathematical model developed in collaboration with Ms. Sadaf Noamani to evaluate the MD process's mass and heat transfer modes, coupled with Joule heating coating layers, is presented.

In Chapter 5, the major findings of this work are presented. This chapter also outlines the efforts needed to be made to optimize the integration of such coating layers into the water desalination membranes.

Chapter 2

2. Development and Performance Testing of Steel Mesh-Based Membranes

With the aid of the flame spray (FS) coating method, alumina (insulating) and nichrome (resistive heating) layers were deposited on woven steel meshes. The alumina layer's integrity was of great importance as it acted as the intermediate layer preventing electrons from leaving the Joule heating layer and passing through the steel mesh. In the coating process, the effect of different spray parameters such as the SOD, torch velocity, the pressure of added air to the flame, and implementation of the cooling system on the coating quality and the substrate was studied. The coated samples were sectioned by water jet cutting and were examined by scanning electron microscopy (SEM). By SEM characterization, the homogeneity and microstructural characteristics of the deposited particles were investigated. To fabricate copper terminals to serve as low resistant electrical connections, the possibility of cold spray coating of this material was also investigated.

To complete the fabrication of the MD membrane samples, the polymeric layer was cast on the backside of the steel substrate. The polymeric layer was added to be able to generate the required temperature difference across this new generation of MD membranes. Finally, the structure and heat generation capability of the fabricated membranes were tested by microscopy characterization and Joule heating tests.

2.1 Experimental Methods

2.1.1 Feedstock Powder

The powders adopted for this study were aluminum oxide ((Al_2O_3, AMDRY 6060, Oerlikon Metco, Westbury, NY, USA), Nickel-20wt.% chromium (Ni20Cr) (Metco 43F-NS, Oerlikon Metco, Westbury, NY, USA), and copper (SST-C5003, CenterLine, Ltd., Windsor, ON, Canada).

Based on the supplier's information, the size distribution of alumina, Ni20Cr, and copper powders was 5 to 45 μm, 10 to 63 μm, and 5 to 45 μm, respectively.

2.1.2 Substrate Preparation

The best options for the MD membranes are hydrophobic polymers. Not only these materials could be severely damaged by the heat generated during the thermal spray methods, but also the successful grit blasting of them, which is integral for good adhesion of the deposited coating to the substrate, faces many challenges. As a result, 304 stainless steel mesh (30 × 150 mesh size, McMaster-Carr, Elmhurst, IL, USA) was chosen as the substrate in this study. Although this mesh's pore size (95 μm) was much larger than what is required of the MD membranes, no finer meshes were found suitable for the FS process. Therefore, a compromise was needed between the FS and MD process requirements, which was made by selecting this particular mesh.

The meshes were cut down to the desired dimensions using a shear. The proper dimensions for the MD cell were 160 mm × 70 mm. For preliminary Joule heating tests, the mesh was cut down to 1-inch × 1-inch. Then the meshes were ultrasonically cleaned

while they were immersed in a dilute solution of water and detergent (Critanox, Alconox, White Plains, NY, USA). The ultrasonic cleaner was used for 15 minutes.

To benefit from the cooling system's effects, a unique substrate holder (aluminum made) was designed and fabricated by water jet cutting. As shown in Figure 2.1, the substrate holder being hollow created the possibility of the substrate to be cooled directly by forced convection while the coating deposition was in progress. The selection of aluminum as the material for this substrate holder was due to its high thermal conductivity and low density.

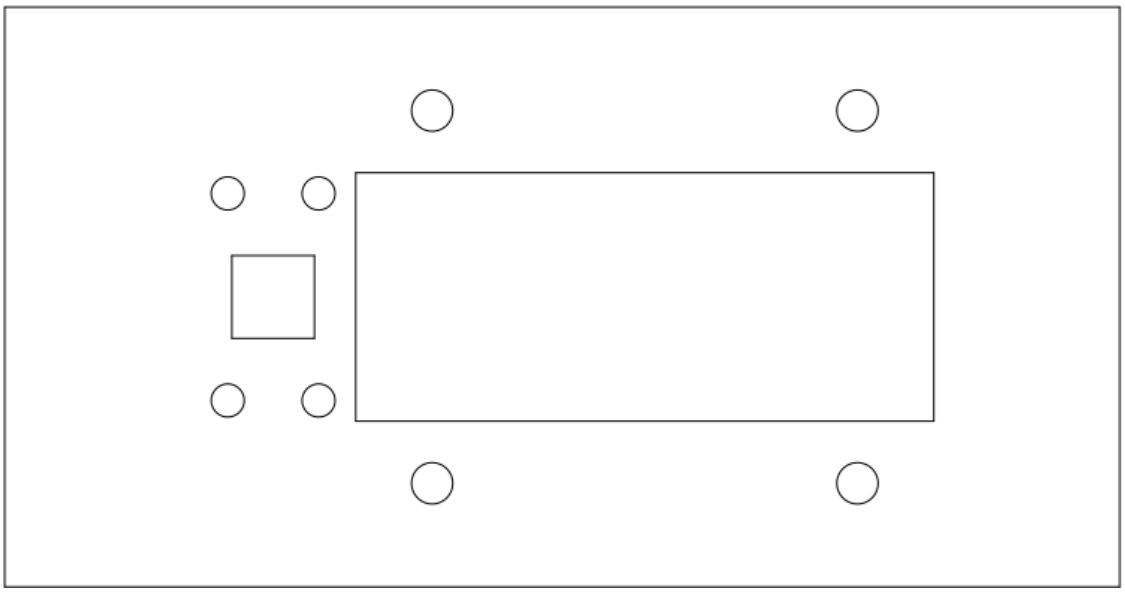

Figure 2.1 Substrate holder design

For the grit blasting part, the substrates were exposed to #24 alumina grit (Manus Abrasive Systems Inc., Edmonton, AB, Canada) being propelled at 90 psig at the substrate's surface. The grit blaster nozzle was held vertical to the surface, and one pass of 90 psig grit blasting on the surface was done. Also, for some samples, the substrate's backside was also

grit blasted with 60 psig pressure to eliminate the residual stresses caused by grit blasting. For the grit blasting process, the substrate was held manually on top of an aluminum-made block to provide support.

The steel mesh being easily deformable, posed an obstacle to the grit blasting process with the sample remaining in the original state. As a result, some samples were coated without being grit blasted. The steel meshes being composed of woven wires provided some surface roughness to a certain extent, but the coating delamination showed that the surface roughness of the substrates was not high enough to ensure proper coating adhesion. Therefore, the samples had to go through the grit blasting procedure. The deformation of the steel mesh as a result of one side of the steel mesh being grit blasted was severe, which made it difficult for the final product to be used as a membrane. Therefore, after grit blasting the feed side of the steel mesh by #24 grit propelled at 90 psig pressure, the backside of the substrate (permeate side) was grit blasted with 60 psig pressure. This approach evened out some of the stress stored inside the steel crystallographic structure and minimized the mechanical deformation of the substrate.

In Figure 2.2(a), only the left half of the feed side of the steel mesh was grit blasted. The severe deformation caused by grit blasting made this substrate useless for both the flame spraying and membrane distillation processes. But, when the backside of the sample was grit blasted at 60 psig, the mechanical deformation was reduced. As could be seen in Figure 2.2(b), some deformity was still present in this sample, but this sample could be implemented for our purposes.

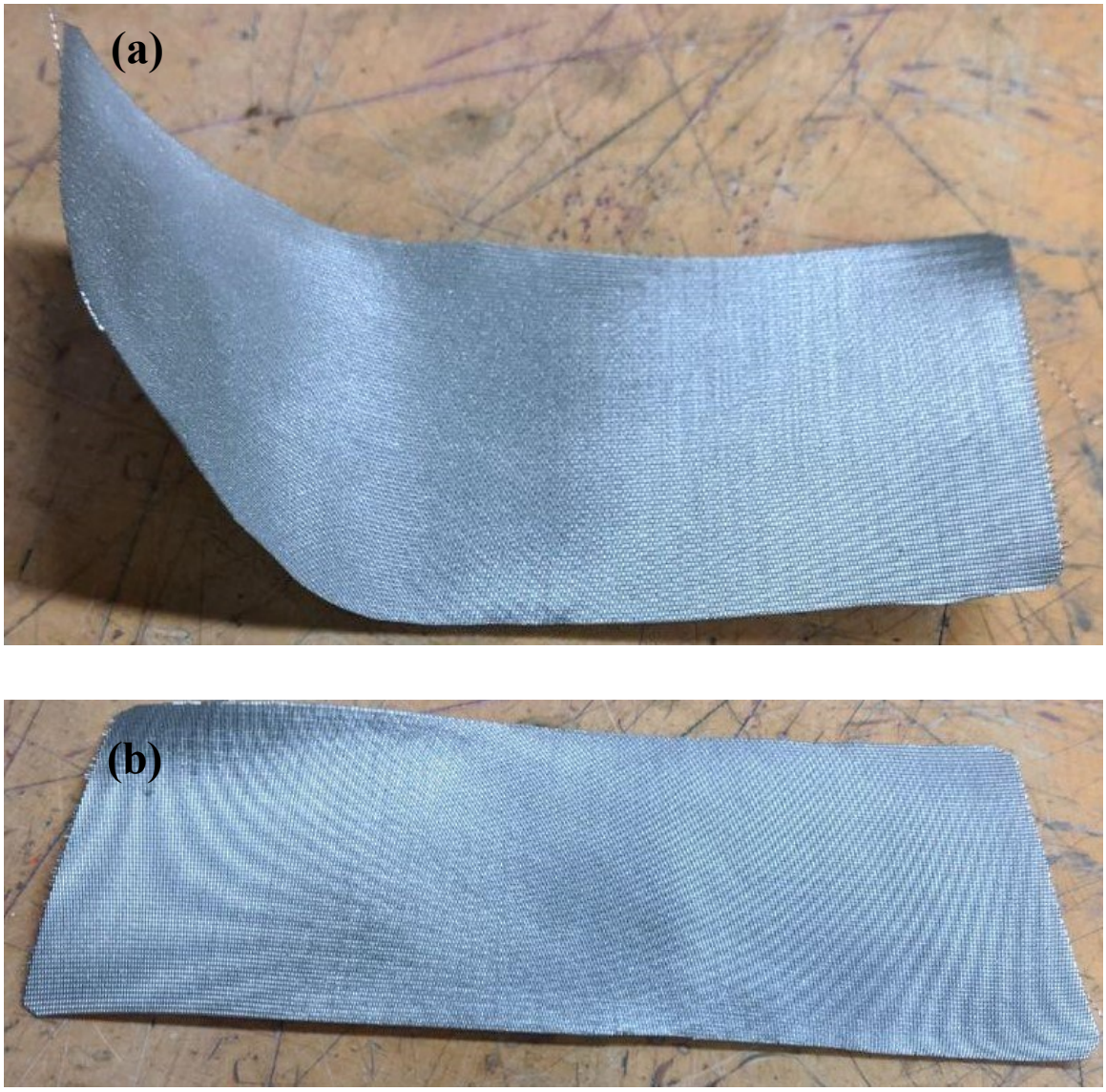

Figure 2.2 (a) Substrate deformation due to one side being grit blasted (b) Status of the substrate when both sides were grit-blasted

2.1.3 Spray Parameters

For the coating deposition, the flame spraying method was used. In this method, the feedstock powder was added to the powder hopper (5MPE, Sulzer Metco, Westbury, NY, USA). The feedstock material was carried by argon gas to be fed into the torch while the oxyacetylene flame was burning (6P-II, Oerlikon Metco, Westbury, NY, USA). For the

coating deposition process, a programmable robot arm (HP-20, Motoman, Yaskawa Electric Corp., Waukegan, IL, USA) carried the torch to fabricate homogeneous coating layers. For the alumina layer deposition, the spraying parameters established by Rezani Rad *et al.* [61] were used. Based on the obtained results, the spraying parameters such as the SOD and the pressure of added air to the flame were modified. Also, the effect of incorporating a cooling system, maintaining the temperature of the substrate while being coated was studied. Based on the established spraying parameters for alumina deposition, the Ni20Cr spraying parameters were developed. The parameters of the flame spraying process are presented in Table 2.1.

Table 2.1 Flame spray parameters

First layer material	Alumina [61]	Alumina	Alumina	Alumina
Acetylene flow [m^3/hr]	1.3	1.3	1.3	1.3
Oxygen flow [m^3/hr]	2.1	2.1	2.1	2.1
Air pressure [psig]	5	10	10	10
Argon pressure [m^3/hr]	0.56	0.56	0.56	0.56
Powder flow rate [FMR]	100	100	100	100
Robot speed [mm/s]	300	300	300	800
Stand-off distance [mm]	127	203.2	203.2	203.2
Number of preheating passes	1	1	1	1

Number coaing passes	5	5	5	16
Pause	No	No	After each 2 pass For 7 minutes	No
Cooling system	No	No	No	Yes
Increments [mm]	3	3	3	3
Second layer material		Ni20Cr		Ni20Cr
Acetylene flow [m^3/hr]		0.9		0.9
Oxygen flow [m^3/hr]		1.9		1.9
Air pressure [psig]		5		5
Argon Pressure [m^3/hr]		0.56		0.56
Powder flow rate [FMR]		60		60
Robot speed [mm/s]		300		800
Stand-off distance [mm]		228.6		228.6
Number of preheating passes		0		0
Pause		No		No
Cooling system		No		Yes
Increments [mm]		3		3

2.1.4 Polymer Casting

15 wt.% PVDF (Solef 1015/1001, Solvay, Alpharetta, GA, USA) and 85 wt.% DMAc (Sigma Aldrich, St. Louis, MO, USA) were added to a bicker. The bicker containing this

solution was on a magnetic stirrer for 24 hours at 50°C. After 24 hours, the solution was placed under a hood to go through a 24-hour degassing step. Prior to the casting process, the substrates were wetted, and the permeate side of the steel mesh was dried with a paper towel for a few minutes. After the completion of the degassing stage, the dope solution was cast on the permeate side of the steel meshes with a brush at the first stage. The samples were moved to a coagulation bath, consisted of DI water to initiate the demixing process. After leaving the samples for 24 hours in the coagulation bath, they were removed to dry. In the second stage of polymer casting, the whole process was followed, as described above, with the casting blade being used instead of the brush. The casting blade was moved at 10 mm/s by the automatic film applicator apparatus.

2.1.5 Microscopic Characterization

In order to conduct microscopic characterization on the heat-generating membrane structures, the samples were cut into 1-inch × 1-inch by water jet cutting. For the microscopic characterization of the prepared samples scanning electron microscope (SEM) (Zeiss Sigma 300 VP-FE, Carl Zeiss Canada Ltd., Toronto, ON, Canada) was utilized. In some samples, the top view of each layer was studied to determine the morphology of each coating layer. Also, the cross-section of the coated samples was analyzed to determine the thickness and porosity of each layer. The ImageJ software was used to determine the physical properties of the SEM images. The porosity analysis was simply done by comparing the cross-sectional area occupied by each phase.

2.1.6 Electrical Connection

The electrical terminals were fabricated by cold spraying of copper particles. The reason for the selection of cold spraying is the good adhesion and contact between the copper terminals and the Ni20Cr layer. Rezvani-Rad [50] has tested this approach, and his samples could generate the required heat. Therefore our first attempt was to deposit copper terminals via the cold spraying method.

Regardless of the spraying parameters, it was noticed that the copper particles could penetrate inside the membrane structure. This turned out to be an issue since the penetration of the copper particles provided easy pathways for electrons to leave the Ni20Cr layer and move through the lower resistance layer, which was the steel mesh. This phenomenon deprived the Ni20Cr layer of generating heat by the passage of electricity through its structure. Therefore the cold spraying process could not be implemented for the steel mesh-based membranes.

As a result, the electrical connections were made using copper tapes and alligator clips. The copper tape itself could not make good contact with the Ni20Cr layer. There was always some gap between the tapes and the surface of the Joule heating layer. Therefore the copper tape terminals mostly functioned as capacitors rather than resistors. But, when the copper tape was coupled with the alligator clips, the pressure applied by the clips ensured good electrical contact between the two materials.

2.1.7 Joule Heating Test

For the Joule heating experiments, 1-inch × 1-inch samples were chosen. The electrical connections were made by copper tape and alligator clips. For these tests, one

thermocouple (TC50, WIKA Instruments, Edmonton, AB, Canada) was attached to the Ni20Cr layer, while the other one was attached to the PVDF layer surface. The thermocouples were connected to a data acquisition module (SCXI-1600, National Instruments, Austin, TX, USA) for data collection. The electrical potential was imposed by a direct current (DC) power supply (1692, BK Precision, Yorba Linda, CA, USA). The parameters of the Joule heating tests are listed in Table 2.2.

Table 2.2 Joule heating test details

Name	Voltage (V)	Current (A)	Power (W)
SM-4W	1.5	2.7	4
SM-6W	1.8	3.2	6
SM-9W	2	4.5	9

2.2 Results and Discussion

2.2.1 Flame Spray Coating

The flame spray coating was done with different parameters and agents involved. For the first set of samples, the spray parameters established by Rezvani Rad *et al.* [61] were implemented. In this approach, the SOD was set 5 inches, and 5 layers of alumina were deposited on the steel mesh without any pauses in between each layer. The coated samples were severely oxidized and deformed. The deformation was so high that it caused coating delamination (Figure 2.3).

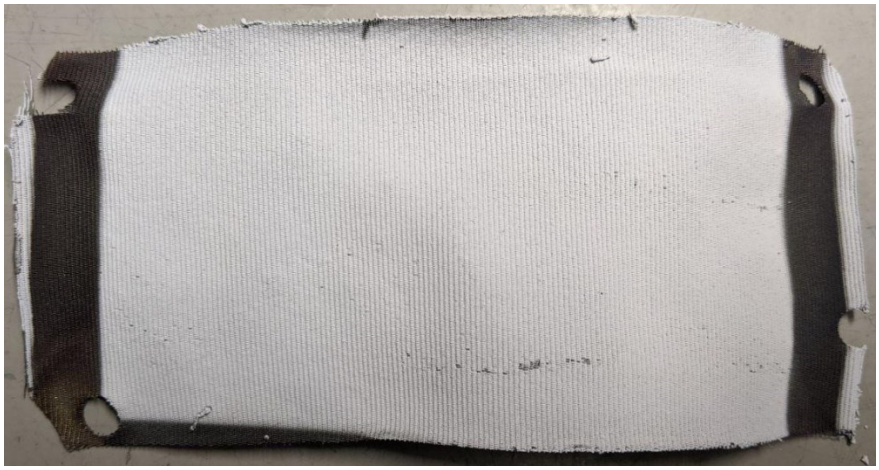

Figure 2.3 Status of the substrate and the deposited layer when spray parameters developed by Rezvani-Rad [50] were used

To reduce the exposure of the substrates to the heat generated by the oxyacetylene flame, SOD was increased to 8 inches. Although the coating did not get damaged because of the excessive heat, the high thermal expansion of the substrate during the coating process rendered it useless for the MD application. Therefore, after every two passes of the torch passing over the sample, the coating process was paused for seven minutes to alleviate the adverse effect of thermal expansion of the substrate.

In Figure 2.4, the difference caused by the pauses could be seen. These samples had much less thermally-induced deformation. Even though these samples could be easily coated with Ni20Cr, their severely oxidized structure was not desired. Since these mesh-based samples were supposed to function inside a corrosive environment such as saline water, it was desired to benefit from the high corrosion resistance nature of the stainless steel mesh. But the oxidation of this material during the FS process was compromising the resistance of this material to corrosion.

Figure 2.4 Effect of spray parameters on the thermally induced deformation of the substrate

To resolve this issue, the spray parameters could not be modified any further. It was found out that the adhesion of the alumina layers deteriorated when the SOD was higher than 8 inches. Moreover, although the pauses successfully reduced the degree of mechanical deformation, the oxidation problem could not be resolved by optimizing this parameter. The only practical approach was to benefit from a forced convective cooling system. The high-pressure air blown out of this system's outlet could help us control the substrate's temperature, preventing it from being oxidized. To create the opportunity to use this cooling system, it was needed for a new substrate holder to be designed.

As shown in Figure 2.1, the backless structure of the substrate holder made it possible for the substrate to be cooled down by forced convection. To mount the substrates on the substrate holder steel made wires were used. Although the forced convective cooling effect could keep the temperature low, the porous structure of the steel mesh created a challenge. Since the mesh was porous, some of the blown air could pass through the pores and reached the face of the sample. These air molecules acted against the homogeneous deposition of particles on the surface of the steel mesh. To overcome this challenge, a piece of aluminum

foil was attached to the backside of the steel substrate. The addition of this non-porous thin film created stagnation points. Therefore the air molecules were stopped upon impact to this surface, preventing them from reaching the other side of the steel substrate.

Additionally, since the aluminum foil had a very low thickness, its heat conduction was not slow enough to significantly influence the cooling effect. Figure 2.5 shows the effect of the cooling system on the reduction of substrate oxidation. Figure 2.5(a) depicts the severe oxidation of the samples which were coated without implementing the cooling system. On the other hand, Figure 2.5(b) and Figure 2.5(c) show the effect of the cooling system when the sample was exposed to it directly and with the aluminum foil playing the part of an intermediary layer between the cooling system and the substrate, respectively.

Figure 2.6(a) shows the sequence of the inorganic layers. Figure 2.6(b) and (c) portray the state of the alumina and Ni20Cr coating layers. It is obvious that since the thickness of the alumina and Ni20Cr layers was low, these coating layers imitated the texture of the steel mesh substrate. It could be inferred that the deposition of the coating layers has not compromised the porosity and the pore size of the support material. Therefore, the structure of the inorganic layers, coupled with their hydrophilic nature, pose negligible mass transfer resistance.

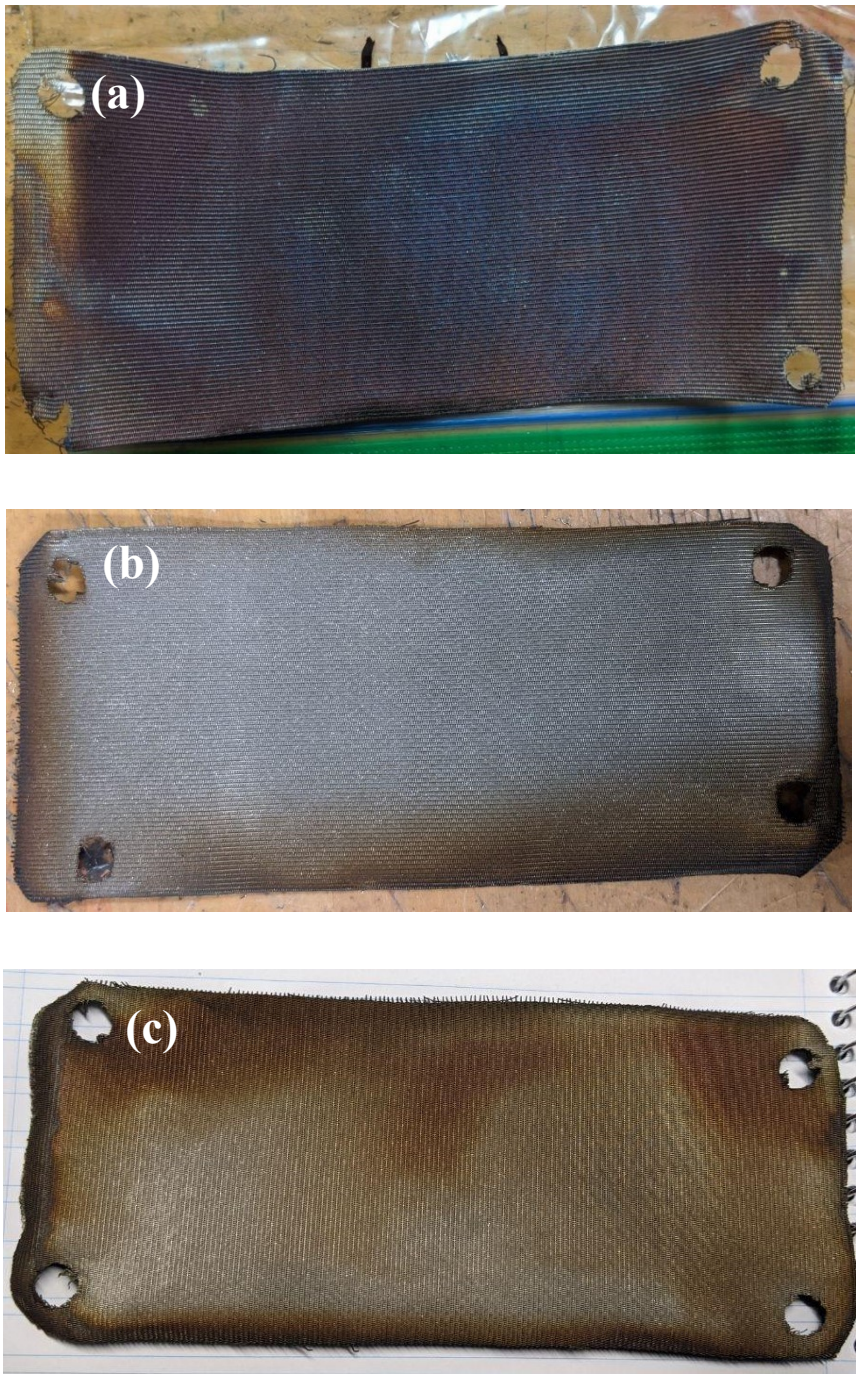

Figure 2.5 Oxidation of the substrates when (a) No cooling system was used, (b) Direct exposure to the cooling system, and (c) Indirect exposure to the cooling system (aluminum foil attached)

Cross-sectional images, e.g., Figure 2.6(d), suggest that the thickness of the alumina and Ni20Cr layers were 121.23 ± 11.85 (n = 12) and 67.16 ± 9 μm (n = 12), respectively. The porosity of the Ni20Cr layer was 2.9 ± 0.87 (n = 6), while the alumina layer had 14.45 ± 0.89 (n = 6) vol. %.

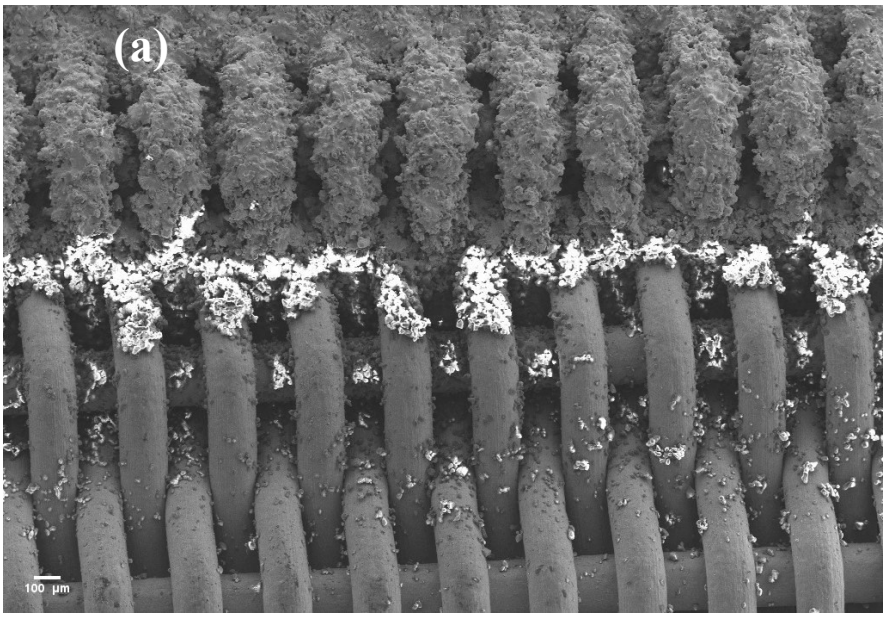

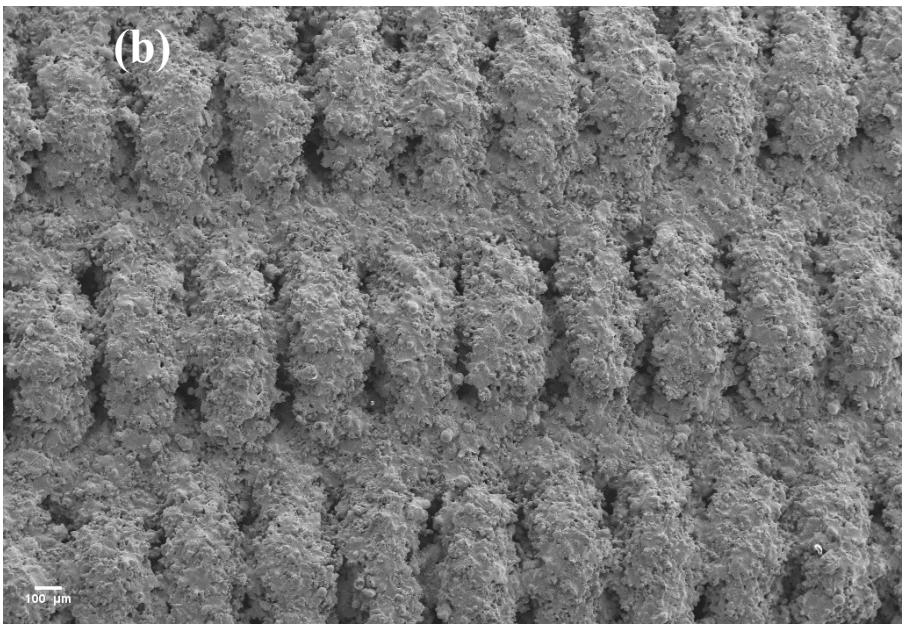

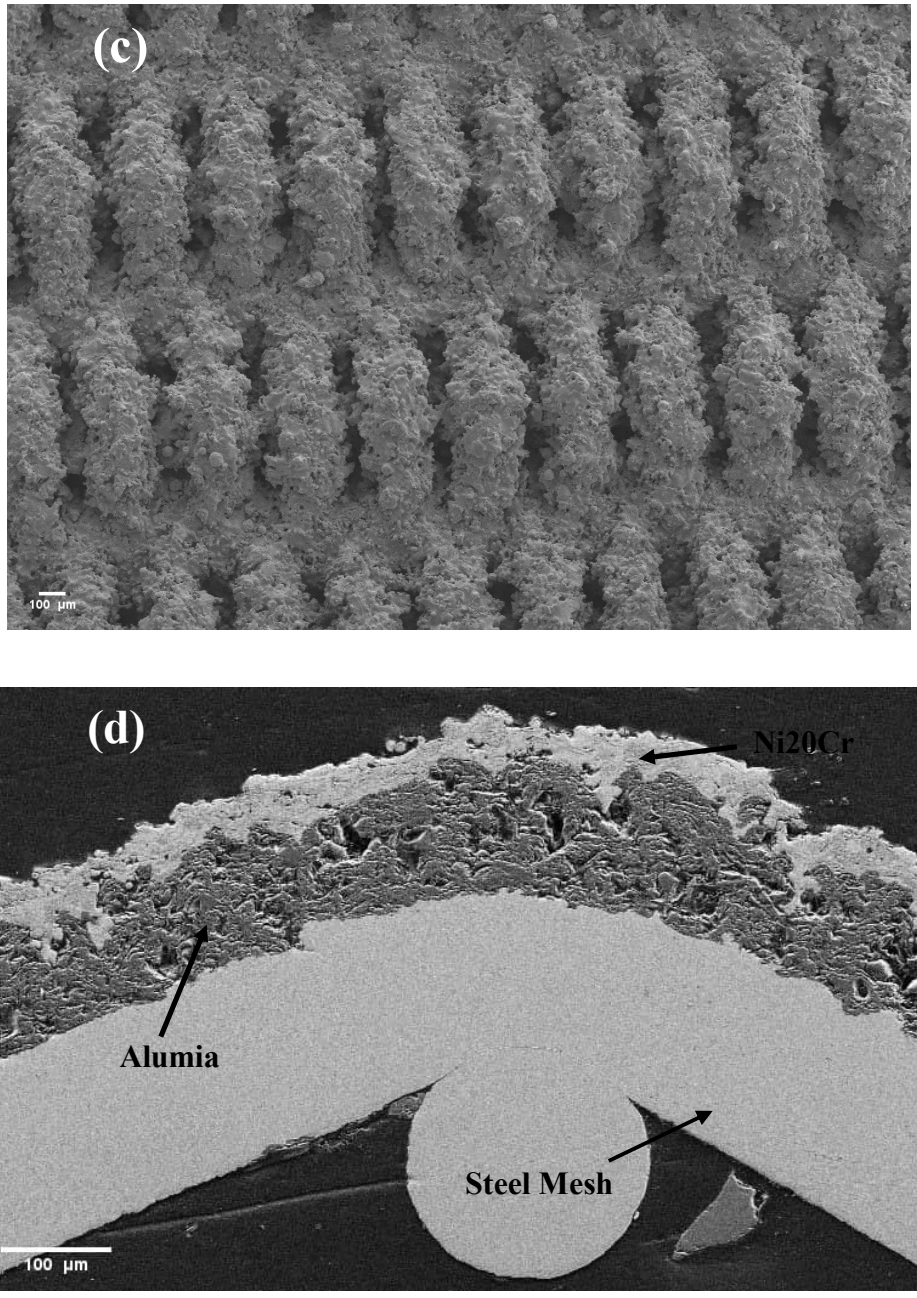

Figure 2.6 SEM images of the feed side (a) Sequence of each layer shown (b) Alumina layer (c) Ni20Cr layer (d) Cross-sectional view

2.2.2 Polymer Casting

The support material being porous posed many challenges for polymer casting. In the NIPS polymer casting method, the polymer dope solution is cast on the support material,

and it is immersed in a coagulation bath consequentially. But in our case, the viscous polymer dope solution could easily go through the pores and wet the feed side. This was not desired, as this polymer penetration could have made the Ni20Cr layer electrically insulating. We intended to allow the heat generated by the Joule heating layer to reach our target medium (saline water) firsthand, without the involvement of any intermediary layers. Therefore the conventional polymer casting method used for membrane fabrication could not be followed. To prevent the cast solution from reaching the feed side of the structure, the samples were wetted with water. Only the permeate side was dried with paper towels. Then the polymer solution was poured on the permeate side of the steel mesh. This approach prevented most of the dope polymer solution from reaching the feed side. This was achieved due to the coagulation process being triggered the moment the polymer solution was in contact with the coagulating agent (water).

In our attempts, it was found out that although the polymer solution could be cast with an automatic film applicator directly, however since there was not much control over the flow of the polymer solution, this approach faced some failures. Therefore, in the first polymer coating stage, the polymer solution was brushed on the permeate side of the steel mesh while it was held vertically. This way, gravity helped us have more control over the flow of the polymer dope solution. After the polymeric layer was formed in the coagulation bath, the casting process was done again, with the automatic film applicator being the casting equipment.

In this particular approach, the non-homogeneous layer cast by brush functioned as a barrier preventing any polymer solution from reaching the feed side. The reason that the polymeric layer could act as a barrier and the steel mesh could not was the sheer fact that

the polymeric layer had pores much smaller than the steel mesh. Even though this first polymeric layer was not homogeneous in terms of thickness, the second layer, coated using an automatic film applicator, ensured that the final polymeric layer was homogeneous. Figure 2.7 shows the feed side of the complete membrane. Although the traces of the PVDF layer could be seen around the edges and the holes of the structure, not much could be found in the main part of the feed side, which showed the proper fabrication of the samples without any of its functionalities being compromised.

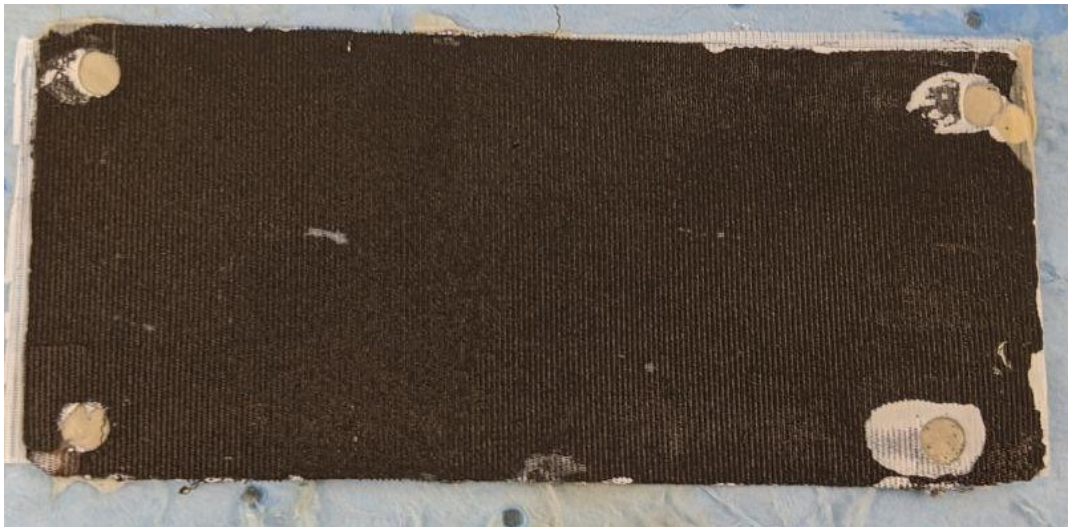

Figure 2.7 Complete membrane structure

In order for this mesh-based membrane to function as expected in an MD setup, it was required for the membrane to create a significant temperature difference across itself. That was one of the reasons that polymer was added to the backside to make sure the required driving force was provided. Since it was very challenging to create 30-40˚C across a heat-generating 1 mm thick structure, it was needed for the polymeric layer to be thicker than conventional MD membranes used for this procedure. Figure 2.8, the cross-sectional SEM image of the heat-generating membrane, shows the thickness of the polymeric layer. The

approximate thickness of the PVDF layer was 205 ± 71.58 (n=12) μm based on our calculations. The unique nature of the mesh caused this significant error. Figure 2.8 depicts this perfectly. It could be seen that at particular locations, the polymer layer has more thickness than others because of the wavy structure of the mesh.

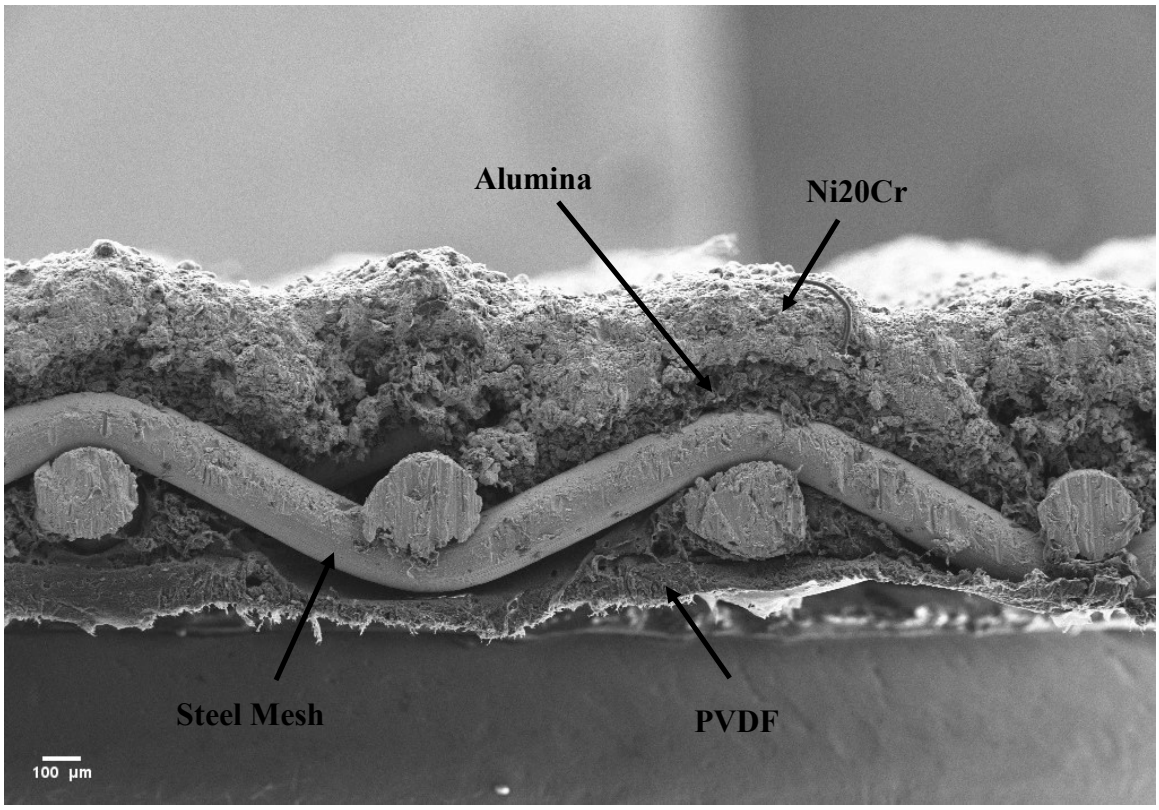

Figure 2.8 Cross-sectional image of the complete membrane

Since, at this stage of the project, the thermal performance of the polymeric layer was much more important than its hydrophobicity, no attempts were made to investigate its hydrophobicity prior to its heat-insulating performance getting verified by Joule heating experiments.

2.2.3 Joule Heating

For the Joule heating tests, stagnant air was chosen as the preliminary environment. Interestingly we could only generate heat while testing our 1-inch × 1-inch samples. Our experiments showed that with low voltages being applied, the Ni20Cr layer had the capability to generate heat. It was also evident that the polymeric layer was working as planned, creating a relatively high-temperature difference across the membrane. The reported temperature difference might not seem like a big deal, but it should be remembered that this temperature difference was achieved across a 1 mm thick sample while it was generating heat. The fact that we could not use any material other than alumina for the dielectric layer did not help our goal of creating a significant temperature difference. Unlike many ceramic materials, alumina is a very heat conductive material that serves very well in Joule heating de-icing components. But in our application, the alumina layer was not helping our cause from a heating standpoint.

As is shown in Figure 2.9, higher applied powers resulted in a higher temperature difference across the membrane structure. The reason behind this phenomenon could be the low heat conductivity of the PVDF layer. As a result, the heat generation rate and the temperature rise on the feed side offset the rate of conducted heat through all layers of structure to increase the temperature of the permeate side. It should be noted that, as a direct result of the more power being applied, both the recorded feed and permeate temperatures were higher.

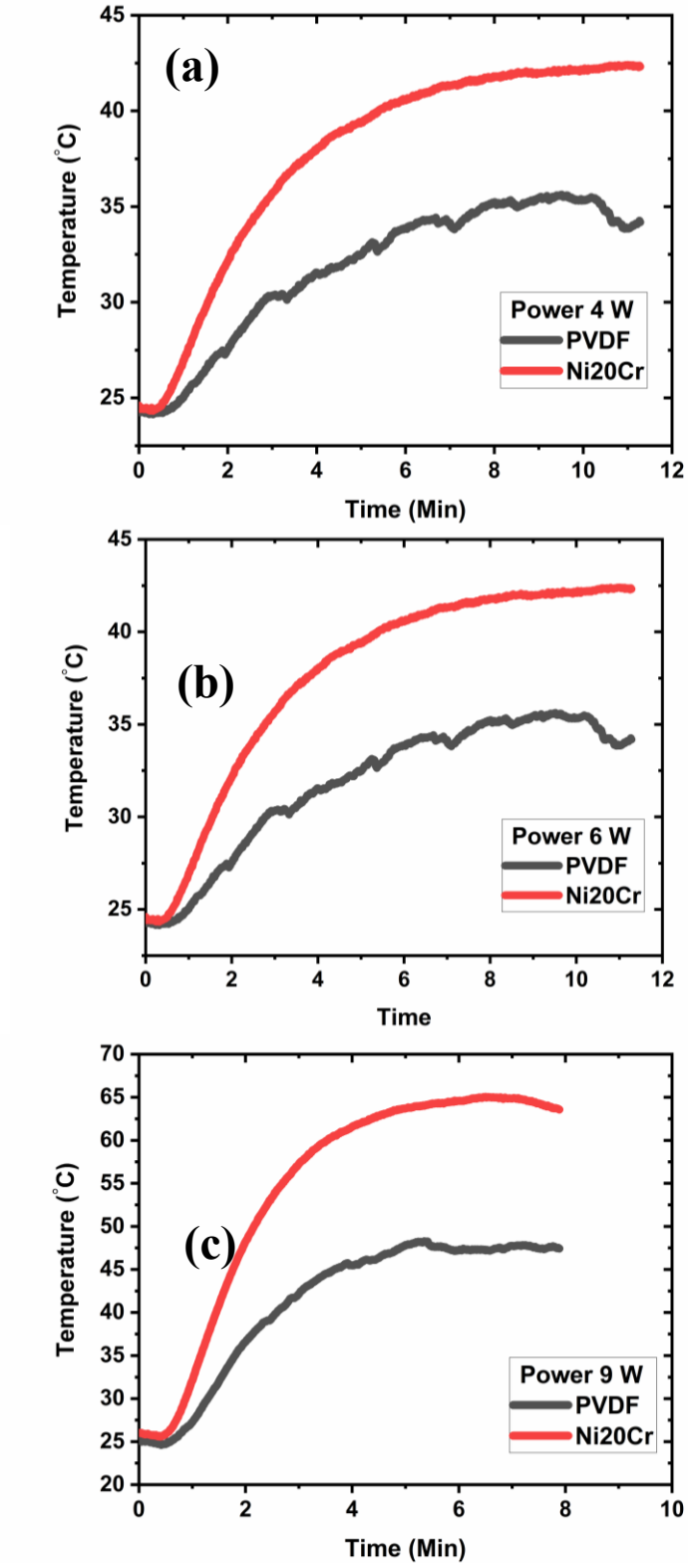

Figure 2.9 The temperature recordings of the Jole heating tests in stagnant air (a) 4 W (b) 6 W (c) 9 W

The same results could not be seen from full-size samples (160 mm × 70 mm). Regardless of how optimized the spraying parameters were or how careful the samples were handled, there were always some signs of short-circuiting while testing these samples. Our hope was that the addition of the polymeric layer might aid us in preventing the short-circuiting from occurring, but it simply did not serve as expected. The only difference between the full-size samples and the small ones was their dimensions. It was speculated that the larger size of the samples led to higher thermal expansion. This thermal expansion occurs for all metallic materials, but the fact that this material was made from wires made it much more sensitive to this natural phenomenon. Another factor that contributed to this failure was the incomplete combustion of the implemented flame. This led to the deposition of microscopic carbon particles while the FS was being carried out. All the factors mentioned coupled together resulted in a more fragile alumina layer, which could have been penetrated by electrically conductive carbon particles. Also, it should be remembered that even when bulk substrates are coated with alumina via FS, the porous structure of the alumina layer, which is a natural consequence of this coating process, is on its own a concern. When the used substrate is a porous one, it becomes much easier for short-circuiting to occur. This structure could work as a heat-generating membrane, but at least not with FS as the coating process.

2.3 Conclusion

FS and NIPS methods were implemented to fabricate steel mesh-based heat-generating membranes. Starting with the sample preparation, it was shown that since the steel mesh substrate was quite prone to deformation, one side grit blasting of those substrates rendered them useless for any application. Therefore, the substrates' backside was grit blasted at 60

psig to even out the stress induced by the grit-blasting process. Even though the substrate still was not in its original state, the deformation was not severe enough to prevent this substrate from being coated and implemented.

Moving on to the FS process, the spraying parameters suggested by other scholars was used. Since the nature of the substrate utilized in this study was much different from those reports, the severe thermal expansion of the sample due to the high temperatures of the FS process and the substrate's unique nature damaged the deposited coating. The SOD being changed from 5 to 8 inches and adding more air to the flame made it possible to successfully deposit the alumina layer on the steel mesh. But, the severe thermally-induced deformation still was an issue. To overcome this challenge, between every two passes, the coating process was paused for seven minutes. These pauses helped not to overwhelm the substrate with the heat generated during the FS. Even though the samples had much less deformation, them being heavily oxidized during the coating process was another unsolved issue. To fix this issue, the spraying parameters could not be further modified without the coating quality being compromised. Therefore a backless substrate holder was designed to benefit from the forced convective cooling system that we had in our possession.

Doing so, not only were the samples no longer deformed, but also the oxidation was no longer an issue. It was noticed that when the substrate was directly exposed to the air cooling, because of the porous nature of this material, the pressured-air could act against coating deposition. Hence the obtained coatings were not homogeneous. This problem was solved by attaching a piece of aluminum foil to the backside of the substrate while it was being covered by coating materials. The foil's non-porous structure created a series of stagnation points, stopping the air from interfering with the coating deposition. Also, since

the aluminum foil was very thin, its heat conduction was not slow enough to render this solution fruitless. Even though the oxidation signs were more obvious using the aluminum foil as a backing layer, it was necessary to compromise between the coating quality and the oxidation of the substrate. With the aluminum layer coating being established, the Ni20Cr coating did not pose any particular challenges on its own. The cooling system was again implemented to control the temperature of the sample. The SEM images showed the coating layer was deposited with good quality. Also, since the coating layers were not thick, they both imitated the structure of the steel mesh. This showed that the inorganic part of the membrane could not impose a high mass transfer resistance. This way, a unique functionality was added to the membrane structure, while its conventional function was not affected by this new feature.

Having fabricated the dielectric and electrically conductive layers on one side of the steel mesh, the Joule heating property of the sample was needed to be examined. But since in the MD process, the high-temperature differences across the membrane yield promising results, prior to testing the Joule heating potential of the samples, on the other side of the steel mesh, PVDF was cast. The addition of this polymeric layer would have helped us create a significant temperature difference across this structure. Again the unique nature of the substrate created many challenges regarding the polymer casting step. The approach could not be made similar to conventional ones since the porous structure of the sample would allow the polymer dope solution to reach the other side of the sample, which was not desired. Therefore, to cast the polymer without compromising the electrical conductivity of the other side (feed), the samples got wet. Only the permeate side got dried by a paper towel. The first polymeric layer was cast on the permeate side using a brush,

while the sample was held vertically to use the gravity in our favor. After the polymer solidification, this process was repeated again with only one difference, instead of the brush, an automatic film applicator was used. This way, the polymeric material did not interfere with the resistive heating layer structure, and also the final polymeric layer was homogeneous. With the membrane structure being complete (consisting of all the layers), the Joule heating property was examined in stagnant air.

The Joule heating tests of the small samples were accompanied with promising results. 9 W of power resulted in the feed side reaching 63°C, while the thermocouple attached to the permeate side recorded 47°C. Although 16°C temperature difference across the membrane is not ideal for the MD process, it is worth noting that this temperature difference was made across a structure thinner than 1 mm while generating heat. Surprisingly, the full-size samples (160 mm × 70 mm) could not generate heat. This could be attributed to short-circuiting. It was concluded that four distinct phenomena contributed to the short-circuiting of the full-size samples. First of all, the porous structure of the alumina layers coated by the FS process is problematic. As explained in the first chapter, the porosity of this layer could lead to short-circuiting. Furthermore, when you add the effects of the porous structure of the mesh substrate coupled with its high thermal expansion, the alumina layer becomes more porous. This porosity might not cause any issues on its own under the testing conditions considered for these samples, but if conductive particles penetrate inside the structure of alumina, they could provide easy pathways for the electrons to flow through the steel mesh structure rather than the resistive heating layer. In our case, since the acetylene used for coating deposition did not oxidize completely, carbon particles were also deposited with the alumina particles. It was

speculated that the porous structure of the alumina layer coupled with the penetration of electrically conductive materials such as carbon particles could have led to the short-circuiting issue.

Although the results of this chapter don't seem to be promising for the MD process, with the right equipment, the structure described here could serve as a heat-generating membrane. For instance, the FS process is not an ideal process to deposit the alumina particles. This step of the process being done with plasma spraying might yield better results.

Chapter 3

3. Development of Steel Plate-Based Joule Heating Elements for the MD Process

The heat-generating failure of the steel mesh-based membranes showed us that the substrate needed to be changed. Therefore instead of steel mesh, a steel plate was used. To make it penetrable by water, prior to being coated, a few holes were drilled in its structure. The bulk structure of the substrate did not pose any challenges like the mesh substrates. After the completion of the FS process, the Joule heating samples were tested in stagnant air, static, and dynamic water environments. The heat generation of the element and its effect on the MD process were investigated. With the aid of SEM characterization, we could analyze our samples after being tested in corrosive environments to determine the chemical composition of the formed oxides. Finally, the quality of the distilled water was examined by analyzing its chemical composition to ensure that the addition of the Joule heating element had not compromised the quality of the purified water.

3.1 Experimental Methods

3.1.1 Materials and Sample Preparation

In this study, alumina (Al_2O_3, Amdry 6060, Oerlikon Metco, Wetsbury, NY, USA) and Nichrome (Ni-20wt.% Chromium, 43F-NS, Oerlikon Metco, Wetsbury, NY, USA) powders were used.

A 26 gauge galvanized steel sheet was cut into 160mm × 70mm samples using ordinary snips. To remove the zinc layer, the samples were grit blasted at 90 psig air pressure with #24 alumina grit (Manus Abrasive Systems Inc., Edmonton, AB, Canada) and were left in vinegar for 24 hours. The obtained carbon steel substrates were grit blasted at 90 psig before the coating deposition. To make this structure penetrable by water, three holes were drilled in the substrate using a 5/32 inch drill bit.

3.1.2 Flame spray coating

To deposit the alumina and nichrome/alumina coating layers, the oxyacetylene flame was chosen as the heat source. The powders were fed into the flame spray torch (6P-II, Oerlikon Metco, Westbury, NY, USA) from the volumetric powder hopper (5MPE, Sulzer Metco, Westbury, NY, USA). The flame spray torch was mounted on a programmable robot arm (HP-20, Motoman, Yaskawa Electric Corp., Waukegan, IL, USA) to deposit homogeneous coatings. The spray parameters for each powder are presented in Table 3.1.

Table 3.1 Flame spray coating deposition parameters

Parameters	Alumina	Ni20Cr/Alumina
Acetylene flow [m^3/h]	1.3	1.3
Oxygen flow [m^3/h]	2.1	2.1
Air pressure [psig]	10	10
Argon pressure [m^3/h]	0.56	0.56
Powder flow rate [FMR]	100	60
Robot speed [mm/s]	300	300
Stand-off distance [mm]	203.2	203.2
Preheating passes	4	0
Coating passes	5	3
Increments [mm]	3	3

The nichrome and alumina particles were mixed in various percentages and coated after the alumina layer was deposited on the steel substrate. The weight percentage of each powder has been mentioned in Table 3.2.

Table 3.2 Composition of the Joule heating layer

Sample Name	Nichrome wt.%	Alumina wt.%
S50	50	50
S65	35	65

With the aid of a scanning electron microscope (SEM) (Zeiss Sigma 300 VP-FE, Carl Zeiss Canada Ltd., Toronto, ON, Canada), the thickness, porosity, and chemical composition of the coating layers were determined. For cross-sectional analysis, the samples were fixed in multi-clips (Ted Pella, Inc., Redding, CA, USA) and cold mounted in an epoxy resin (LECO, Mississauga, ON, Canada). The mounted samples were ground and polished to prepare them for cross-sectional SEM characterization. The image analysis was done with the ImageJ software aided in the process of calculating the thickness, the porosity, and the chemical composition of the coating layers.

3.1.3 MD Cell

In order to be able to integrate the prepared samples into the MD process and investigate their influence, the commercial MD cells could not be used. Therefore, a new cell was designed to apply the novel changes without compromising the MD cell's original function. The material chosen for the MD cell was acrylic because of its relatively high working temperature, good machinability, and reasonable cost.

Figure 3.1 shows the details of the MD cell designed for this study. In the half-block allocated to the feed side, two rectangular pockets were considered, which were supposed to house the copper terminals and the electrical connections. The rectangular holes were only a couple of millimeters deep and were connected to thorough circular holes. The circular holes were machined to be the gateways of the thermocouple wires into the cell. Also, since it was predicted that some water might leak from those holes, a shallow groove was designed for o-ring placement, and the outlet of the holes was threaded so that they could be connected to tubes to circulate the leaking feed water back to the feed tank if needed. It is worth mentioning that o-ring grooves were designed to surround the rectangular pockets not to overwhelm the circular o-rings by being exposed to too much water. Also, two 10 mm wide o-rings were used inside the rectangular pockets to ensure that there was no water leakage from those holes carrying thermocouple wires. A 1 mm deep rectangular groove was considered to mount the Joule heating sample in the half cell allocated to the permeate side. This way, the thickness of the membrane itself could not cause any leakage.

To test the MD cell, a 1 mm thick layer was fixed at the permeate side, and on top of it, one layer of commercial PTFE membrane (PTFE laminated membrane filters, 0.45 Micron, 300 x 300 mm, SterliTech,) was fixed facing the feed side. This experiment was done with 6 liters of saline water (10 gr/lit NaCl) contained in the feed tank.

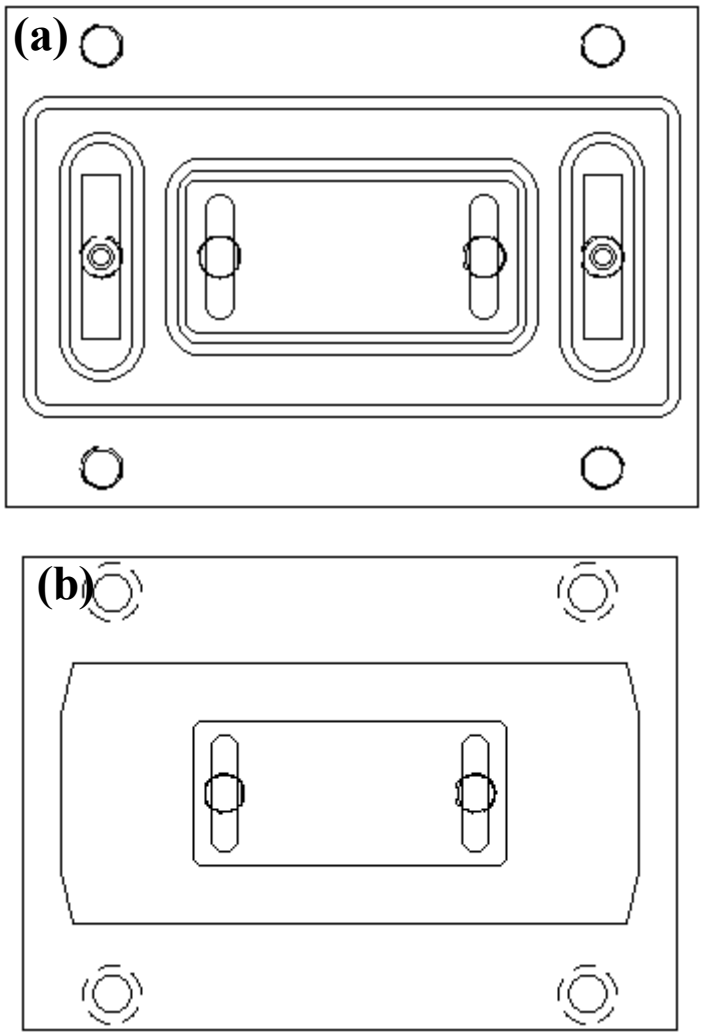

Figure 3.1 The design of the MD cell (a) feed and (b) permeate

3.1.4 Resistive Heating

The main parts of the electrical circuit were a DC power supply (1692, BK Precision, Yorba Linda, CA, USA) and an H-bridge (BTS7960 motor driver board, Aideepen, Shenzhen, Guangdong, China). A fan was used to prevent the H-bridge from overheating and being damaged as a result. A data acquisition system (USB-6000, National Instruments, Austin, TX, USA) controlled by a LabVIEW program, which was written in-

house, was implemented to set the H-bridge working frequency. The Joule heating tests were done in three different environments.

3.1.4.1 In Stagnant Air

The electrical connections were made with the aid of alligator clips and copper tapes. For the tests that the sample was exposed to stagnant air, one thermocouple (TC50, WIKA Instruments, Edmonton, AB, Canada) was attached to the surface of the nichrome/alumina layer. On the other end, the thermocouple was connected to a DAQ (SCXI-1600, National Instruments, Austin, TX, USA). In this part of the experiment, since the environment could not induce electron leakage, the H-bridge was not part of the electrical circuit. The details of the tests are organized in Table 3.4.

Table 3.3 Parameters for Joule heating tests in stagnant air

Name	Voltage (V)	Current (A)	Power (W)
S50-Air-6W	2.6	2.4	6
S50-Air-11W	3.5	3.2	11
S50-Air-20W	5	4	20
S50-Air-27W	6	4.5	27

3.1.4.2 In Stagnant Water

An insulated glass bowl was selected to examine the Joule heating coating layer's performance in stagnant water. The details of the experiment are listed in Table 3.4. The temperature recording was done via two thermocouples, one attached to the surface of the sample and the other immersed in the bulk water. In these tests, the voltage was set at 6 V,

and the drawn power was 40 W. The electrical connection was made with copper tape and alligator clips.

Table 3.4 Parameters for Joule heating tests in stagnant water

Name	Water Composition	Frequency (Hz)
S50-SW-DI	DI Water	40
S50-SW-1grlit	1 g/L NaCl/Water	100
S50-SW-5grlit	5 g/L NaCl/Water	1000
S50-SW-10grlit	10 g/L NaCl/Water	1000

3.1.4.3 MD test

For Joule heating tests conducted in the MD cell, the electrical connection was made outside the cell. To prevent the alligator clip from piercing the copper tape and damaging the connection, a piece of copper plate was also used as support for the copper tape. The pressure applied by both the MD cell and the alligator clips ensured a proper electrical connection between the sample and the rest of the circuit. Figure 3.2 shows the MD cell setup and electrical connections.

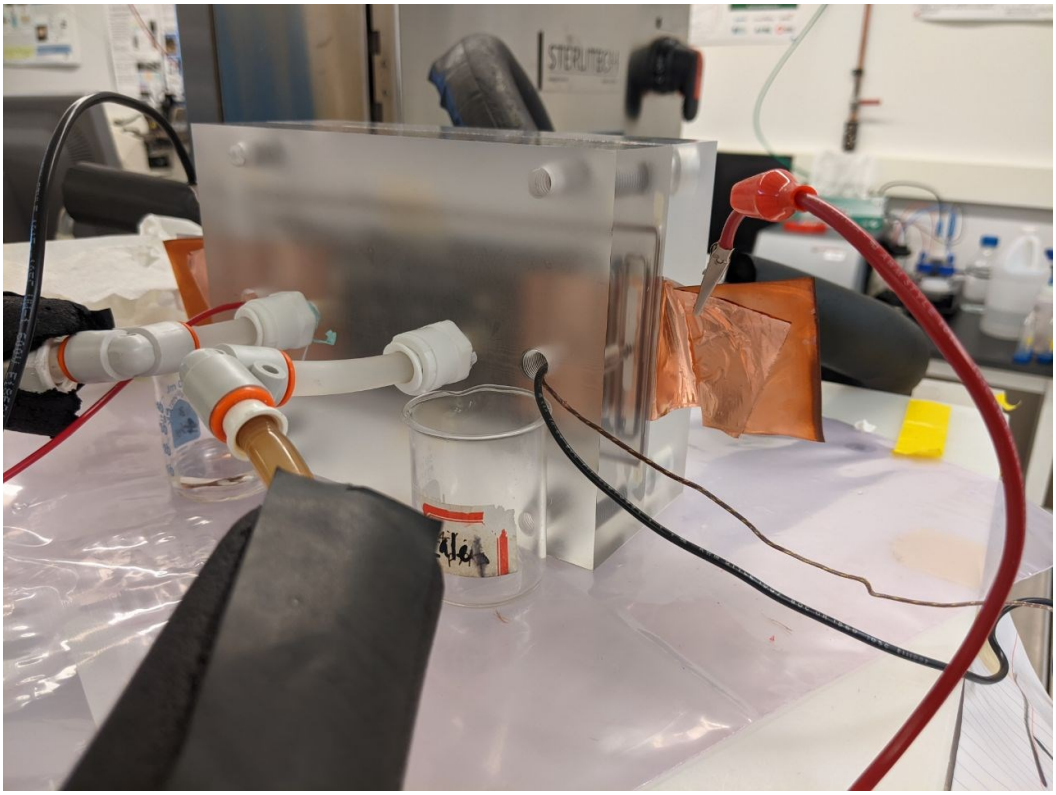

Figure 3.2 Dynamic water (MD) test setup

To test the heating capability of the fabricated samples in a dynamic environment, the sample was mounted in a specially designed MD cell. Four thermocouples were attached to the active area of the feed half block. Only the thermocouple temperature readings showing the average temperature of the active area have been used in this report. The details of the experiment are mentioned in Table 3.5.

In all the tests, the permeate flow rate was set at higher values than the feed flow rate. Since a higher cooling rate on the feed side induced by water flow was not desirable, the feed flow rate was kept at the minimum value defined by the system (0.2 LPM). On the other hand, the presence of a heat-generating source close to the PTFE membrane could have caused a temperature drop across the membrane itself, weakening the distillation's

driving force. Therefore, the permeate side's flow rate was chosen to be higher (0.4 LPM) to enforce a more potent cooling effect on the permeate side of the membrane. Last but not least, it should be mentioned that all the MD tests were conducted in the counter-current mode, meaning that the feed water inlet was placed on the side that the permeate water outlet was fixed.

Also, since the nichrome/alumina layer was conducting electricity in a corrosive environment, the formation of oxide layers on top of our Joule heating coating layer was expected. To make sure that the Joule heating layer itself did not take part in the electrochemical reactions occurring in the cell, samples were cut down to 1-inch × 1-inch with the help of water jet cutting. Thereafter surface of the samples was studied to determine the chemical composition of the oxide layers. This approach helped us confidently ascertain whether the Joule heating layer was deteriorated while operating.

To ensure that no contaminant was added to the permeate water simply due to the Joule heating sample's implementation, some water was removed from the bottom of the permeate tank for chemical composition analysis. This analysis was done via inductively coupled plasma mass spectrometry (ICP-MS). Also, to further understand the role of the PTFE membrane in limiting the domain of the contaminants to the feed side of the setup, the used membranes were analyzed with the SEM microscope, and the components detected with the help of the microscope were examined with energy-dispersive X-ray spectroscopy (EDX).

Table 3.5 MD tests parameters

Name	Water Chemical Composition	Feed Flow Rate (LPM)	Permeate Flow Rate (LPM)	Frequency (kHz)	Power (W)
S65-MD-2grlit-40W	2 g/L NaCl/Water	0.2	0.4	1	40
S65-MD-2grlit-50W	2 g/L NaCl/Water	0.2	0.4	1	50
S65-MD-2grlit-60W	2 g/L NaCl/Water	0.2	0.4	1	60
S65-MD-2grlit-70W	2 g/L NaCl/Water	0.2	0.4	1	70
S65-MD-2grlit-80W	2 g/L NaCl/Water	0.2	0.4	1	80

3.2 Results and Discussion

3.2.1 Flame Spray Coating

One of the questions which might be raised about the flame spraying parameters could be the number of pre-heating passes. Since the original substrate that was acquired for this study was galvanized steel, the zinc coating could have made it impossible to deposit the desired coatings. The reason for this phenomenon is the significant mismatch between the thermal expansion coefficient of the zinc coating and the alumina layer. Our initial attempt to remove this galvanization layer, which was done with grit blasting and immersion of the substrate inside vinegar, could only remove the zinc layer to a certain extent. It was realized

that in order to have a good coating adhesion, the pre-heating step had to be done in 4 passes. Any fewer passes led to poor coating adhesion and delamination. Figure 3.3 shows the influential role the number of preheating passes play, ensuring a proper alumina coating adhesion to the substrate in this particular case.

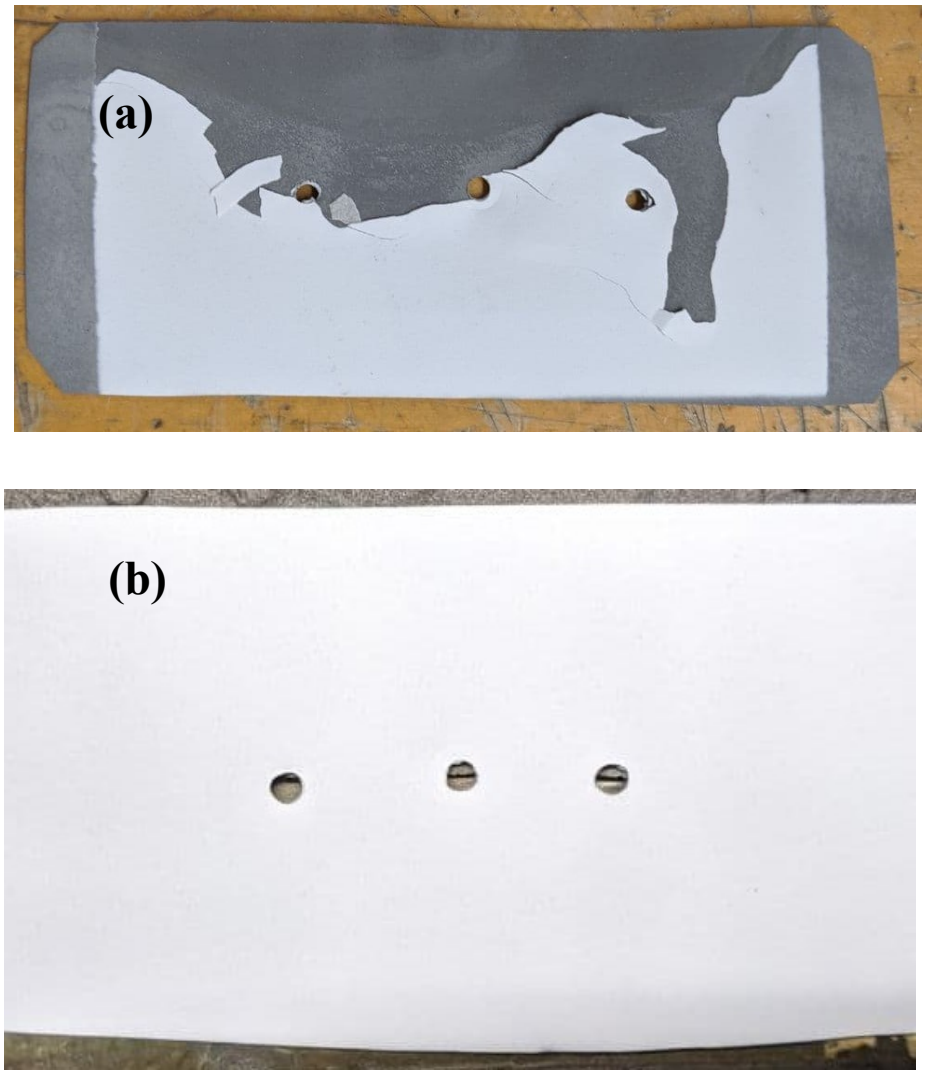

Figure 3.3 Effect of number of preheating passes (a) Fewer than 4 passes (b) 4 passes

The SEM characterization helped us determine the thickness and the porosity of all the layers. Also, since a mixture of nichrome/alumina was used for the resistive heating layer, it was important to determine the chemical composition of this layer. Although the weight

percentage of each powder was known before being added to the powder hopper, the flow of each powder was different from the other. For example, based on our observation, it was evident that the nichrome powder had much better flowability and adhesion than the alumina particles when coated. Therefore one of the concerns regarding the mixture of these two powders being used simultaneously for coating deposition was the dominant deposition of the nichrome particles due to their superiority. As a result, it was needed to know how much was the share of each powder in forming the Joule heating layer. The main reason why mixtures of these powders were used to fabricate the resistive heating layer was our desire to increase the resistance of this layer, not to overwhelm the implemented H-bridge when high powers were drawn. Because most available commercial H-bridges lack proper heat sinks, as a result, when the components of the circuit draw a high electrical current, the H-bridge could be damaged.

Figure 3.4(a) and (b) show the cross-section of the S50 and S65 samples, respectively. As expected, the alumina layer (the darker layer) had high porosity. The penetration of the nichrome particles (bright layer) into the structure of the alumina layer proves that some of the pores of this layer were open. The alumina layer thickness for the S50 sample was 237.73 ± 14.97 μm (n = 25). This number for the S65 sample was 236.95 ± 12.19 μm (n =38). The nichrome/alumina layer thickness was 75.99 ± 9.78 μm (n = 14) and 58.75 ± 8.95 (n = 30) μm for the S50 and S65 samples, respectively. The porosity of the alumina layer in the S50 sample was determined to be 20.73 ± 1.24 vol.% (n = 11), while this number for the S65 sample was 22.17 ± 2.56 vol.% (n = 15).

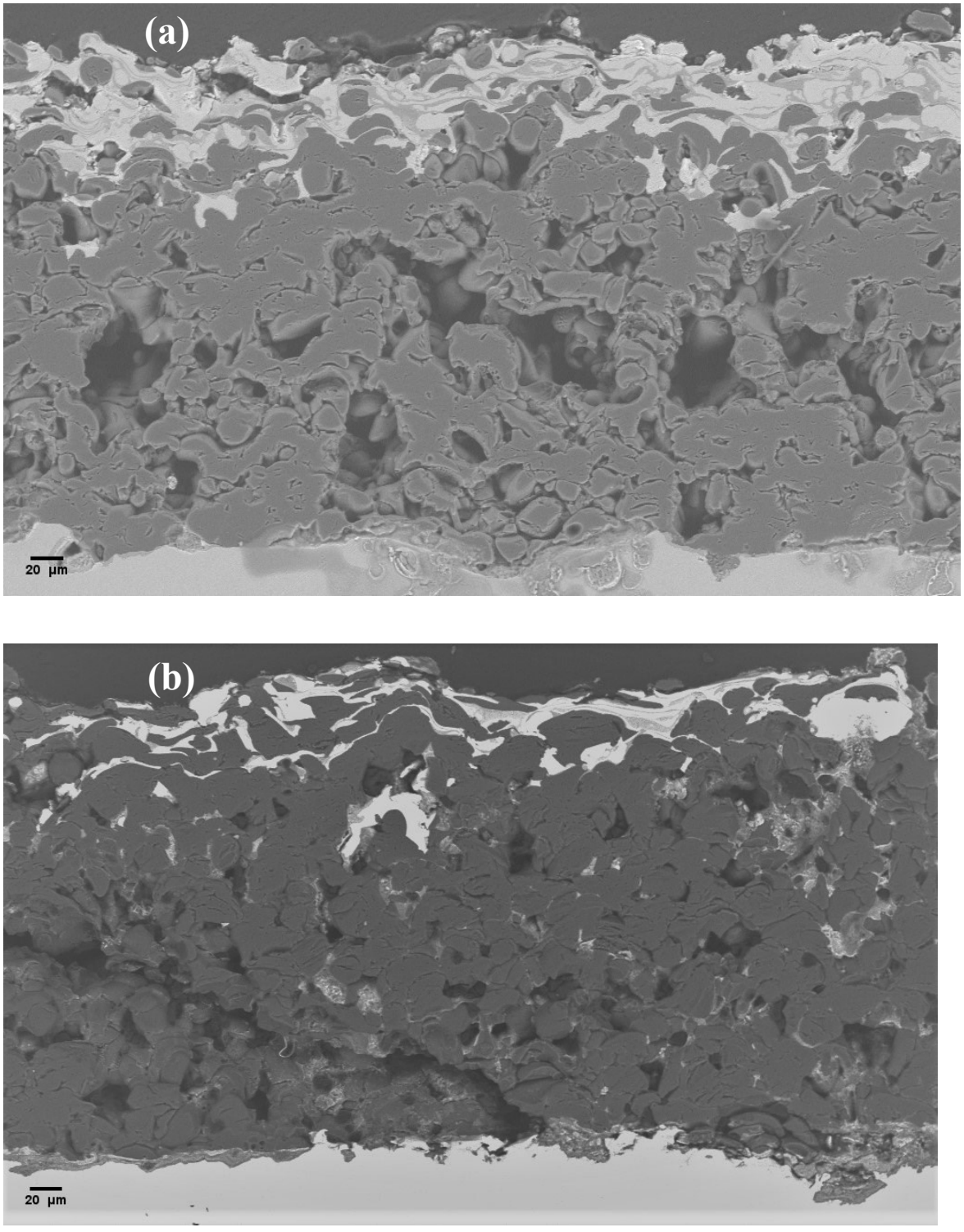

Figure 3.4 Cross-sectional SEM images of the (a) S50 and (b) S65 samples

Since the alumina spraying parameters were the same, the calculated porosity values should be close to each other as they are. The porosity of the resistive heating layer (top layer) was much lower than the alumina layer. The S50 sample's resistive heating layer was 2.14 ± 0.85 vol.% (n = 6), while this value was 3.43 ± 1.19 vol.% (n = 6) for the S65 sample. This was induced by the well coatability of the nichrome particles. As could be seen in Figure 3-4(a) and (b), unlike the alumina layer, it seems that the nichrome particles were melted while being deposited. Hence these particles played the role of filling material. Finally, further image analysis was done to determine the percentage of each powder in the final layer. This analysis was simply done by comparing the surface area occupied by each phase. The nichrome/alumina layer consisted of 40.30 ± 9.14 vol.% (n = 12) and 53.09 ± 6.75 vol.% (n = 11) alumina particles in S50 and S65 samples, respectively.

3.2.2 Joule Heating

3.2.2.1 In Stagnant Air

To demonstrate the heat generation capability of the nichrome coating layers, the S50 sample was tested while exposed to stagnant air. It is worth mentioning that none of the thermocouples could be attached ideally to the desired surface in the Joule heating runs. Therefore, there was always some gap between the thermocouple and the surface. Depending on how big this gap was, the temperature reading error could vary. Figure 3.5 shows the temperature readings of each applied voltage. 2.6 V, 3.5 V, 5 V, and 6 V were the applied voltages in stagnant air experiments. The steady-state temperature of the sample and how long it took the sample to reach this state were among the objectives of these tests.

Figure 3.5 depicts the detailed temperature readings of each experiment. The sudden spike in Figure 3.5 for the "27 W" test shows our attempt to fix the thermocouple gap. As expected, the higher electrical powers led to higher temperature readings. In less than 10 minutes, the sample reached its steady-state regardless of the applied power. Since the feed side's temperature is kept under 100°C, the Joule heating testing with higher voltages was ignored.

The sound functionality of the Joule heating layer is highly dependent on the dielectric layer to work as intended, preventing the electrons moving through the Joule heating layer from reaching the electrically conductive substrate. The obtained results have portrayed that although the alumina layer was porous, the applied voltage was not strong enough to cause electron leakage between the conductive layers. Of course, when saline water is incorporated, water penetrating the open pores could induce short-circuiting.

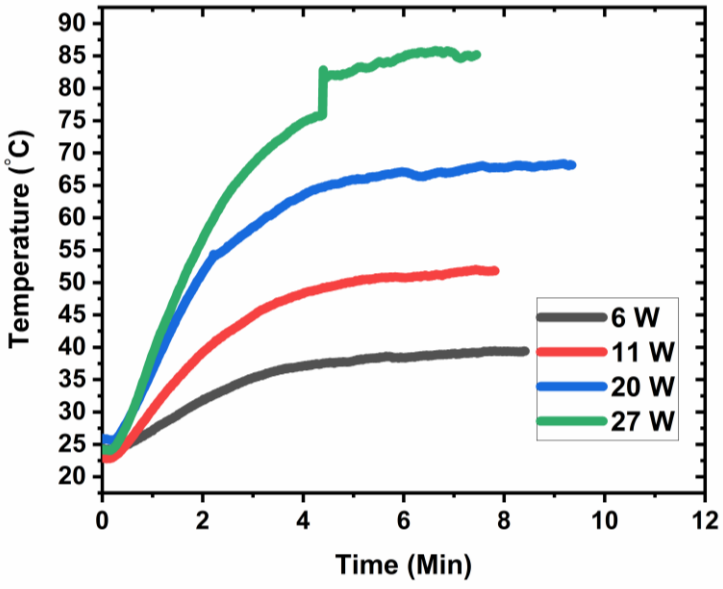

Figure 3.5 Temperature readings of Joule heating experiment in stagnant air

3.2.2.2 In Stagnant Water

In the previous section, the Joule heating performance of the fabricated samples was tested while exposed to stagnant air. Since the air was not our target medium, it was needed to check its performance in the water. This stage was simply done to realize how adding water to the equation would change the samples' performance. Due to some safety concerns, the tests were initiated while the sample was immersed in stagnant water to fully control each component of the circuit. 6 V was chosen for this stage of our study because it was the H-bridge's lowest working voltage. The only parameters that were subject to change were the H-bridge frequency and the concentration of the NaCl in water. Figure 3.6 shows the temperature recording details of the stagnant water experiments.

One of the first questions which might be raised after analyzing Figure 3.6 is the phenomenon that resulted in a higher temperature difference between the temperature of the water and the Joule heating element. The most cautious answer is that the thermocouple placed in water was not fixed. Depending on its location, its temperature reading could have been different. Without any further testing, the above-mentioned speculation is the most reasonable explanation. Since the main purpose of this study was to examine the performance of the Joule heating element while used as the heat source of the MD process, no further studies were done on the stagnant water environment.

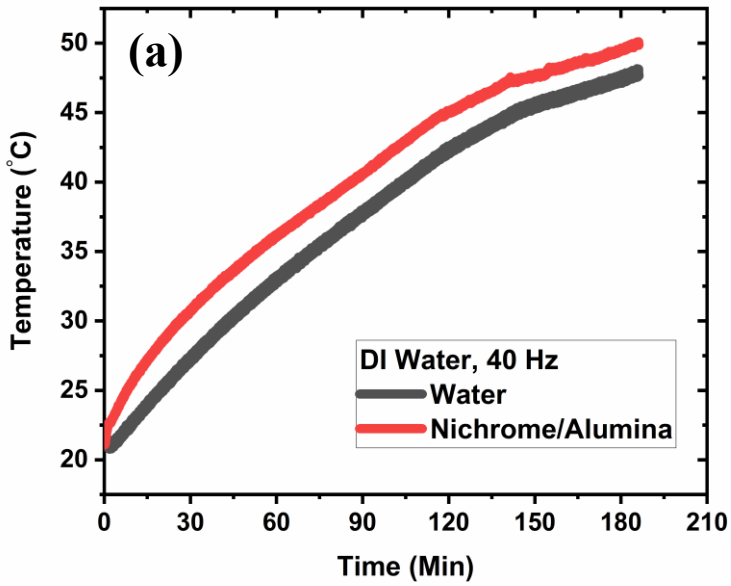
(a)
Temperature (°C)
Time (Min)
DI Water, 40 Hz
Water
Nichrome/Alumina

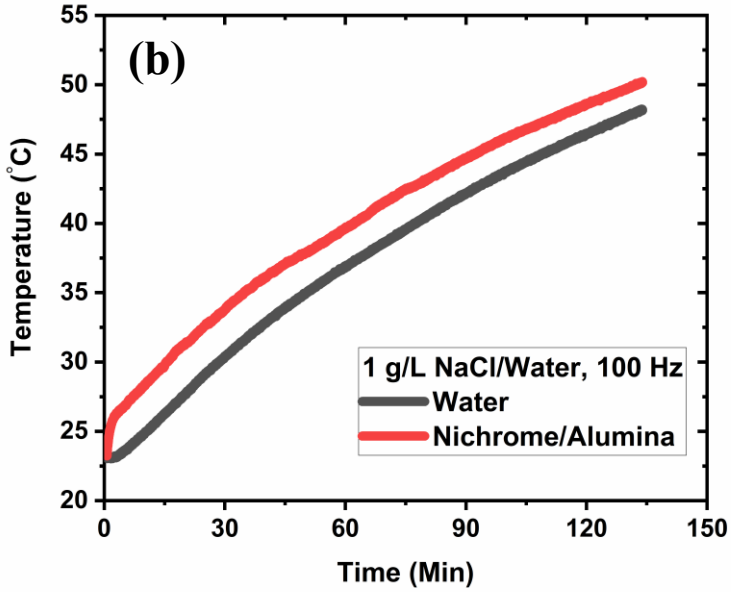
(b)
Temperature (°C)
Time (Min)
1 g/L NaCl/Water, 100 Hz
Water
Nichrome/Alumina

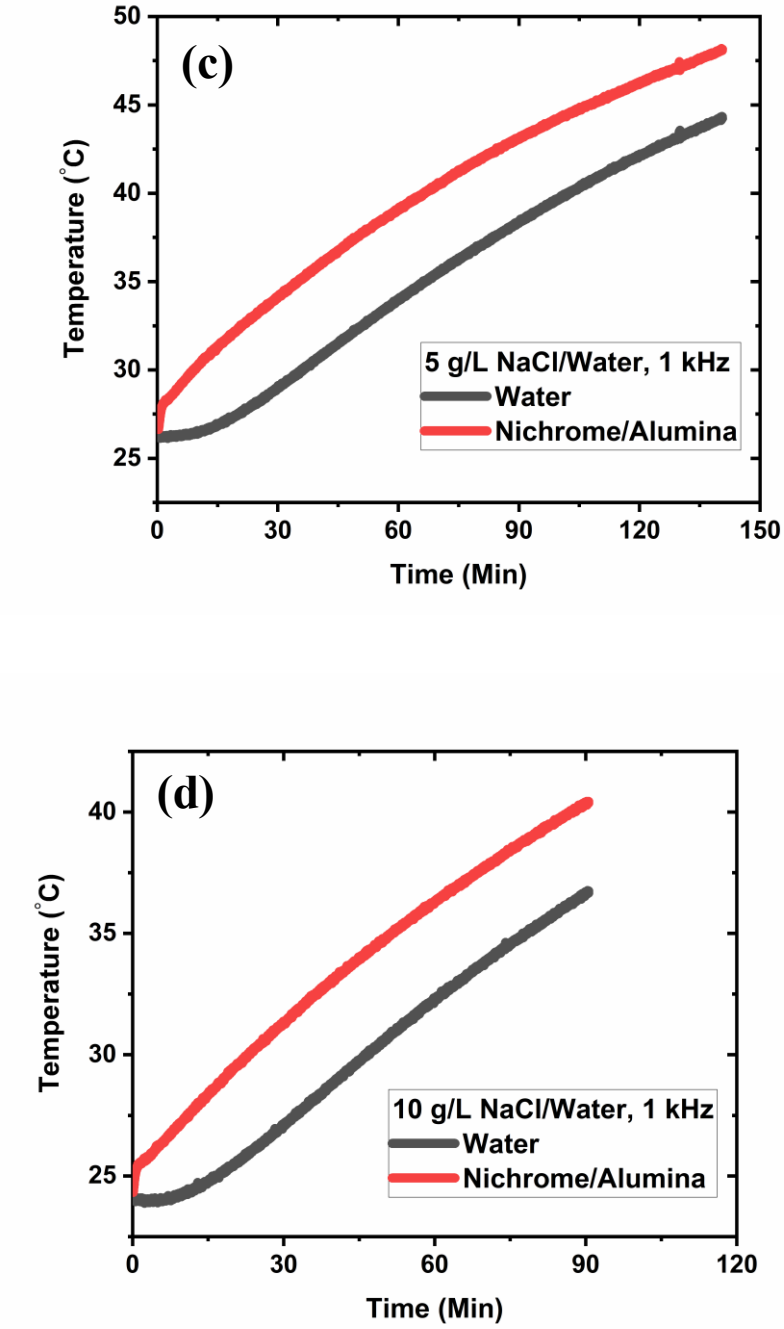

Figure 3.6 Temperature recording of the Joule heating experiments in stagnant water (a) DI water, 40 Hz, (b) 1 g/L NaCl/Water 100 Hz (c) 5 g/L NaCl/Water, 1 kHz, and (d) 10 g/L NaCl/Water, 1 kHz

Moving on to the heating performance of the elements in the stagnant water environment, as expected, the DI water acted as a heat sink, delaying the temperature rise. The fact that the water was heated to reach 50°C in about three hours proved that the designed circuit and the Joule heating sample could serve as heating components of an MD setup. Since DI water had a very low electrical conductivity, the electrical leakage faced in an actual MD test was not present here. Therefore, salt was added to the water at different concentrations to observe its effect on the efficiency of the Joule heating coating layer.

For the second test, NaCl was added to the DI water with 1 g/L concentration. Also, since the added salt could have increased the electron leakage, theoretically, to reduce the chances of electron leakage, the frequency was set at 100 Hz. Interestingly, even though salt was added to the water and it was expected for more electrons to trigger auxiliary electrochemical reactions, the sample reached the 50°C mark one hour sooner than the time it was tested in DI water. The only parameter which was different between the two experiments was the set frequency of the H-bridge. This difference is the testament proving the reasoning behind using an H-bridge for passing electricity through a part that is immersed in water. Regardless of whether there are any contaminants in the water, certain chemical or electrochemical reactions accompany this process. Even when the sample was only exposed to DI water, some orange-looking stains could be found on the nichrome/alumina layer's surface. The same stains could be seen in a much larger quantity on the steel substrate. The quantity of the accumulated oxides on the surface of the sample was much higher when the incorporated medium was saline water.

Additionally, the fact that the temperature readings did not experience any sudden drops during the Joule heating tests confirms that at those temperatures, the

nichrome/alumina layer was highly unlikely to be the source of the oxides found on its surface. The only hypothesis that could be made at this stage regarding the oxides' source was that the steel substrate was being oxidized severely due to testing conditions, and some of those oxides could attach themselves to other surfaces. To make the environment much harsher, the NaCl component concentration was increased to 5 g/L.

The higher thermal efficiency of the sample working with 100 Hz when compared to the test done with 40 Hz led to setting higher frequencies in the next experiments in hopes of optimizing the efficiency furthermore. The Joule heating layer's performance was almost identical to the one recorded in the 1gr/lit NaCl/water environment. The same stable electrical and thermal performance bolstered the hypothesis that the resistive heating layer itself was not subject to corrosion during the experiments. Despite the same pattern of frequency change was followed as before, no significant change in heat generation efficiency was noticed. The reason for this phenomenon is that in order for the designed electrical circuit to work at high frequencies, the components should be compatible with each other. Our findings showed that as the applied frequency was raised, the electrical waves became noisy, and the electrical current shown on the power supply dropped to a lower number, indicating that an ordinary power supply such as ours could not keep up with the H-bridge pace. From this point forward, the working frequency of the H-bridge was set at 1 kHz. The fact that our power supply could not meet the demand made us reluctant to increase the frequency any further to prevent it from getting damaged during the experiments. To test the sample further in saline water, a 10 g/L NaCl/water environment was chosen. Even though this test was not carried out until the temperature of

the nichrome/alumina layer was 50°C, the temperature increase rate was identical to the tests done at 100 Hz and 1 kHz.

The inspection of the sample after the static water tests showed many signs of oxidation. The fact that even the alumina layer was covered with oxides showed that steel was the source of the oxides. Because it was highly unlikely for alumina (a very durable ceramic) to experience any phase changes under those circumstances. Also, the severe color change of the copper tape was a sign of electrical terminals' oxidation. It is worth mentioning that after this series of experiments, the used copper tapes and alligator clips were so oxidized that they could no longer conduct electricity. But, the nichrome/alumina layer kept working with a high level of stability regardless of the voltage, chemical composition of the environment, H-bridge applied frequency, and the nature of the electrical connections. It could be inferred that, at least in the static environment, the nichrome/alumina layer did not engage in auxiliary chemical/electrochemical reactions accompanying the electricity passages through the water.

3.2.2.3 MD test

To make sure that we had the proper setup to test our Joule heating elements, an MD cell was designed. This cell was tested in the conventional MD mode while a commercial PTFE membrane was utilized. Overall the saline feed water was distilled at a 12.1 kg/m^2hr rate. The fact that the conductivity of the permeate tank remained in the initial state shows that the salt rejection of the membrane was 100%. Also, this perfect salt rejection served as a testament proving that the designed MD cell functioned as desired. Having a well

designed and fully functional MD cell, we could examine the performance of the prepared Joule heating elements as the sole heat source of the MD process.

As promising as the results obtained from the static environment tests were, the MD operation is done in a dynamic environment, changing some important factors. In a conventional MD setup, the feed water flows through the cell channels, changing the heat convection from free to forced. Therefore, theoretically, it would be much harder for the sample to maintain its temperature. Also, another change in the MD setup is that much higher quantities of water are involved in the system. Elevating 1 liter of water temperature in a static state to 50°C took almost 2 hours. Considering all the points above, it would be impossible for the Joule heating layer to elevate the bulk water temperature to the desired temperature and trigger the MD process within a few hours. Therefore, the only efficient way for the resistive heating layer to facilitate the MD process is to create the required heat for the distillation at the membrane's surface. It is worth mentioning that based on what has been reported by Rezvani Rad and McDonald [73], the drawn power by the nichrome coating layers could be as high as 500 W. Although the sample itself could work while high power is drawn, it should be noted that the system's temperature should remain below 100°C to ensure that the mass transfer is generated by thermally-induced vapour pressure difference and not flash boiling. Additionally, the occurrence of the flash boiling could damage the pumps due to cavitation. Before analyzing the obtained results, it is necessary to mention that the implemented saline water had 2 grams of NaCl per each liter.

Regarding the concentration of the salt in water, when 5 g/L NaCl/water solution was tested, within a few minutes, the copper tapes were corroded severely, which resulted in a stoppage of electrical connectivity (Figure 3.10(b)). Therefore, 2 g/L NaCl/water solution

was chosen as the testing feed water. In addition to the copper tape, the nichrome/alumina layer could have also been corroded alongside the copper terminals. Interestingly, when the corroded copper tape was replaced with new ones, the electrical conductivity was retrieved. This observation suggested that the nichrome/alumina layer did not engage in any of the auxiliary chemical/electrochemical reactions occurring inside the cell. Even though copper tape proved not to be an ideal option for Joule heating elements in water, since the scope of this study was to investigate the behavior of the resistive heating coating layer, the copper tape remained as the electrical terminal. According to the findings of Dudchenko *et al.* [45], carbon-based materials could be chosen as ideal options for such a purpose. It is worth mentioning that the temporary nature of the copper tape worked in our favor. If the electrical terminals were permanent copper ones, the sample could not be implemented anymore after a few hours. But, when dealing with the copper tape, they were simply replaced after each experiment. This question might be raised that the copper tapes used in the stagnant water experiments did not corrode as fast as the ones incorporated in MD trials. One logical explanation could be that the pressure exerted by the testing setup in the dynamic experiments was much higher. It is widely accepted that stress could accelerate the corrosion process. Therefore, the higher stress inside the MD cell could have contributed to the short electrical lifetime of the copper tapes.

Moving on to the heating performance of the prepared samples, to comprehensively study the Joule heating element being integrated inside the MD cell, various electrical powers (40, 50, 60, 70, and 80 watts) were applied. For each power, four MD runs were done. For the temperature readings, four thermocouples were attached to the feed active area of the MD cell. The temperature recordings of the thermocouple, which was showing

the average temperature of all thermocouples, have been shown in Figure 3.7. As could be seen, the lower electrical powers induce a more smooth temperature rise. This is due to the fact that an H-bridge was utilized. Since the H-bridge switches the direction of the electrical current, at higher powers, the temperature fluctuations are more prominent. In the end, the obtained flux was averaged. Since the temperature recordings of the 80 W experiment were very close to the maximum working temperature of the cell components, we were reluctant to increase the power any further.

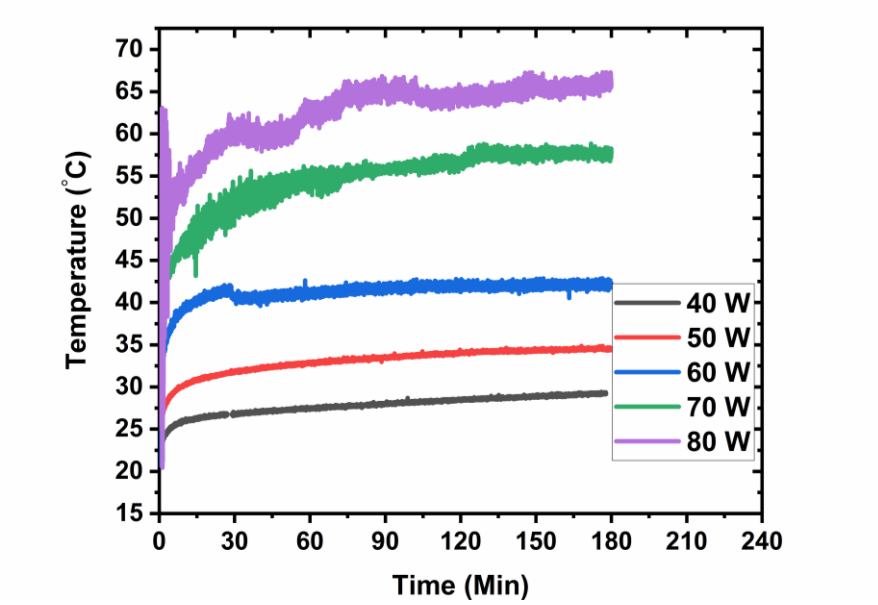

Figure 3.7 Temperature recording of the feed active area during the MD experiments

Although the heat generated by the Joule heating element mostly remained inside the MD cell, over time, the temperature of the feed tank was being affected by the heat source (Figure 3.8). One interesting observation was that when the feed tank temperature raised as the result of the Joule heating element operating, the mass transfer rate increased. The justification for this phenomenon is that the prolonged operation of this novel heat source also triggered the mass transfer due to the bulk feed water becoming slightly hotter than

the permeate water. The feed tank in our experiments was not thermally insulated. Therefore this temperature rise in the feed tank could have been much more significant if the tank was insulated. One can only wonder how different the mass transfer rate could have been if the used system was fully insulated. Since the objective of this study was developing a Joule heating coating layer and a setup to be used in the MD process, our focus was only concentrated on the performance of the Joule heating sample and not the optimizations of the system. It could be claimed that the flux numbers obtained, depicted in Figure 3.9, could be considered as the worst-case scenario numbers for such a system.

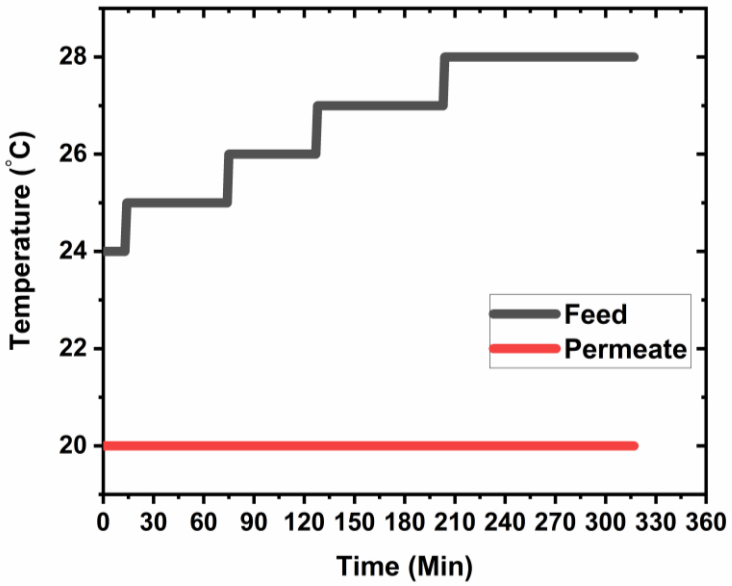

Figure 3.8 Feed water temperature change as a result of coating-based Joule heating

Figure 3.9 shows the direct relationship between the applied power and flux. The flux increased as a direct result of higher powers being used. The numbers reported in Figure 3.9 are the average of all the fluxes which were obtained from four MD runs. Although the reported values of mass flux are not enthralling when compared to the numbers yielded by the conventional MD setups, it is necessary to understand that the power usage in this novel

approach is roughly 3-6 times lower than the commercial heating baths, when the power values of heating baths were checked in catalogs [82]. For instance, the MD cell test done as part of this study yielded 12.1 kg/m^{2}hr as a result of a 40°C temperature difference across the membrane. Also, Noamani [81] has reported more than 30 kg/m^{2}hr mass when the feed water temperature was set at 80°C. Still considering the fact that the Joule heating elements were fabricated utilizing a very inexpensive and industrial method and the cost of the H-bridge, DC power supply, DAQ, the expenses of this novel design is much lower than the conventional one. Without a doubt, the conventional MD is far superior in regards to mass transfer flux, but in case the heat-generating membranes are promoted as the future of the MD process, the resistive heating coating layers fabricated by thermal spraying would be the best option for that design.

Some of the error sources which have shown their effectiveness in the error bars were human error, the error of the equipment, the utilized MD cell, and the nature of the electrical connections. Since human error is quite self-explanatory, we start with the equipment error. The smallest weight that could be detected by the weight scale used in this study was 1 gram. If we consider the fact that the difference between some of the reported fluxes are only a couple of grams of water being distilled in one hour, the very influential role of the weight scale becomes evident. Furthermore, despite getting the work done, the designed MD cell was not a standard one. Therefore from time to time, a small amount of water leaked from the cell. Of course, we tried to overlook the results of those faulty experiments, but one can wonder how big of a role the MD cell has played as a source of error. Finally, the nature of the electrical connections also became problematic in some experiments. Since we could not fabricate our preferred electrical terminals, cold

sprayed copper terminals, we were forced to work with copper tape. Hence the electrical connection between the electrical circuit and the Joule heating element had to be made outside the MD cell. Since the hydrophilic nature of the tape induced some water leakage, the copper tape extended from the water sealed environment of the MD cell to the outside of the cell was problematic. It should be mentioned that we did our best to resolve these problems, but each one could have played a role in causing the errors of these experiments. Besides the role of each error source, it could be said that some components of the Joule heating element did corrode more severely when higher electrical powers were applied. As a result, the induced oxide particles might have blocked the pores of the membrane, reducing the mass transfer rate in some cases. Of course, at this stage, the role of the error sources and the scaling phenomenon on larger error bars could not be determined, and more testing is needed.

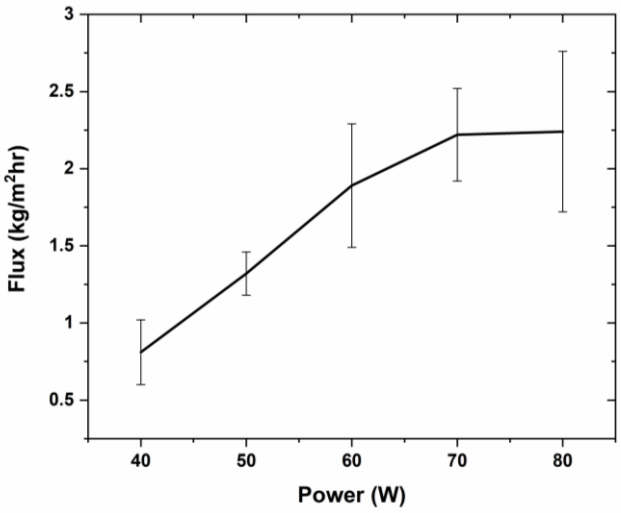

Figure 3.9 Measured fluxes at various electrical powers

When the samples were inspected after the tests, the quantity of oxides found on the surface of the nichrome/alumina layer was significant (Figure 3.10(a)). Since no unstable

electrical or heat generation performance was noticed during the operation of the sample, it was again speculated that the nichrome/alumina layer did not corrode while working. The fact that the alumina layer was also covered in oxides bolstered this hypothesis. Because considering the experiment conditions, it was highly unlikely for a material like alumina to go through any phase changes. To have some assurance about the nichrome/alumina layer not being corroded while generating-heat, the samples were cut down to 1-inch × 1-inch by water jet to be analyzed with SEM.

Figure 3.10 Oxides on the surface of the (a) nichrome/alumina layer and (b) Copper tape

Figure 3.11 portrays the SEM pictures which were taken from the nichrome/alumina layer after implementation inside the MD cell. In Figure 3-11(a) and (b), the height difference between the electrically conductive layer and the oxide layer (having sharp brightness because of charge accumulation) is evident. Figure 3-11(c) image was taken with much higher magnification (500x) of the nichrome/alumina layer. The oxide particle precipitation on top of the nichrome/alumina layer could be seen in Figure 3-11(c). Rather than being corroded, this layer acts as a hub for oxide formation due to the fact that it was conducting electricity.

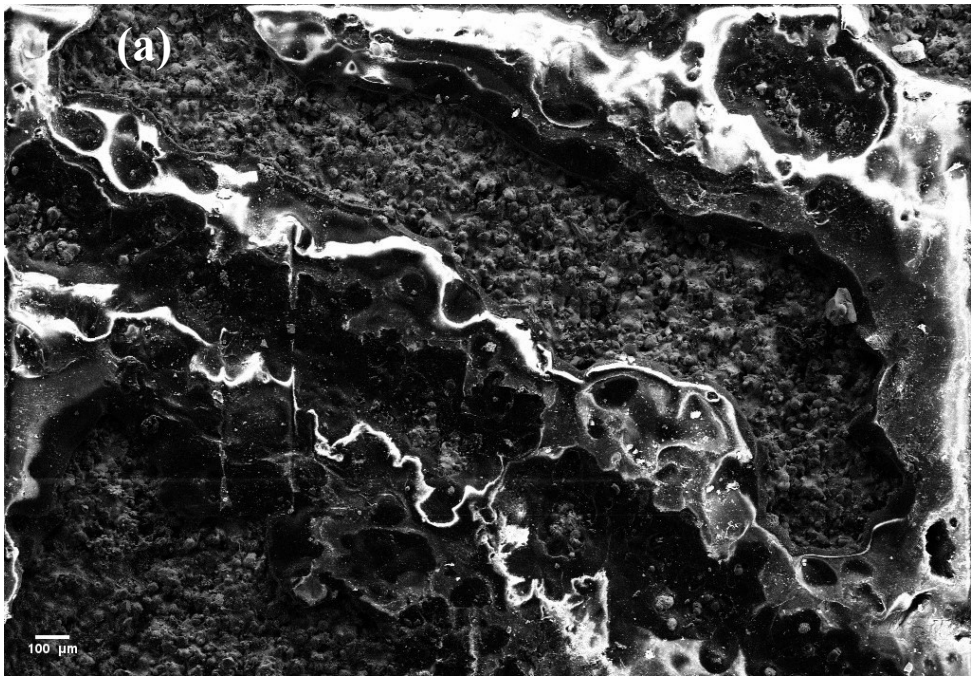
(a)
100 µm

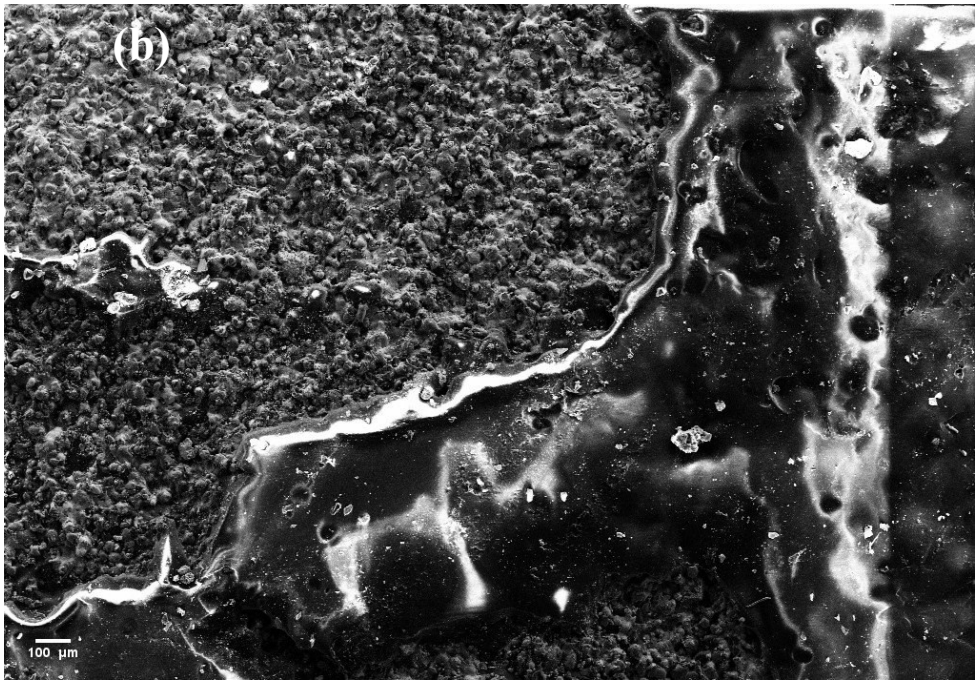
(b)
100 µm

Figure 3.11 Top view images of the nichrome/alumina layer after being used in the MD process (a) 40x, (b) 40x, and (c) 500x

The EDX characterization proved that the oxide layers mostly consisted of elements other than Ni and Cr (Table 3.6). It could be inferred that the nichrome layer did not engage in the deteriorating electrochemical reactions. Therefore, this Joule heating material could have a long-lasting and widespread presence in marine applications. The only downside of the oxide formation precipitation on the surface of the Joule heating layer was that the new copper tapes could not have good contact with the sample, increasing the resistance of the circuit.

Table 3.6 Results of EDX characterization of the Joule heating layer

Wt. %	Ni	Fe	Cr	Cl	Si	Al	Na	O	Mg
Nichrome/alumina	50.2	2.1	15.6	1.6	0.1	7.6	0.6	22.2	-

Oxide	6.4	14.8	1.2	-	3.6	6.2	2.8	64	1

Even though this oxide compound formation did not affect the resistive heating performance of the nichrome material, it still was a concern. The inability of the membrane to retain these compounds on the feed side could have affected the quality of the distilled water. The used PTFE membranes were also characterized by SEM (Figure 3.12). Interestingly as seen from Figure 3.12(a), the membrane's permeate side did not show any anomalies. On the other hand, the feed side of the membrane seemed to be affected by the oxide compounds. The only elements detected by EDX (Table 3.7) on the permeate side were carbon and fluorine, which are the building blocks of PTFE. In contrast, the feed side was contaminated with various elements such as zinc, iron, aluminum (Table 3.7). This assured us that the membrane was not overwhelmed by the formation of oxide on the feed side, and it kept functioning as expected. Since we did not want to leave any doubts about the quality of the filtered water unanswered, four water samples were taken from the bottom of the permeate tank on different days. The water samples were chemically analyzed by the ICP-MS method. The ICP-MS analysis results are brought in Table 3.8.

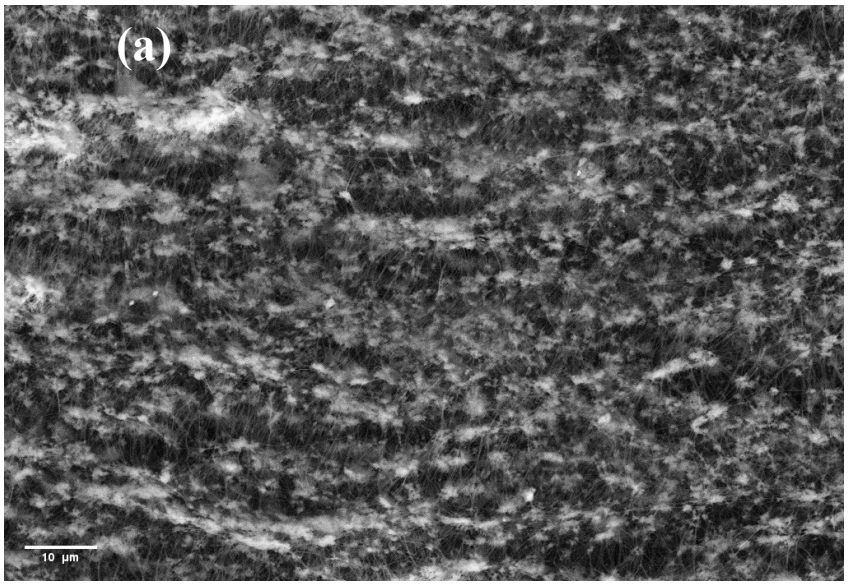
(a)
10 µm

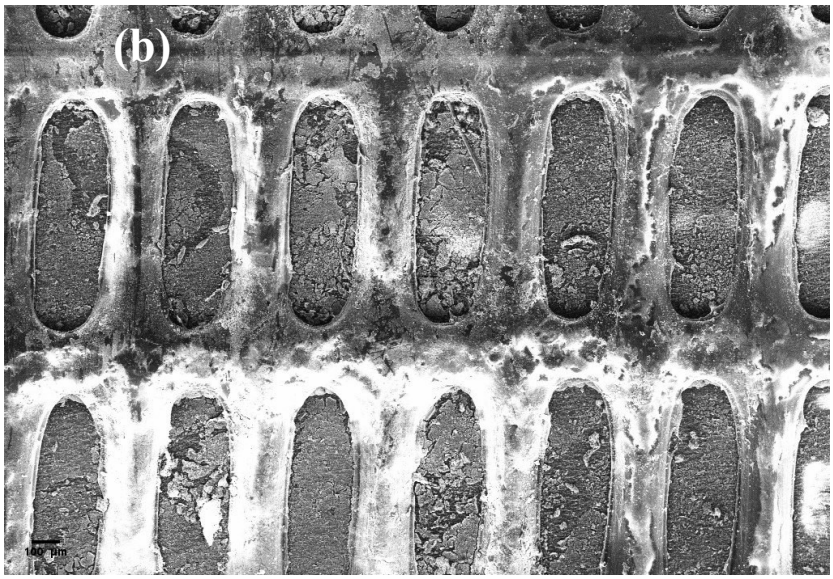
(b)
100 µm

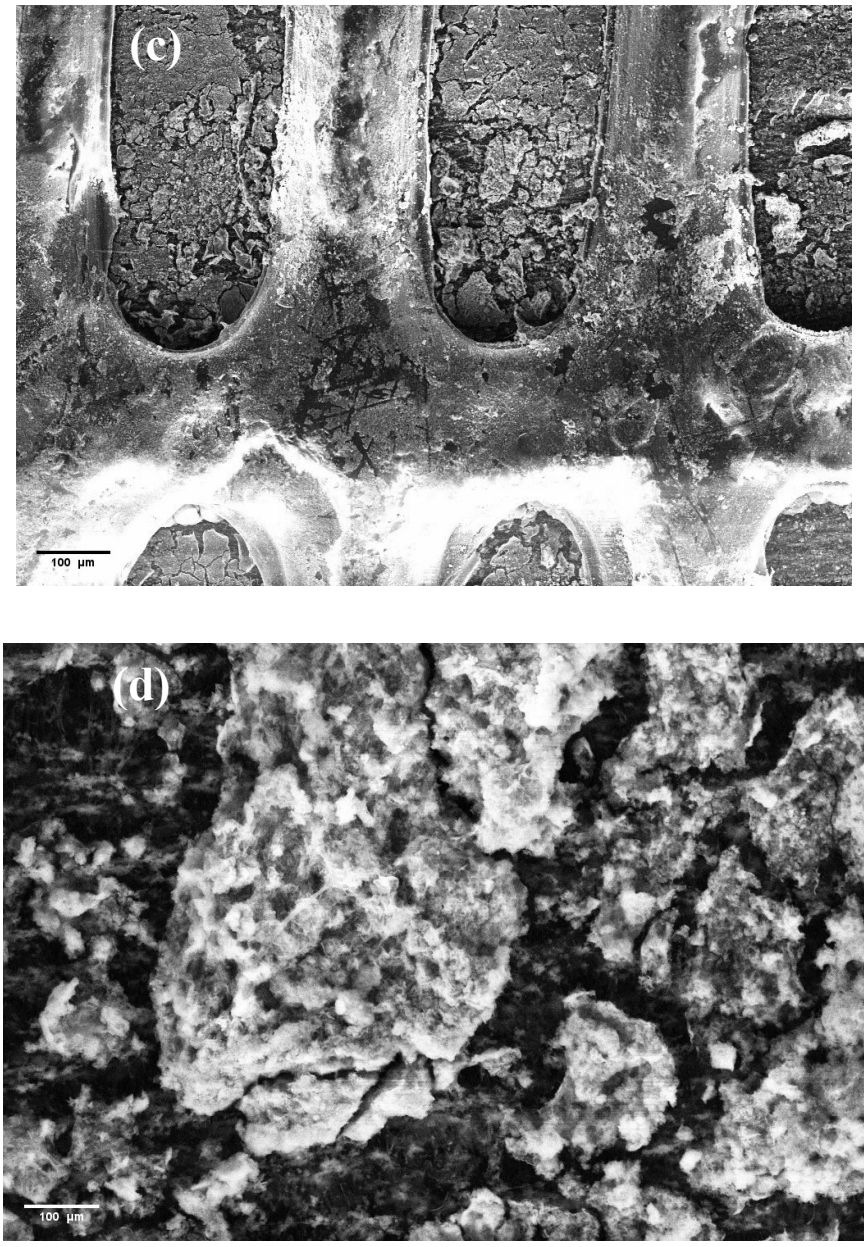

Figure 3.12 Top view SEM imaged of the PTFE membrane after being used in the MD experiments (a) Permeate side 1000x, (b) Feed side 40x, (c) Feed side 100x, and (d) 1000x

Table 3.7 Results of EDX characterization of the PTFE membrane after MD tests

Wt. %	C	F	O	Na	Al	Cl	Fe	Zn
Permeate side	26.6	73.4	-	-	-	-	-	-
Feed side (britght)	33	-	41	8	1.7	1.3	5.2	9.4
Feed side (dark)	14	35	17	6.4	0.7	0.7	5.8	20

Table 3.8 Chemical composition analysis of the permeate water by ICP-MS method

Name	Al (ppb)	Cr (ppb)	Fe (ppb)	Co (ppb)	Ni (ppb)	Cu (ppb)
LOD (ppb)	0.0266	0.0117	1.0627	0.0004	0.0816	0.0040
Sample 1	0.58	0.32	<dl	0.126	8.32	570
Sample 2	<dl	0.07	<dl	0.027	1.52	601
Sample 3	<dl	0.09	<dl	0.030	1.87	594
Sample 4	<dl	0.23	<dl	0.053	3.39	588
Suggested Concentration for Drinking Water	≤ 2900 [83]	≤ 50 [84]	≤ 300 [85]	≤ 1[1] [86]	≤ 69[2] [87]	≤ 2000 [88]

1: The limit has been set for fresh bodies of water
2: In a report published by the world health organization (WHO), this limit has been introduced as the maximum found among drinking waters in Canada

In table 3.8, limits of detection (LOD) refers to the lowest amount that the ICP-MS equipment could have detected. Since our objective was to purify water for regular

households, the amounts detected via ICP-MS characterization were compared with Canadian drinking water regulations. By comparing the data obtained by chemical analysis of our samples and the guidelines of the Canadian government, it could be concluded that not only has the integration of the Joule heating coating layer made it possible to distill water by low energy consumption, but also this additional structure has not deteriorated the quality of the distilled water. There is no doubt that this structure, at least parts of it, was oxidized during the MD operation, but the PTFE membrane layer functioned as a proper barrier, not letting the contaminants to penetrate the permeate water.

3.3 Conclusion

Joule heating coating layers were fabricated by flame spraying on steel substrates. The heat generation of the samples was examined in air and saline water. In the tests which were conducted while the samples were exposed to stagnant air, only 27 W of power was sufficient to increase the temperature of the nichrome/alumina layer to 85°C in less than 10 minutes.

For the testing phase in water, the first stage was done in stagnant water. Also, to prevent the electrons from leaking into the water, a commercial H-bridge was integrated into the electrical circuit. As expected, the water medium acted as a heat sinking agent, which delayed the increase in temperature significantly. Interestingly, in our tests with saline water, although there were higher chances of electrons leaking into the water medium, causing energy waste, by increasing the rate at which the electrical current direction was alternating, the sample reached 50°C much faster. For the samples which were conditioned to 100 Hz and 1 kHz frequencies, regardless of the chemical composition

of water, it took the sample to reach the desired temperature (50°C) one hour less than the sample, which was working with 40 Hz while immersed in DI water. This finding showed that in order to generate heat via resistive heating samples in electrically conductive mediums such as saline water, it is necessary to implement an H-bridge to benefit from the full potential of the heating element.

Moving on to implementing the Joule heating samples in the MD process, as expected, since the cooling nature of the medium was changed from free to forced convection, higher electrical powers were needed to initiate water desalination. Various electrical powers were investigated while the Joule heating element was integrated inside an MD cell. It was evident that the higher the applied power, the higher the temperature of the sample became. The highest average flux recorded belonged to the 80 W power, which yielded 2.24 $kg/hr.m^2$ mass flux. Considering the fact that the temperature of the feed water was not affected significantly by the operation of the Joule heating coating layer suggested the fact that water desalination was done mostly because the generated heat was concentrated at the surface of the membrane. Even though the recorded flux was not as much as the ones reported by the conventional MD process, much less energy was consumed in this novel approach. Furthermore, the heating ability of the Joule heating coating layers remained stable through hours of testing, indicating that this electrically conductive layer did not engage in any auxiliary chemical/electrochemical reactions. The only thing that limited our ability to test our samples in feed waters harsher than 2 gr/lit was the nature of the electrical terminals used in this work. Alongside the steel substrate, the copper tapes implemented for electrical connection did corrode.

This phenomenon could have turned into concern if the quality of the desalinated water was influenced. After testing the chemical composition of the permeate water by the ICP-MS method, it was evident that the concentration of minerals remained within the acceptable range defined by the Canadian government for drinking water. Therefore it could be concluded that not only by implementing Joule heating coating layers, it was possible to distill water with low energy consumption, but also this innovation did not compromise the quality of the purified water. Additionally, unlike the preceding endeavors, this novelty could be executed via the flame spray coating process, which is fairly inexpensive and widely used in the industry. The authors of this document believe that it is too early to conduct a detailed performance analysis of this novel design. The reason is that the purpose of this study was to develop an inexpensively made Joule heating element to be used in water desalination. Our focus was concentrated on developing a system to make it possible to benefit from such coating layers. None of the other components of the MD setup was modified according to this innovative approach. We believe that there are many aspects of this process that could be optimized, making the Joule heating elements more efficient and more viable options for water desalination.

Chapter 4

4. Mathematical Modelling of Performance of the Joule Heating Coating Layer Integrated into the MD Process

In this chapter, a collaborative effort was made to model the heat and mass transfer of the MD process in which the Joule heating element has been integrated. It must be mentioned that the following mathematical model has already been developed by Ms. Sadaf Noamani in the advance water research lab (AWRL). The author of this document used the results of the model and the obtained experimental values to further analyze the performance of the Joule heating elements being integrated into the MD cell. Since the heat and mass transfer occurring inside the MD cell are coupled together, both phenomena have been investigated. The developed model benefits from simplicity, but when its predictions were compared to the experimental results obtained in the previous chapter, it became evident that this simplicity did not affect the accuracy of the model in a significant way. It is worth mentioning that since the integration of the Joule heating materials in the membrane desalination processes has not been explored deeply in the research community, the introduced mathematical model has no precedents.

4.1 Mass Transfer

The MD process's driving force is the temperature difference between the two water bodies separated by the membrane. This temperature difference induces a vapor pressure difference across the membrane. For example, for a temperature difference of 40°C across a membrane in contact with a feed water containing 2 g/L salt, the vapor pressure difference

is 17475 kg/m^{2}sPa. As a direct result, the feed water, which is in contact with the membrane surface, vaporizes, and after moving through the membrane pores, it condensates on the permeate side of the membrane. Therefore, the vapor pressure of the feed and permeate water dictates the mass flux (J).

$$J_w = B_M(P_{wvf} - P_{wvp}) \tag{4.1}$$

In Eq.(4.1), the J_w, B_M, P_{wvf}, and P_{wvp} correspond to the mass flux (kg/m^{2}s), the membrane mass transfer coefficient (kg/m^{2}sPa), and vapor pressures of feed and permeate water in the vicinity of the membrane (Pa) [89 – 93].

Each of the parameters involved in the Eq.(4.1) could be determined by mathematical equations. For starters, the membrane mass transfer coefficient denoted by B_M is a function of the membrane features such as its porosity (ε), pore size (r), tortuosity ($\tau = 1/\varepsilon$) [94], thickness (δ), the mass transfer type through the membrane pores and the average temperature across the membrane (Eq.(4.2)).

$$T_m = \frac{T_{mf} + T_{mp}}{2} \tag{4.2}$$

The letter T represents the temperature, and the subscript m, f, and p each represent the membrane, feed, and permeate. For instance, the subscript mf refers to the feed side surface of the membrane.

The characteristics of the flow which occurs via the structure of the membrane could be determined after the dimensionless Knudsen number (Eq.(4.3)) is calculated [5, 15, 95]. If the Knudsen number is larger than 1, the flow is categorized as the Knudsen flow in which the collision of the water vapor molecules to each other transpires with lower frequency when compared to the collision of these molecules with the pore wall [5, 15,

95]. In case this number is smaller than 0.01, the flow type is characterized as molecular diffusion, in which, unlike the Knudsen flow, the chances of the vapor molecules hitting each other is higher than the wall collision [5, 15, 95]. Lastly, if the Knudsen number lies between 0.01 and 1, the flow of the molecules through the membrane pores is a combination of both the diffusion modes [5, 15, 95].

$$K_n = \frac{\lambda}{d_{pore}} \tag{4.3}$$

$$\lambda = \frac{K_B T_m}{\sqrt{2}\Pi P_m \sigma^2} \tag{4.4}$$

In the above equations λ, d_{pore}, K_{B}, P_{m}, and σ represent the mean free path of transported molecules, the diameter of membrane's pores, the Boltzman constant, the mean pressure inside the pores, and the collision diameter of water molecules, in that order [15]. The mean pressure inside the pores has been assumed to be atmospheric pressure while the collision diameter was set at 2.641×10^{-10} m [81]. After the Knudsen number is calculated according to Eq.(4.3), depending on how the mass transfer mode could be characterized based on its value, one of the equations mentioned below could be used to determine the membrane mass transfer coefficient [43, 95, 96].

$$Knudsen\ Flow:\ B_{\text{M}} = B_{\text{K}} = \left(\frac{2\varepsilon r}{3\delta\tau}\right)\left(\frac{8MW_{\text{w}}}{\pi RT_{\text{m}}}\right)^{0.5} \tag{4.5}$$

$$Molecular\ Diffusion:\ B_{\text{M}} = B_{\text{m}} = \left(\frac{MW_{\text{w}}\varepsilon PD}{RT_{\text{m}}\delta\tau P_{\text{air,pore}}}\right) \tag{4.6}$$

$$Combination:\ B_{\text{M}} = B_{\text{T}} = \left\{\left[\left(\frac{2\varepsilon r}{3\delta\tau}\right)\left(\frac{8MW_{\text{w}}}{\pi RT_{\text{m}}}\right)^{0.5}\right]^{-1} + \left[\frac{MW_{\text{w}}\varepsilon PD}{RT_{\text{m}}\delta\tau P_{\text{air,pore}}}\right]^{-1}\right\}^{-1} \tag{4.7}$$

The molecular weight of water (MW_{w}), the universal gas constant (R), the air pressure in the membrane pores ($P_{\text{air, pore}}$), the total pressure inside the pores (P), and the diffusion

coefficient of water (D) are some of the parameters which are involved in the above equations. The PD and $P_{air,\ pore}$ values could be defined implementing the below mathematical relations [95]:

$$PD = 1.895 \times 10^{-5} {T_m}^{2.072} \tag{4.8}$$

$$P_{air,pore} = P_m - \exp(23.1964 - \left(\frac{3816.44}{T_m - 46.13}\right)) \tag{4.9}$$

With the B_M related equations being determined, the vapor pressure of the feed and permeate sides are the two missing parts to calculate the mass transfer flux via Eq.(4.1). According to Eq.(4.10), the feed side vapor pressure could be calculated if the activity coefficient of water (γ_{wf}), the mole fraction of water (x_{wf}), and the surface temperature of the membrane on that particular side (T_{mf}) are available [43, 92, 94, 97]. Since the permeate water is supposed to have no contaminants (perfect rejection of the membrane in the MD process), the only required piece of data for the permeate side vapor pressure is the temperature of the membrane on this side (Eq.(4.11)) [43, 92, 94, 97].

$$P_{wvf} = (\gamma_{wf} x_{wf}) \exp(23.1964 - \frac{3816.44}{T_{mf} - 46.13})) \tag{4.10}$$

$$P_{wvp} = \exp(23.1964 - (\frac{3816.44}{T_{mp} - 46.13})) \tag{4.11}$$

The activity coefficient could be calculated using Eq.(4.12) implemented in other studies [94,97].

$$\gamma_{wf} = 1 - (0.5 x_{NaCl}) - (10 (x_{NaCl})^2) \tag{4.12}$$

4.2 Heat Transfer

It is evident that in order to solve the equations defined for the mass transfer, which occurs through the membrane, the surface temperature of the membrane on both the feed and permeate sides is needed. Therefore, the heat transfer governed by the temperature difference inside the cell should be defined and solved. The introduction of the Joule heating layer into the MD cell changes the direction of some of the heat transfer phenomena. In a conventional MD setup, all modes of heat transfer occur from the feed side to the permeate side. Meaning that the heat is transferred from the feed bulk water to the membrane, the membrane conducts the heat from its feed to the permeate surface, and on the feed side, the heat follows the same direction in which it gets transferred from the membrane to the bulk permeate water. Unlike the conventional MD, when the heat source is placed close to the membrane, the feed water no longer is the body with the highest temperature. The surface of the membrane on the feed side becomes the body that has the highest temperature. This fact helps us determine the direction of the heat transfer in this novel system. Of course, since our Joule heating material is not embedded inside the structure of the membrane, in reality, the membrane surface is not the hottest body in this system. But, for the sake of simplicity, we only introduced the effect of the Joule heating element, which is its electrical power, into the equation. Its physical attributes and the gap between this element and the membrane surface were not parts of this mathematical modeling. As a result, the surface of the membrane on the feed side becomes the hottest body. Therefore, there would be a forced convective heat transfer from this surface to the bulk of the feed water. The second mode of heat transfer is conduction, in which the membrane is the medium. The direction is from the feed to the permeate. Another heat

transfer occurs because the membrane triggers mass transfer. The vaporization and the movement of the water molecules through the membrane pores governs this heat transfer mode. Lastly, the membrane permeate surface would have a higher temperature than the permeate water because of the conducted heat through the membrane and also the exothermic nature of condensation. The below equations portray the mathematical relations governing each of the heat transfer modes mentioned above [92, 94]. The assumption made regarding the membrane surface being the hottest body in this system has been implemented in Eq.(4.13), which shows that heat was transferred from the membrane surface to the feed water bulk body. $Q_{M,}$ which represents the overall heat transfer occurring via the membrane, could be calculated when the heat conducted via the membrane (Q_{cm}) structure and the heat transfer caused by mass transfer (Q_v) are determined.

$$Q_{\mathrm{f}} = h_{\mathrm{f}}(T_{\mathrm{mf}} - T_{\mathrm{bf}}) \tag{4.13}$$

$$Q_{\mathrm{M}} = Q_{\mathrm{cm}} + Q_{\mathrm{v}} \tag{4.14}$$

$$Q_{\mathrm{cm}} = \frac{K_{\mathrm{M}}}{\delta}(T_{\mathrm{mf}} - T_{\mathrm{mp}}) \tag{4.15}$$

$$Q_{\mathrm{cm}} = \frac{K_{\mathrm{M}}}{\delta}(T_{\mathrm{mf}} - T_{\mathrm{mp}}) \tag{4.16}$$

$$Q_{\mathrm{v}} = J_{\mathrm{w}}(\Delta H_{\mathrm{v}}) \tag{4.17}$$

$$\Delta H_{\mathrm{v}} = 1.7535T_{\mathrm{mf}} - 2024.3 \tag{4.18}$$

$$Q_{\mathrm{p}} = h_{\mathrm{p}}(T_{\mathrm{mp}} - T_{\mathrm{bp}}) \tag{4.19}$$

In the equations presented above, the K_M corresponds to the total effective membrane thermal conductivity, which could be accurately calculated by the below mathematical relations [80, 92].

$$k_{\mathrm{m}} = \alpha_1 \times 10^{-4} T_m + \alpha_2 \times 10^{-2} \quad (4.20)$$

$$k_{\mathrm{gas}} = 2.72 \times 10^{-3} + 7.75 \times 10^{-5} T_m \quad (4.21)$$

$$\beta = (k_{\mathrm{m}} - k_{\mathrm{gas}})/(k_{\mathrm{m}} + 2k_{\mathrm{gas}}) \quad (4.22)$$

$$\beta = (k_{\mathrm{m}} - k_{\mathrm{gas}})/(k_{\mathrm{m}} + 2k_{\mathrm{gas}}) \quad (4.23)$$

$$K_{\mathrm{M}} = \frac{k_{\mathrm{gas}}(1 + 2\beta(1-\varepsilon))}{(1 - \beta(1-\varepsilon))} \quad (4.24)$$

In Eq.(4.20), α_1 and α_2 are constants that correspond to 5.77 and 8.914 for PTFE, respectively [96].

Since our study targets the steady-state condition, according to energy conservation law, the amount of energy stored in the selected control volume did not change. Therefore, the heat generated at the surface of the membrane was transferred to the feed water and the membrane structure. This law also suggested that the heat conducted through the membrane equalized the heat transferred to the permeate water. Hence, the energy balance equation (EQ.(4.25)) could be written. As a result, if the energy balance equations (mentioned below) are solved for the temperature of the membrane on the feed (T_{mf}) and permeate (T_{mp}), the surface temperatures could be calculated.

$$\mathrm{Q} = \mathrm{Q_f} = \mathrm{Q_{gen}} = \mathrm{Q_p} = \mathrm{U}\ (\mathrm{T_{mf}} - \mathrm{T_{bp}}) \quad (4.25)$$

$$U = \frac{1}{\left[\frac{1}{\left[\frac{K_M}{\delta}\right] + \left[\frac{J_w\,(\Delta H_V)}{T_{mf} - T_{mp}}\right]}\right] + \left[\frac{1}{h_p}\right]} \quad (4.26)$$

$$Q = \frac{(T_{mf} - T_{bf})}{\frac{1}{h_f}} = Q_{gen} = \frac{T_{mf} - T_{mp}}{\frac{1}{\left[\frac{K_M}{\delta}\right] + \left[\frac{J_w\,(\Delta H_V)}{T_{mf} - T_{mp}}\right]}} = \frac{(T_{mp} - T_{bp})}{\frac{1}{h_p}} \quad (4.27)$$

$$T_{mf} = \frac{(Q_{gen} + h_f(T_{bf}) + U(T_{bp})}{h_f + U} \tag{4.28}$$

$$T_{mp} = \frac{\left(Q_{gen} - h_f(T_{mf} - T_{bf}) \right)}{h_p} + T_{bp} \tag{4.29}$$

The heat transfer coefficient of the feed and permeate water could be computed if the Nusselt number, the thermal conductivity of the respective solution, and the hydraulic diameter of the flow channel are available [35, 92, 97].

$$h_{\mathrm{f}} = \frac{\mathrm{Nu_f} k_{\mathrm{f}}}{D_{\mathrm{h}}} \tag{4.30}$$

$$h_{\mathrm{p}} = \frac{\mathrm{Nu_p} k_{\mathrm{p}}}{D_{\mathrm{h}}} \tag{4.31}$$

As warned by Hitsov *et al.* [80], the equations defining the mathematical relations of the Nusselt number should be chosen cautiously, as in some cases, there are some differences between the predicted values and the real values in practice. Since the model developed by Noamani [81] did agree with the results obtained from the practice, and because of the similar nature of this work with hers, the Nusselt number equations used in that work were selected for this study.

There are two natural consequences of the membrane being the medium that triggers phase change, known as “temperature polarization” and “concentration polarization.” The former is the direct result of the endothermic and exothermic nature of the vaporization and condensation processes. Therefore, the temperature of the membrane surface in contact with the feed water will be lower than the bulk feed water. On the other hand, the temperature of the membrane on the permeate side will be higher than the actual temperature of the permeate water. Hence the temperature difference, which causes the

driving force to reduce. The latter phenomenon, called concentration polarization, occurs because of the retention of the contaminants by the membrane. As a result, the water which is in the vicinity of the membrane would contain a higher concentration of contaminants, ergo lower vapor pressure. The intensity of these two phenomena has been formulated and could be calculated via Eq.(4.32) and Eq.(4.34) [31, 95 – 97].

$$\mathrm{TPC} = \frac{T_{\mathrm{mf}} - T_{\mathrm{mp}}}{T_{\mathrm{bf}} - T_{\mathrm{bp}}} \tag{4.32}$$

$$C_{\mathrm{mf}} = C_{\mathrm{bf}}\, e^{\left(\frac{J_{\mathrm{w}}}{\rho_{\mathrm{f}} K}\right)} \tag{4.33}$$

$$\mathrm{CPC} = \frac{C_{\mathrm{mf}}}{C_{\mathrm{bf}}} \tag{4.34}$$

In contrast with the *CPC*, the smaller values of *TPC* indicate a more potent polarization effect [81, 98].

The performance of an MD design is evaluated by two parameters known as thermal (η) and energy (*GOR*) efficiencies [15, 32]. While the former could be calculated using Eq.(4.35), Eq.(4.36) has been suggested for the determination of the latter [15, 32].

$$\eta = \frac{Q_{\mathrm{v}}}{Q_{\mathrm{v}} + Q_{\mathrm{cm}}} \times 100 \tag{4.35}$$

$$\mathrm{GOR} = \frac{Q_{\mathrm{v}}}{Q_{\mathrm{H}}} \tag{4.36}$$

4.3 Algorithm

For the development and execution of the following algorithm, a MATLAB program was written. In the first step of this model, the membrane properties (porosity, tortuosity, thickness, pore size, active surface area, thermal conductivity), fluid properties (salt

concentration, viscosity, thermal conductivity, and solution density), module geometry, operating conditions, and the power of the Joule heating element were defined as inputs.

In the next step, one surface temperature for each side of the membrane was guessed. In an iterative manner, the average temperature across the membrane, the mass transfer mode, and the resulting flux were calculated. Using the calculated flux, the heat transferred because of the vapor movement is computed. Using the Eqs. which has been defined for the overall heat transfer coefficient, the value yielded by this equation helps us define the new feed and permeate temperatures of the membrane. This iteration was carried on until the error margin between the new temperatures and the old ones became smaller than 10^{-8}.

When the final temperatures were calculated from the heat and mass balance equations, the values of each heat transfer mode, the TPC, the CPC, the thermal efficiency, and the GOR could be determined using the equations defined in this manuscript.

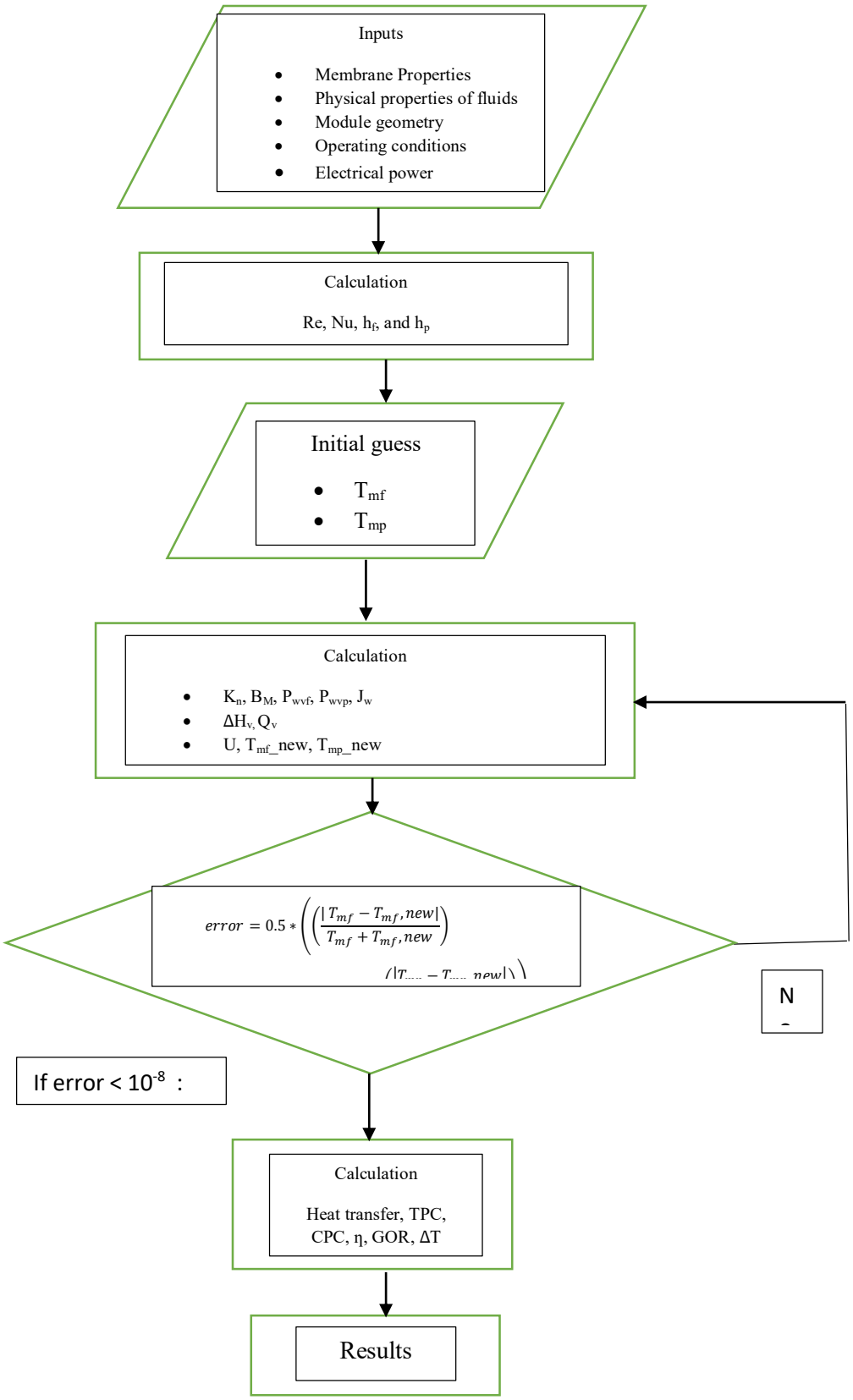

Figure 4.1 Flow chart of the developed model algorithm

4.4 Results and discussion

The comparison of the experimental results regarding the mass transfer flux with the values predicted by the mathematical model yielded Figure 4.1.

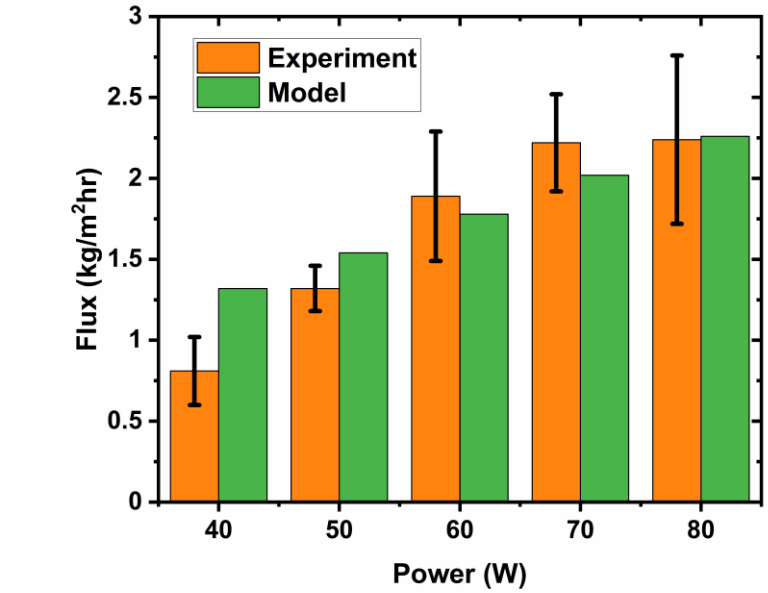

Figure 4.2 Comparison of the measured fluxes from both experimental and theoretical ways as a function of electrical power

As could be seen, the deviation of the two values is much higher at low powers than high powers. It seems that the higher the electrical power, the agreement between the simulation and the experimental data grows. Based on the conducted experiments, it was obvious that the 40 W power was not potent enough to trigger water desalination. Our experimental results were much lower than the flux predicted by the model. One possible explanation could be the exclusion of the time factor in the mathematical model. In most experiments, it could be seen that it took the samples some time to start triggering the distillation process. The lower the power, this time became longer. It might be possible that

if the 40 W experiment is conducted for a long time, the obtained flux would agree more with the predicted value. If the value calculated for the 40 W power is excluded, it could be concluded that the model had under 20 % error when simulating the conditions. It shows that the simple construction of the model did not make it ineffective to model the heat and mass transfer phenomena occurring inside the MD cell.

Secondly, the results of the mathematical modeling showed that the reason behind the low rates of mass transfer was the minimal temperature difference across the membrane (Figure 4.2). Even though the heat source was placed close to the membrane, its power was not high enough to impact the temperature of the water. If we reflect on the fluid flow, this becomes quite reasonable. A small sample generating heat is exposed to a bulk of water circulating through the system at a certain rate. Since the temperature readings showed much higher temperatures than the ones that the model suggests, it could be inferred that the Joule heating sample does not have enough time to affect the temperature of the water significantly. Just in a few seconds of exposure, the feed water absorbs a certain amount of heat, and it dumps the heat inside a tank containing 6 liters of cold water, which is not thermally insulated. It seems that rather than the Joule heating element, the design of the current setup is inefficient. Therefore, an optimized system might yield much more promising results that could make the Joule heating coating layers the innovation that the MD process needs to become a commercially viable water desalination method.

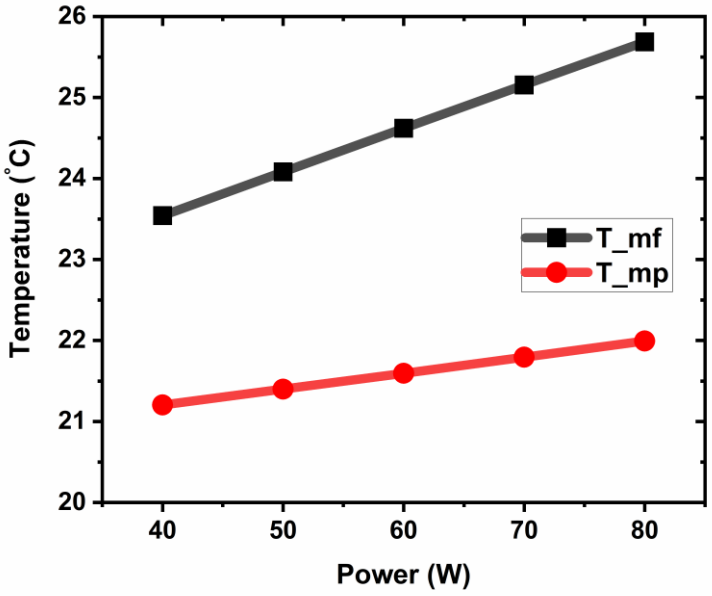

Figure 4.3 Calculated temperature of the membrane on both feed and permeate sides

The calculations regarding the thermal efficiency and the GOR of the Joule heating element integrated into the MD process yielded Figure 4.3. Even though the sample's thermal efficiency increased with higher electrical powers, the GOR followed the opposite trend. Of course, these changes were not that significant. Although the improvement in thermal efficiency was expected, the lower GOR efficiency of high powers was not expected. This result indicates that the generated heat is being wasted because of the design.

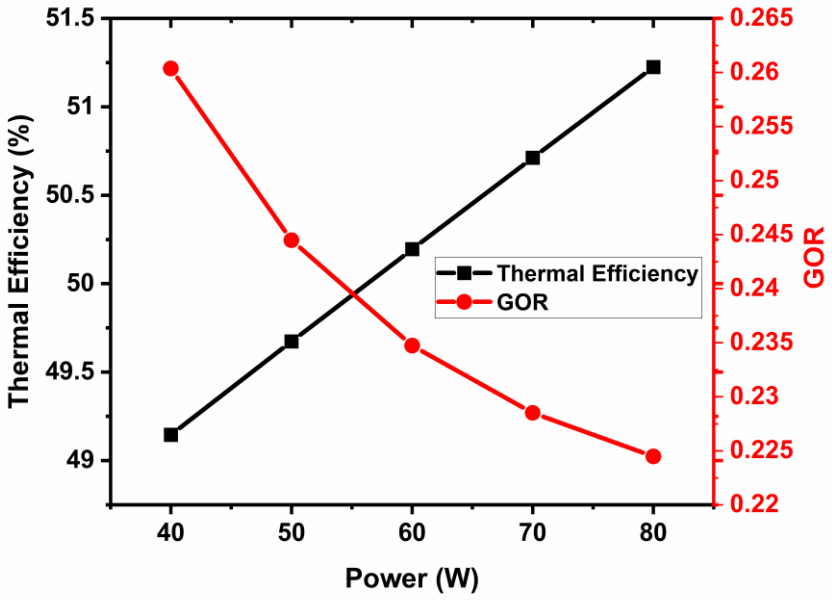

Figure 4.4 Thermal efficiency and GOR as functions of electrical power

Figure 4.4 shows the values related to TPC and CPC factors. Regarding the temperature polarization effect, the temperature polarization became a bit stronger with higher powers used, but this difference did not play a big role in the mass transfer. Having compared the TPC values of this system with the ones reported by Noamani [81], it could be seen that for a membrane with the same thickness as the one used in this study (100 μm), the temperature polarization is 2-3 times more effective in the conventional setup. The reason for this difference is the fact that the heat source is close to the membrane surface. This way, the surface of the membrane possesses a higher temperature than the feed bulk water. This explains why temperature polarization is much less problematic in this design.

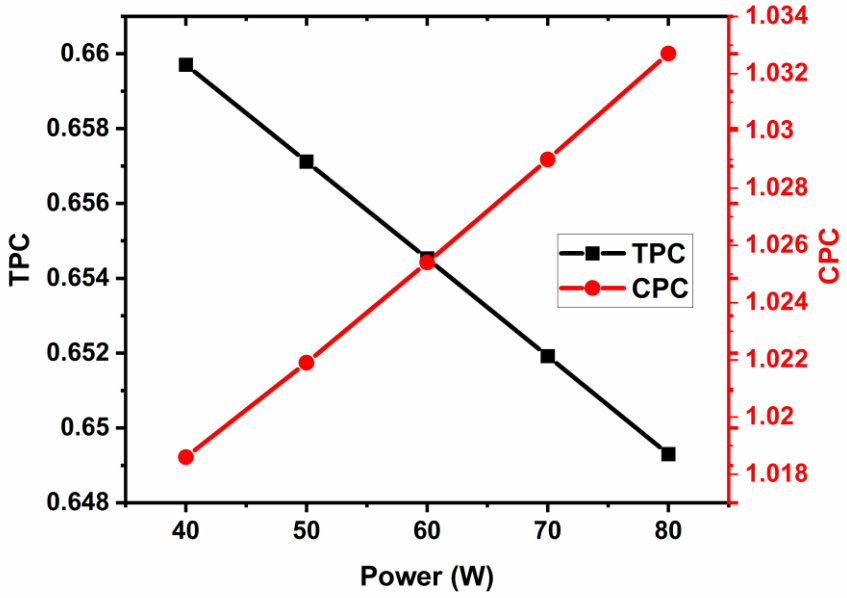

Figure 4.5 TPC and CPC values as a function of electrical power

Moving on to the CPC values, since in our experiments, we only could add 2 grams of salt per liter of water, this value is much lower than the ones reported by Noamani [81]. As expected, the higher the flux, the more adverse the concentration polarization effect becomes. Therefore, the CPC value increased as a result of the electrical power raise.

4.5 Conclusion

In this work, a simple Nusselt number based mathematical model was developed to evaluate the difference made by the addition of the Joule heating element to the MD process. Even though the developed model was simple, in most cases, it had the capability to predict the mass flux with a high level of accuracy. The error margin of the predictions of this model with the experimental data was under 20 % in the majority of cases. The temperatures which were calculated for the feed and permeate sides of the membrane were

26°C, which showed the inability of the Joule heating element to be significantly effective in the current design. In addition to providing us with insight regarding the mass flux, the effects of temperature and concentration polarization were also evaluated in this simulation. The concentration polarization effect was not that significant due to only 2 grams of salt being dissolved in each liter of water. The TPC number was 0.65, which was 2-3 times the numbers reported in the literature involving conventional MD setups. The fact that the proximity of heat source to the membrane reduces the effect of temperature polarization is one of the strengths of this novel approach. The thermal efficiency of the system was around 50 %. It was obvious that as the heat generation power increased, the growth in flux induced some improvement in thermal efficiency.

Chapter 5

5. Conclusion

5.1 Overall Conclusions

Despite having many advantages, the MD process's high energy demand and its low flux are among the biggest disadvantages of this method, hindering it from becoming a commercially viable water desalination process. One of the possible solutions to these issues proposed in the literature has been the fabrication of heat-generating membranes. Even though promising results have been reported by scholars in this regard, the high cost of the heat-generating materials was a challenge that was not overcome in past efforts. Therefore, the main objective of this work was to fabricate such membranes by implementing the inexpensive and industrially used method of flame spray coating.

The original plan to achieve the abovementioned goal was to use a porous support material such as steel mesh and deposit dielectric and Joule heating layers, consequentially on its feed side. On the permeate side, to complete the structure of the membrane, polymer casting was done. Although the porous nature of the base material posed many challenges in both the flame spraying and polymer casting processes, by modifying some of the involved parameters, those challenges were overcome. But our attempt to generate heat in the mesh-based membranes was fruitless mostly.

Therefore an alternative approach was taken. Instead of the steel mesh, the base layer became a steel plate. Since the substrate had a bulk structure, prior to being coated, a few holes were drilled in its structure. Changing the substrate, the flame spray coating process

was done with ease. The Joule heating property of the fabricated samples was tested in stagnant air, static, and dynamic water. In stagnant air, only 27 W was needed to increase the temperature of the sample from room temperature to 85°C within a few minutes. To examine the samples in water, an H-bridge was coupled with our DC power supply. The H-bridge kept changing the direction of the current, which helped keep the electrons passing through the structure of the resistive heating material rather than water. It was proven that higher working frequencies of H-bridge made the performance of the Joule heating sample more efficient.

To test the functionality of the Joule heating elements as the heat source of the MD process, a special MD cell was designed. Our unique design helped us not only to mount our 1 mm thick samples inside the cell without causing any issues but also it enabled us to record the temperature of the water passing through the MD cell. As expected, the higher powers led to higher temperatures. Although the temperature of the feed side active area, while 80 W of power was being drawn, was 70-90°C, the measured flux was 2.24 kg/hr.m^2. Our experiments showed that the Joule heating coating layer was not strong enough to affect the temperature of the feed tank significantly. Therefore the only way it could have provided the necessary energy for the water to move from the feed side to the permeate side was by surface heating. Although the measured flux simply shows the inefficiency of this novel approach, this number could be justified by the amount of energy consumed. Comparing with the conventional heating baths used for the MD process, it could be inferred that the lower flux is proportional to the lower energy used in this system.

As a direct result of passing electricity through a corrosive environment, some components of the Joule heating element did corrode. Having spectated the stable heat

generation of the sample coupled with its prolonged lifespan, the samples were characterized by SEM to investigate the nature of the oxide layers. The SEM characterization showed that the nichrome material did not engage in the auxiliary electrochemical reactions. This layer only played the part of an ideal substrate for reactions to take place due to carrying electricity. The used membranes and the filtered water were also analyzed, and no signs of contaminants reaching the permeate side could be detected. This showed that not only could we integrate a Joule heating element into the MD process, but also the quality of the purified water was not compromised.

To further investigate the effect of the Joule heating element when used in the MD setup, a simple mathematical model was developed. The mathematical model, despite not being complicated, could predict the flux values with low error in most cases. Having observed the relative accuracy of the model, the other mathematical evaluations were also studied. The calculated temperature for the feed side of the membrane was lower than 26°C. This showed the inability and incompatibility of the Joule heating element to function efficiently in the current design. The effect of temperature polarization was much less prominent when compared to the numbers reported in the literature. The heat source being close to the membrane helps keep the temperature polarization in check. The thermal efficiency of this design increased with higher powers, but the efficiency was around 50 %, which was not impressive.

We believe that the goals set at the beginning of this research project were achieved. In the end, the achievements of this project are the design of a much needed and fully functional MD cell, fabrication of the Joule heating element on very thin substrates which

worked in all the target environments, and the development of an electrical circuit compatible with the nature of this project.

5.2 Future Work

It is necessary that a comprehensive study be conducted on the Joule heating coating layers when used as a heat source in the MD cell. The effect of all the involved parameters such as feed water flow rate, permeate water flow rate, and the chemical composition of the water should be analyzed. Also, there are many aspects of the design that are still unknown. One of the parameters which should be studied in detail is the space between the Joule heating element and the membrane. The main drawback of this innovation has been its low flux and overall energy efficiency. The improvement of these mentioned factors should be pursued. Finally, the components of the MD setup should become thermally insulated to create a closed system, retaining the generated heat inside the system. In the current setup, most of the heat generated by the Joule heating element was dumped in the feed tank and was wasted. In the end, it might be proven that the Joule heating element is not a suitable heat source when the feed water is not pre-heated. But we should remember that most industrial wastewaters are relatively hot. It is expected that the integration of Joule heating elements into the MD processes dealing with relatively hot waters could be more influential. The combination of these two designs could be the improvement needed for this method to become more widely used. Of course, the integration of conventional MD and the Joule heating coating layers should be the backup plan in case the Joule heating element is incapable of creating a significant temperature difference between the feed and permeate solution on its own.

References

[1] A.G. Koutroulis, L. V. Papadimitriou, M.G. Grillakis, I.K. Tsanis, R. Warren, R.A. Betts, Global water availability under high-end climate change: A vulnerability based assessment, Glob. Planet. Change. 175 (2019) 52–63. https://doi.org/10.1016/j.gloplacha.2019.01.013.

[2] S.N. Gosling, N.W. Arnell, A global assessment of the impact of climate change on water scarcity, Clim. Change. 134 (2016) 371–385. https://doi.org/10.1007/s10584-013-0853-x.

[3] B. Khorshidi, I. Biswas, T. Ghosh, T. Thundat, M. Sadrzadeh, Robust fabrication of thin film polyamide-TiO2 nanocomposite membranes with enhanced thermal stability and anti-biofouling propensity, Sci. Rep. 8 (2018). https://doi.org/10.1038/s41598-017-18724-w.

[4] E. Drioli, A. Ali, F. Macedonio, Membrane distillation: Recent developments and perspectives, Desalination. 356 (2015) 56–84. https://doi.org/10.1016/j.desal.2014.10.028.

[5] D. González, J. Amigo, F. Suárez, Membrane distillation: Perspectives for sustainable and improved desalination, Renew. Sustain. Energy Rev. 80 (2017) 238–259. https://doi.org/10.1016/j.rser.2017.05.078.

[6] M. Qasim, M. Badrelzaman, N.N. Darwish, N.A. Darwish, N. Hilal, Reverse osmosis desalination: A state-of-the-art review, Desalination. 459 (2019) 59–104. https://doi.org/10.1016/j.desal.2019.02.008.

[7] C.S. Fernandes, N.A.H.M. Nordin, M.R. Bilad, A. Aqsha, M.D.H. Wirzal, Z.A. Putra, Phase inversion and pore formation of PVDF membrane with silica as additive, J. Adv. Res. Fluid Mech. Therm. Sci. 49 (2018) 48–54.

[8] G. dong Kang, Y. ming Cao, Application and modification of poly(vinylidene fluoride) (PVDF) membranes - A review, J. Memb. Sci. 463 (2014) 145–165. https://doi.org/10.1016/j.memsci.2014.03.055.

[9] M. Mulder, Basic Principles of Membrane Technology, 1996.

[10] D.M. Wang, J.Y. Lai, Recent advances in preparation and morphology control of polymeric membranes formed by nonsolvent induced phase separation, Curr. Opin. Chem. Eng. 2 (2013) 229–237. https://doi.org/10.1016/j.coche.2013.04.003.

[11] H.C. Duong, D. Chuai, Y.C. Woo, H.K. Shon, L.D. Nghiem, V. Sencadas, A novel electrospun, hydrophobic, and elastomeric styrene-butadiene-styrene membrane for membrane distillation applications, J. Memb. Sci. 549 (2018) 420–427.

https://doi.org/10.1016/j.memsci.2017.12.024.

[12] F.E. Ahmed, N. Hilal, R. Hashaikeh, Electrically conductive membranes for in situ fouling detection in membrane distillation using impedance spectroscopy, J. Memb. Sci. 556 (2018) 66–72. https://doi.org/10.1016/j.memsci.2018.03.069.

[13] A. Politano, P. Argurio, G. Di Profio, V. Sanna, A. Cupolillo, S. Chakraborty, H.A. Arafat, E. Curcio, Photothermal Membrane Distillation for Seawater Desalination, Adv. Mater. 29 (2017) 1603504. https://doi.org/10.1002/adma.201603504.

[14] Z. Wang, D. Hou, S. Lin, Composite Membrane with Underwater-Oleophobic Surface for Anti-Oil-Fouling Membrane Distillation, Environ. Sci. Technol. 50 (2016) 3866–3874. https://doi.org/10.1021/acs.est.5b05976.

[15] A. Alkhudhiri, N. Hilal, Membrane distillation-Principles, applications, configurations, design, and implementation, Elsevier Inc., 2018. https://doi.org/10.1016/B978-0-12-815818-0.00003-5.

[16] B.B. Ashoor, S. Mansour, A. Giwa, V. Dufour, S.W. Hasan, Principles and applications of direct contact membrane distillation (DCMD): A comprehensive review, Desalination. 398 (2016) 222–246. https://doi.org/10.1016/j.desal.2016.07.043.

[17] M. Tomaszewska, Encyclopedia of Membranes, Encycl. Membr. 2 (2012). https://doi.org/10.1007/978-3-642-40872-4.

[18] D.M. Warsinger, J. Swaminathan, E. Guillen-burrieza, H.A. Arafat, J.H.L. V, Scaling and fouling in membrane distillation for desalination applications : A review, DES. 356 (2015) 294–313. https://doi.org/10.1016/j.desal.2014.06.031.

[19] L. Eykens, I. Hitsov, K. De Sitter, C. Dotremont, L. Pinoy, I. Nopens, B. Van der Bruggen, Influence of membrane thickness and process conditions on direct contact membrane distillation at different salinities, J. Memb. Sci. 498 (2016) 353–364. https://doi.org/10.1016/j.memsci.2015.07.037.

[20] A. Alkhudhiri, N. Darwish, N. Hilal, Membrane distillation: A comprehensive review, Desalination. 287 (2012) 2–18. https://doi.org/10.1016/j.desal.2011.08.027.

[21] M. Rezaei, D.M. Warsinger, J.H. Lienhard V, W.M. Samhaber, Wetting prevention in membrane distillation through superhydrophobicity and recharging an air layer on the membrane surface, J. Memb. Sci. 530 (2017) 42–52. https://doi.org/10.1016/j.memsci.2017.02.013.

[22] N. Thomas, M.O. Mavukkandy, S. Loutatidou, H.A. Arafat, Membrane distillation research & implementation: Lessons from the past five decades, Sep. Purif. Technol. 189 (2017) 108–127. https://doi.org/10.1016/j.seppur.2017.07.069.

[23] A.L. Ahmad, M.R.M. Ramli, M.I.M. Esham, Effect of additives on hydrophobicity of PVDF membrane in two-stage coagulation baths for desalination, J. Phys. Sci. 30 (2019) 207–221. https://doi.org/10.21315/jps2019.30.3.13.

[24] D. Hou, J. Wang, D. Qu, Z. Luan, C. Zhao, X. Ren, Preparation of hydrophobic PVDF hollow fiber membranes for desalination through membrane distillation, Water Sci. Technol. 59 (2009) 1219–1226. https://doi.org/10.2166/wst.2009.080.

[25] L. Eykens, K. De Sitter, C. Dotremont, L. Pinoy, B. Van der Bruggen, Membrane synthesis for membrane distillation: A review, Sep. Purif. Technol. 182 (2017) 36–51. https://doi.org/10.1016/j.seppur.2017.03.035.

[26] S. Munirasu, F. Banat, A.A. Durrani, M.A. Haija, Intrinsically superhydrophobic PVDF membrane by phase inversion for membrane distillation, Desalination. 417 (2017) 77–86. https://doi.org/10.1016/j.desal.2017.05.019.

[27] A. Deshmukh, C. Boo, V. Karanikola, S. Lin, A.P. Straub, T. Tong, D.M. Warsinger, M. Elimelech, Membrane distillation at the water-energy nexus: Limits, opportunities, and challenges, Energy Environ. Sci. 11 (2018) 1177–1196. https://doi.org/10.1039/c8ee00291f.

[28] A. Razmjou, E. Arifin, G. Dong, J. Mansouri, V. Chen, Superhydrophobic modification of TiO 2 nanocomposite PVDF membranes for applications in membrane distillation, J. Memb. Sci. 415–416 (2012) 850–863. https://doi.org/10.1016/j.memsci.2012.06.004.

[29] D. Hou, J. Wang, X. Sun, Z. Ji, Z. Luan, Preparation and properties of PVDF composite hollow fiber membranes for desalination through direct contact membrane distillation, J. Memb. Sci. 405–406 (2012) 185–200. https://doi.org/10.1016/j.memsci.2012.03.008.

[30] L.F. Ren, F. Xia, V. Chen, J. Shao, R. Chen, Y. He, TiO2-FTCS modified superhydrophobic PVDF electrospun nanofibrous membrane for desalination by direct contact membrane distillation, Desalination. 423 (2017) 1–11. https://doi.org/10.1016/j.desal.2017.09.004.

[31] M. Essalhi, M. Khayet, Membrane Distillation (MD), Elsevier Ltd, 2015. https://doi.org/10.1016/B978-0-12-384746-1.00003-3.

[32] M.R. Rahimpour, N.M. Kazerooni, M. Parhoudeh, Water treatment by renewable energy-driven membrane distillation, Elsevier Inc., 2019. https://doi.org/10.1016/B978-0-12-813545-7.00008-8.

[33] P.S. Goh, T. Matsuura, A.F. Ismail, N. Hilal, Recent trends in membranes and membrane processes for desalination, Desalination. 391 (2016) 43–60.

https://doi.org/10.1016/j.desal.2015.12.016.

[34] P. Wang, T.S. Chung, Recent advances in membrane distillation processes: Membrane development, configuration design and application exploring, J. Memb. Sci. 474 (2015) 39–56. https://doi.org/10.1016/j.memsci.2014.09.016.

[35] L. Martínez-Díez, M.I. Vázquez-González, Temperature and concentration polarization in membrane distillation of aqueous salt solutions, J. Memb. Sci. 156 (1999) 265–273. https://doi.org/10.1016/S0376-7388(98)00349-4.

[36] L. Huang, J. Pei, H. Jiang, X. Hu, Water desalination under one sun using graphene-based material modified PTFE membrane, Desalination. 442 (2018) 1–7. https://doi.org/10.1016/j.desal.2018.05.006.

[37] S. Cerneaux, I. Struzyńska, W.M. Kujawski, M. Persin, A. Larbot, Comparison of various membrane distillation methods for desalination using hydrophobic ceramic membranes, J. Memb. Sci. 337 (2009) 55–60. https://doi.org/10.1016/j.memsci.2009.03.025.

[38] J. Wu, K.R. Zodrow, P.B. Szemraj, Q. Li, Photothermal nanocomposite membranes for direct solar membrane distillation †, (2017). https://doi.org/10.1039/c7ta04555g.

[39] N.I.M. Nawi, M.R. Bilad, N.A.H.M. Nordin, M.O. Mavukkandy, Z.A. Putra, M.D.H. Wirzal, J. Jaafar, A.L. Khan, Exploiting the interplay between liquid-liquid demixing and crystallization of the PVDF membrane for membrane distillation, Int. J. Polym. Sci. 2018 (2018). https://doi.org/10.1155/2018/1525014.

[40] D. González, J. Amigo, F. Suárez, Membrane distillation: Perspectives for sustainable and improved desalination, Renew. Sustain. Energy Rev. 80 (2017) 238–259. https://doi.org/10.1016/j.rser.2017.05.078.

[41] L.D. Tijing, Y.C. Woo, W.G. Shim, T. He, J.S. Choi, S.H. Kim, H.K. Shon, Superhydrophobic nanofiber membrane containing carbon nanotubes for high-performance direct contact membrane distillation, J. Memb. Sci. 502 (2016) 158–170. https://doi.org/10.1016/j.memsci.2015.12.014.

[42] L. Eykens, K. De Sitter, C. Dotremont, L. Pinoy, B. Van Der Bruggen, How to Optimize the Membrane Properties for Membrane Distillation: A Review, Ind. Eng. Chem. Res. 55 (2016) 9333–9343. https://doi.org/10.1021/acs.iecr.6b02226.

[43] A. Luo, N. Lior, Critical review of membrane distillation performance criteria, Desalin. Water Treat. 57 (2016) 20093–20140. https://doi.org/10.1080/19443994.2016.1152637.

[44] W. Albrecht, R. Hilke, K. Kneifel, T. Weigel, K. V. Peinemann, Selection of microporous hydrophobic membranes for use in gas/liquid contactors: An

experimental approach, J. Memb. Sci. 263 (2005) 66–76. https://doi.org/10.1016/j.memsci.2005.04.005.

[45] A. V Dudchenko, C. Chen, A. Cardenas, J. Rolf, D. Jassby, Frequency-dependent stability of CNT Joule heaters in ionizable media and desalination processes, Nat. Nanotechnol. |. 12 (2017). https://doi.org/10.1038/NNANO.2017.102.

[46] Y.S. Jun, X. Wu, D. Ghim, Q. Jiang, S. Cao, S. Singamaneni, Photothermal Membrane Water Treatment for Two Worlds, Acc. Chem. Res. (2019). https://doi.org/10.1021/acs.accounts.9b00012.

[47] H. Ye, X. Li, L. Deng, P. Li, T. Zhang, X. Wang, B.S. Hsiao, Silver Nanoparticle-Enabled Photothermal Nanofibrous Membrane for Light-Driven Membrane Distillation, Ind. Eng. Chem. Res. 58 (2019) 3269–3281. https://doi.org/10.1021/acs.iecr.8b04708.

[48] Y.Z. Tan, H. Wang, L. Han, M.B. Tanis-Kanbur, M.V. Pranav, J.W. Chew, Photothermal-enhanced and fouling-resistant membrane for solar-assisted membrane distillation, J. Memb. Sci. 565 (2018) 254–265. https://doi.org/10.1016/j.memsci.2018.08.032.

[49] D. Tejero-Martin, M. Rezvani Rad, A. McDonald, T. Hussain, Beyond Traditional Coatings: A Review on Thermal-Sprayed Functional and Smart Coatings, Springer US, 2019. https://doi.org/10.1007/s11666-019-00857-1.

[50] M. Rezvani-Rad, Application of Thermally-Sprayed Coatings as Heat Tracers for Carbon Steel Pipes to Mitigate the Effect of Ice Accumulation and Freezing Damage, (2019).

[51] T.S. Technology, R.C. Tucker, Introduction to Coating Design and Processing, Therm. Spray Technol. 5 (2018) 76–88. https://doi.org/10.31399/asm.hb.v05a.a0005725.

[52] H. Ashrafizadeh, A. McDonald, P. Mertiny, Deposition of Electrically Conductive Coatings on Castable Polyurethane Elastomers by the Flame Spraying Process, J. Therm. Spray Technol. 25 (2016) 419–430. https://doi.org/10.1007/s11666-015-0376-2.

[53] S. Sampath, H. Herman, A. Patel, R. Gambino, R. Greenlaw, E. Tormey, Thermal Spray Techniques for Fabrication of Meso-Electronics and Sensors, 624 (2000) 181–188.

[54] M. Niittymaki, K. Lahti, T. Suhonen, J. Metsajoki, Effect of temperature and humidity on dielectric properties of thermally sprayed alumina coatings, IEEE Trans. Dielectr. Electr. Insul. 25 (2018) 908–918.

https://doi.org/10.1109/TDEI.2018.006892.

[55] R. Gonzalez, H. Ashrafizadeh, A. Lopera, P. Mertiny, A. McDonald, A Review of Thermal Spray Metallization of Polymer-Based Structures, J. Therm. Spray Technol. 25 (2016) 897–919. https://doi.org/10.1007/s11666-016-0415-7.

[56] J.R. Davis, Introduction to Thermal Spray Processing, Handb. Therm. Spray Technol. (2004) 3–13.

[57] D. Tejero-Martin, M. Rezvani Rad, A. McDonald, T. Hussain, Beyond Traditional Coatings: A Review on Thermal-Sprayed Functional and Smart Coatings, J. Therm. Spray Technol. (2019). https://doi.org/10.1007/s11666-019-00857-1.

[58] Oerlikon Metco, An Introduction to Thermal Spray [Brochure], Http://Www.Oerlikon.Com/Metco/En/Products-Services/Coating-Equipment/Thermal-Spray/. (2014) 9.

[59] M. Prudenziati, Development and the implementation of high-temperature reliable heaters in plasma spray technology, J. Therm. Spray Technol. 17 (2008) 234–243. https://doi.org/10.1007/s11666-008-9164-6.

[60] B. Jeffery, A. McDonald, M. Peppler, R.S. Lima, Bactericidal effects of HVOF-sprayed nanostructured TiO2 on pseudomonas aeruginosa, in: Proc. Int. Therm. Spray Conf., 2009: pp. 376–381. https://doi.org/10.1361/cp2009itsc0376.

[61] M. Rezvani Rad, M.M. Bajgiran, C. Moreau, A. Mcdonald, Microstructural and Performance Analyses of Thermal-Sprayed Electric Resistance Heating Systems as De-Icing Elements, (n.d.).

[62] P.L. Fauchais, J.V.R. Heberlein, M.I. Boulos, Thermal Spray Fundamentals, 2014. https://doi.org/10.1007/978-0-387-68991-3.

[63] D. Michels, J. Hadeler, J.H. Lienhard, High-heat-flux resistance heaters from vps and hvof thermal spraying, Exp. Heat Transf. 11 (1998) 341–359. https://doi.org/10.1080/08916159808946570.

[64] M.M. Bajgiran, C. Moreau, M.R. Rad, A. Mcdonald, On Reliability of Thermally-Sprayed Alumina Dielectric Layers in a Multi- layered Coating-based Heating System, (2019) 1–7.

[65] J.M. Lamarre, P. Marcoux, M. Perrault, R.C. Abbott, J.G. Legoux, Performance analysis and modeling of thermally sprayed resistive heaters, J. Therm. Spray Technol. 22 (2013) 947–953. https://doi.org/10.1007/s11666-013-9946-3.

[66] F.L. Toma, S. Scheitz, L.M. Berger, V. Sauchuk, M. Kusnezoff, S. Thiele, Comparative study of the electrical properties and characteristics of thermally

sprayed alumina and spinel coatings, J. Therm. Spray Technol. 20 (2011) 195–204. https://doi.org/10.1007/s11666-010-9580-2.

[67] F.L. Toma, L.M. Berger, S. Scheitz, S. Langner, C. Rödel, A. Potthoff, V. Sauchuk, M. Kusnezoff, Comparison of the microstructural characteristics and electrical properties of thermally sprayed Al 2O 3 coatings from aqueous suspensions and feedstock powders, J. Therm. Spray Technol. 21 (2012) 480–488. https://doi.org/10.1007/s11666-012-9761-2.

[68] J. Mollá, M. González, R. Vila, A. Ibarra, Effect of humidity on microwave dielectric losses of porous alumina, J. Appl. Phys. 85 (1999) 1727–1730. https://doi.org/10.1063/1.369317.

[69] R. Gerson, T.C. Marshall, Dielectric breakdown of porous ceramics, J. Appl. Phys. 30 (1959) 1650–1653. https://doi.org/10.1063/1.1735030.

[70] D. Michels, J. Hadeler, J.H. Lienhard, High-heat-flux resistance heaters from vps and hvof thermal spraying, Exp. Heat Transf. 11 (1998) 341–359. https://doi.org/10.1080/08916159808946570.

[71] A. Lopera-Valle, A. McDonald, Application of Flame-Sprayed Coatings as Heating Elements for Polymer-Based Composite Structures, J. Therm. Spray Technol. 24 (2015) 1289–1301. https://doi.org/10.1007/s11666-015-0302-7.

[72] A. Lopera-Valle, A. McDonald, Flame-sprayed coatings as de-icing elements for fiber-reinforced polymer composite structures: Modeling and experimentation, Int. J. Heat Mass Transf. 97 (2016) 56–65. https://doi.org/10.1016/j.ijheatmasstransfer.2016.01.079.

[73] M. Rezvani Rad, A. McDonald, Development of a thermal-sprayed coating system to mitigate ice accumulation and freezing damage in carbon steel pipes, Proc. Int. Therm. Spray Conf. 2018-May (2018) 635–642.

[74] J. Zuo, Fundamental Principles of Membrane Distillation Membrane Fabrication, Membr. Distill. (2019) 39–68. https://doi.org/10.1201/9780429287879-3.

[75] E. Fontananova, J.C. Jansen, A. Cristiano, E. Curcio, E. Drioli, Effect of additives in the casting solution on the formation of PVDF membranes, Desalination. 192 (2006) 190–197. https://doi.org/10.1016/j.desal.2005.09.021.

[76] C. Meringolo, T.F. Mastropietro, T. Poerio, E. Fontananova, G. De Filpo, E. Curcio, G. Di Profio, Tailoring PVDF Membranes Surface Topography and Hydrophobicity by a Sustainable Two-Steps Phase Separation Process, ACS Sustain. Chem. Eng. 6 (2018) 10069–10077. https://doi.org/10.1021/acssuschemeng.8b01407.

[77] F. Liu, N.A. Hashim, Y. Liu, M.R.M. Abed, K. Li, Progress in the production and

modification of PVDF membranes, J. Memb. Sci. 375 (2011) 1–27. https://doi.org/10.1016/j.memsci.2011.03.014.

[78] D.Y. Zuo, Y.Y. Xu, W.L. Xu, H.T. Zou, The influence of PEG molecular weight on morphologies and properties of PVDf asymmetric membranes, Chinese J. Polym. Sci. (English Ed. 26 (2008) 405–414. https://doi.org/10.1142/S0256767908003072.

[79] M. Haponska, A. Trojanowska, A. Nogalska, R. Jastrzab, T. Gumi, B. Tylkowski, PVDF membrane morphology - Influence of polymer molecularweight and preparation temperature, Polymers (Basel). 9 (2017) 1–14. https://doi.org/10.3390/polym9120718.

[80] I. Hitsov, T. Maere, K. De Sitter, C. Dotremont, I. Nopens, Modelling approaches in membrane distillation: A critical review, Sep. Purif. Technol. 142 (2015) 48–64. https://doi.org/10.1016/j.seppur.2014.12.026.

[81] S. Noamani, Development of a Self-sustained Model to Predict the Water Desalination Performance of the Membrane Distillation Process, (2020).

[82] Thermo Scientific Laboratory Temperature Control Products, ADVANCED Series Heated Immersion Circulators, (2013) 115050.

[83] Health Canada, Aluminum in Drinking Water - For Public Consultation, (2019). https://www.canada.ca/content/dam/hc-sc/images/programs/consultation-aluminum-drinking-water/aluminum-eng-consultation.pdf.

[84] G.T. Document, Guidelines for Canadian Drinking Water Quality - Chromium, 2016. www.canada.ca/en/health-canada/services/environmental-workplace-health/reports-.

[85] Health Canada, Guidelines for Canadian drinking water quailty - technical document for iron, Gov. Canada. 1978 (1987) 15–18. http://www.hc-sc.gc.ca/ewh-semt/pubs/water-eau/index-eng.php#tech_doc.

[86] Environment Canada, Canadian Environmental Protection Act, 1999-Federal Environmental Quality Guidelines- Cobalt, (2013) 1–10.

[87] WHO, Nickel in Drinking-water, Environ. Heal. (2005).

[88] Federal-Provincial-Territorial Committee on Drinking Water (CDW), Copper in Drinking Water: Guideline Technical Document for public consultation, (2018) 78. https://www.canada.ca/en/health-canada/programs/consultation-copper-drinking-water/document.html.

[89] J.G. Lee, E.J. Lee, S. Jeong, J. Guo, A.K. An, H. Guo, J. Kim, T.O. Leiknes, N. Ghaffour, Theoretical modeling and experimental validation of transport and

separation properties of carbon nanotube electrospun membrane distillation, J. Memb. Sci. 526 (2017) 395–408. https://doi.org/10.1016/j.memsci.2016.12.045.

[90] I. Hitsov, K. De Sitter, C. Dotremont, P. Cauwenberg, I. Nopens, Full-scale validated Air Gap Membrane Distillation (AGMD) model without calibration parameters, J. Memb. Sci. 533 (2017) 309–320. https://doi.org/10.1016/j.memsci.2017.04.002.

[91] G. Rao, S.R. Hiibel, A.E. Childress, Simplified flux prediction in direct-contact membrane distillation using a membrane structural parameter, Desalination. 351 (2014) 151–162. https://doi.org/10.1016/j.desal.2014.07.006.

[92] I. Hitsov, PhD Dissertation: Model-based analysis and optimization of membrane distillation, 2017.

[93] D. Winter, Membrane Distillation - A Thermodynamic, Technological and Economic Analysis (PhD Thesis), (2014) 341. https://www.reiner-lemoine-stiftung.de/pdf/dissertationen/Dissertation-Daniel_Winter.pdf.

[94] A. Khalifa, H. Ahmad, M. Antar, T. Laoui, M. Khayet, Experimental and theoretical investigations on water desalination using direct contact membrane distillation, Desalination. 404 (2017) 22–34. https://doi.org/10.1016/j.desal.2016.10.009.

[95] M. Qtaishat, T. Matsuura, B. Kruczek, M. Khayet, Heat and mass transfer analysis in direct contact membrane distillation, Desalination. 219 (2008) 272–292. https://doi.org/10.1016/j.desal.2007.05.019.

[96] S.O. Olatunji, L.M. Camacho, Heat and mass transport in modeling membrane distillation configurations: A review, Front. Energy Res. 6 (2018) 1–18. https://doi.org/10.3389/fenrg.2018.00130.

[97] Ó. Andrjesdóttir, C.L. Ong, M. Nabavi, S. Paredes, A.S.G. Khalil, B. Michel, D. Poulikakos, An experimentally optimized model for heat and mass transfer in direct contact membrane distillation, Int. J. Heat Mass Transf. 66 (2013) 855–867. https://doi.org/10.1016/j.ijheatmasstransfer.2013.07.051.

[98] A. Ali, F. Macedonio, E. Drioli, S. Aljlil, O.A. Alharbi, Experimental and theoretical evaluation of temperature polarization phenomenon in direct contact membrane distillation, Chem. Eng. Res. Des. 91 (2013) 1966–1977. https://doi.org/10.1016/j.cherd.2013.06.030.